

Laser and carbon: nanotube synthesis and annealing

Dissertation

zur Erlangung des Grades
des Doktors der Ingenieurwissenschaften
der Naturwissenschaftlich Technischen Fakultät
der Universität des Saarlandes



von

NICOLÁS SOUZA CARMONA

Saarbrücken

2017

Tag des Kolloquiums: 28.07.2017

Dekan: Prof. Dr. G. Kickelbick

Berichterstatte: Prof. Dr.-Ing. F. Mücklich
Prof. Dr. V. Presser

Vorsitz: Prof. Dr.-Ing. D. Bähre

Akad. Mitarbeiter: Dr.-Ing. F. Aubertin

Laser and carbon: nanotube synthesis and annealing

Written in EU standard: British English (BE) and decimal comma (,.)

Results and discussion with decimal point (.) for publishing.



THE MOST EXCITING PHRASE
TO HEAR IN SCIENCE,
THE ONE THAT HERALDS
NEW DISCOVERIES,
IS NOT 'EUREKA!' BUT
'THAT'S FUNNY...'

Isaac Asimov

Contents

Abstract.....	VIII
Zusammenfassung	IX
Acknowledgements.....	X
Scientific contributions	XII
Featured peer-review publications.....	XII
Further peer-review collaborations in laser and/or carbon nanotubes.....	XII
Talks	XIII
Conference posters.....	XIII
Prize.....	XIII
1. Carbon nanotubes.....	1
1.1. History	2
1.2. Properties.....	4
Electrical properties	7
Mechanical properties	8
Optical properties	9
Limiting factors	11
1.3. Synthesis	14
Growth	14
Synthesis techniques	15
Alternative carbon feedstocks	20
2. Motivation and goals	22
3. Materials and methods.....	24
3.1. CNT synthesis.....	24
Oven-laser apparatus: Pulsed laser deposition	24
Experimental run-through	27

3.2.	Processing	27
3.3.	Characterisation.....	28
4.	Results and discussion	30
4.1.	In situ tracking of defect healing and purification of single-wall carbon nanotubes with laser radiation by time-resolved Raman spectroscopy	30
4.2.	Scaling up single-wall carbon nanotube laser annealing: effect on electrical resistance and hydrogen adsorption	43
4.3.	Upcycling spent petroleum cracking catalyst (FC3R): pulsed laser deposition of single-wall carbon nanotubes and silica nanowires	53
5.	Conclusion and outlook	65
	Appendix	68
	Literature	74
	List of figures.....	80
	List of symbols.....	82
	List of abbreviations.....	84
	List of units.....	85
	Lebenslauf	87

Abstract

Thanks to their predicted and measured properties, carbon nanotubes (CNTs) are becoming viable and superior alternatives to many of materials science's established materials. Yet, although the divide between model and reality has narrowed, insufficient CNT quality and purity remain major hindrances to the performance of most CNT-based materials. Furthermore, CNT precursors are overwhelmingly high-purity petrochemical substances, hampering sustainable and widespread adoption of CNTs.

These two identified challenges were addressed towards synthesis energy and cost efficiency, sustainability and material performance. To this end, single-wall CNTs (SWCNTs) were synthesised in a custom-built oven laser apparatus as the object of this study.

Laser annealing was found to quickly and drastically recrystallise defects and remove impurities as measured by Raman spectroscopy, thermogravimetry, electrical resistance and hydrogen adsorption measurements. Results could be reproduced at the micro- and millimetre scale. Composite processing related damage, artificially introduced into SWCNTs, was almost completely reversed by laser annealing. Quality and purity levels equal to that of commercial tubes could be achieved through this technique.

A waste product of petroleum refining, fluid catalytic cracking catalyst residue, was successfully employed as carbon precursor for SWCNT synthesis, as well as silica nanowires, onion-like carbons and carbon nanodiamonds.

Zusammenfassung

Aufgrund Ihrer vielfach prognostizierten aber auch bekannten Eigenschaften, werden Kohlenstoff-Nanoröhrchen (CNTs) zu konkurrenzfähigen und teilweise überlegenen Alternativen zu vielen in der Materialforschung etablierten Materialien. Obwohl sich die „Kluft“ zwischen Modellvorstellungen und Realität verkleinert hat, sind die unzureichende CNT-Qualität und Reinheit noch immer wesentliche Hindernisse für die Performance der meisten CNT-basierten Materialien. Darüber hinaus sind CNT-Vorgänger überwiegend hochreine petrochemische Substanzen, die eine Akzeptanz von CNTs erschweren.

Diese Arbeit befasst sich mit den damit verknüpften Herausforderungen nämlich den Zielen Energie-/Kosteneffizienz, Nachhaltigkeit und Performance. Zu diesem Zweck wurden einwandige CNTs (SWCNTs) in einem speziellen Ofen, der mit einem Hochleistungslaser kombiniert wurde, synthetisiert und näher studiert.

Die Laserbehandlung heilt Defekte und entfernt Verunreinigungen schnell und effizient. Dies wurde durch Raman-Spektroskopie, Thermogravimetrie, elektrische Widerstandsmessung und schließlich Wasserstoff-Adsorption bestätigt. Die Ergebnisse konnten im Mikro- und Millimeterbereich reproduziert werden. Herstellungsbedingte Defekte in den SWCNTs konnten durch Laserglühen fast vollständig beseitigt werden. Durch diese Technik konnten Qualität und Reinheitsgrade erreicht werden, die denen von handelsüblichen Nanoröhrchen entsprechen.

Katalysatorrückstände des Cracking Prozesses während der Erdölraffination wurden dabei für die Synthese von SWCNTs, sowie Silica-Nanodrähten, „Onion-like Carbon“ und Kohlenstoff-Nanodiamanten eingesetzt.

Acknowledgements

Having explored different approaches at such a vast and arduous undertaking, I naturally proceeded with structure and order, from broad to specific, trying not to leave anything out. Half way through, I realised I had no idea what I was doing and impostor syndrome kicked in. *Who cares about this? Why am I doing this?* Then, inspiration appeared like a fresh Mensa Tüte full of edible goodies (not just magazines and ads). The acknowledgements were on their way.

These emotional salutations are for another enterprise, the seven years preceding; nods to people who made this project start, live and conclude, chronologically. Structure be damned.

First, I must thank my Schwester, Paula, for having believed in me and convinced me that a PhD was within my reach. Thanks to her, her personality, professionalism and work ethics, I benefited – as I often have – from people’s misguided beliefs that intelligence runs in the family (some school teachers now know better). *Her* reputation preceded me and she, along with Dr. Sebastián Suarez, fought to get me in. His presentation on why we should make carbon nanotubes at FuWe – *we have a laser, we have an oven, we have graphite ...* – was where it all started. This eventually led to Prof. Frank Mücklich believing these two wonderful people, and thus believing in me. Special thanks to him for the trust, means, support and flexibility bestowed on me. Unfortunately, rancid capitalism and the 2008 financial crisis also set the stage for my contacts and job promises to vanish, nudging me in the right direction.

To my office homies, Federico Lasserre and Dr. Suarez, my mentors, I owe my day-to-day wellbeing; two-one-one foreva’. You kept me afloat and never eager to call it a Feierabend. Regular motivational talks and wake-up calls kept me on track. The same goes for the greater FuWe cosmos: friends, colleagues, foosball fiends, chill-out area and kitchen procrastinators, parties and get-togethers; the Germans, the Latin Americans, the French, the Asians; my extended family.

A round of applause for Dr. Flavio Soldera for securing funding for me (thank you DAAD) and for international projects (thank you European Commission), with which I worked, travelled and grew as a scientist and as a person.

Many thanks to Prof. Volker Presser for providing access to very critical laboratory equipment, and especially for endorsing my “That’s funny...”-moment and giving my thesis a direction. Thanks to Marco Zeiger, from his team, who also helped with many measurements.

In the end, a Kiss got me through these trying times – a Dr. Flóra Márta Kiss – who I met half way through my PhD, starting her own PhD in biochemistry, and who gave new meaning to the question ‘are you hung(a)ry?’. My best friend and wife* made everything fun and feel like home, on and off campus. Köszönöm, szerelmem, for your constant support and motivation, especially in finishing this thesis.

This homey feeling was completed by my family, with whom I – unexpectedly – again shared a home/city/region with: my sister Paula, my brother-in-law Val, my two nieces Elsa and Nina, and my dad Juan, who moved from Spain to be with us. You gave me refuge and love. In Saarbrücken, I had it all.

*same person.

Scientific contributions

Featured peer-review publications

→ *Results and discussion*

This work is based on three original research papers reproduced in chapter 4 *Results and discussion*. The original manuscripts are printed with kind permission of the Royal Society of Chemistry and the Journal RSC Advances.

“Scaling up single-wall carbon nanotube laser annealing: effect on electrical resistance and hydrogen adsorption” [N. Souza](#), Martín Roble, Donovan E. Diaz-Droguett, F. Mücklich; *RSC Adv.*, 2017, 7, 5084-5092

“Upcycling spent petroleum cracking catalyst: simultaneous pulsed laser deposition of single-wall carbon nanotubes and silica nanowires” [N. Souza](#), F. Lasserre, A. Blickley, M. Zeiger, S. Suarez, M. Duarte, V. Presser, F. Mücklich; *RSC Adv.*, 2016, 6, 72596-72606

“In situ tracking of defect healing and purification of single-wall carbon nanotubes with laser radiation by time-resolved Raman spectroscopy” [N. Souza](#), M. Zeiger, V. Presser, F. Mücklich; *RSC Advances*, 2015, 5, 62149–62159

Further peer-review collaborations in laser and/or carbon nanotubes

“Long-lasting solid lubrication by CNT-coated patterned surfaces” L. Reinert, F. Lasserre, C. Gachot, P. Grützmacher, T. Maclucas, [N. Souza](#), F. Mücklich, S. Suarez; *Scientific Reports*; Accepted

“Influence of the reinforcement distribution on the electronic transport properties of MWCNT-reinforced metal matrix composites” S. Suarez, [N. Souza](#), F. Lasserre & F. Mücklich; *Advanced Engineering Materials*, 2016, 18, 1-8

“Tailored frictional properties by Penrose inspired surfaces produced by direct laser interference patterning” C. Gachot, A. Rosenkranz, R. Buchheit, [N. Souza](#), F. Mücklich; *Applied Surface Science*, 2016, 367, 174–180

“Simultaneous deposition of carbon nanotubes and decoration with gold-palladium nanoparticles by laser induced forward transfer” Federico Lasserre, Andreas Rosenkranz, [N.](#)

[Souza](#), Martin Roble, Esteban Ramos-Moore, Donovan Diaz-Droguett, Frank Mücklich; *Appl. Phys. A*, 2016, 122:150

“Wear debris and electrical resistance in textured Sn-coated Cu contacts subjected to fretting” K. E. Trinh, A. Tsipenyuk, M. Varenberg, A. Rosenkranz, [N. Souza](#), F. Mücklich; *Wear*, 2015, 344-345, 86-98

“Wetting Properties of Steel Surfaces Modified by Laser Interference Metallurgy” B. Raillard, J. Rémond, E. Ramos-Moore, [N. Souza](#), C. Gachot, F. Mücklich; *Tribology Letters*, 2013, 15, 341-346

“Dry Friction Between Laser-Patterned Surfaces: Role of Alignment, Structural Wavelength and Surface Chemistry” C. Gachot, A. Rosenkranz, L. Reinert, E. Ramos-Moore, [N. Souza](#), M. H. Müser, F. Mücklich; *Tribology Letters*, 2012, 49, 193-202

Talks

“Laser surface annealing of single-wall carbon nanotubes” 1st Workshop on Nanostruct. Mat. and Surface Engineering, Pontifical Catholic Univ. of Chile, Chile, Nov. 11-13.2014

“Laser-assisted growth of high-quality carbon nanotubes” *NanoCom Workshop*, Uni. Saarland, Saarbrücken, Apr. 30-31.2013

Conference posters

→ Appendix

“Laser annealing of single-wall carbon nanotubes” N. Souza, Volker Presser, Frank Mücklich; *NT14 2014*, Los Angeles, USA

“Laser-assisted growth of high-quality CNTs” N. Souza, S. Suárez Vallejo, F. Soldera, F. Mücklich; *ChemOnTubes 2012*, Arcachon, France

Prize

→ Appendix

Best electron micrography in Germany - 1st place in national electron micrography contest *Rendering the nanosized visible* by cc-nanobionet. Presented at WING 2011 Berlin and at Deutsches Museum in Munich. Published in *Der Spiegel* (41/2011) and others. Current branding for the Deutscher Verband Nanotechnologie e.V.

1. Carbon nanotubes

A nanomaterial is arguably considered as such when at least one of its external (or either internal/external) spatial dimensions is in the conventional nm scale (loosely, $1 - 10^2$; as opposed to 10^3)^[1]. In the external sense, and with decreasing nano-dimensionality, dot-, rod- and plate-like nanomaterials/-structures (Figure 1) have been discovered, produced and imagined, since before the inception of nanotechnology in a broader sense. In addition to its nanodimensions, a nanomaterial is often referred to as 0-D (dot), 1-D (rod) or 2-D (plate), pertaining to a usually large aspect ratio, non-nano to nano. In a more physical sense, this indicates the number of dimensions in which governing phenomena deviate from that which is observed in bulk materials, those not restricted to the nanoscale.

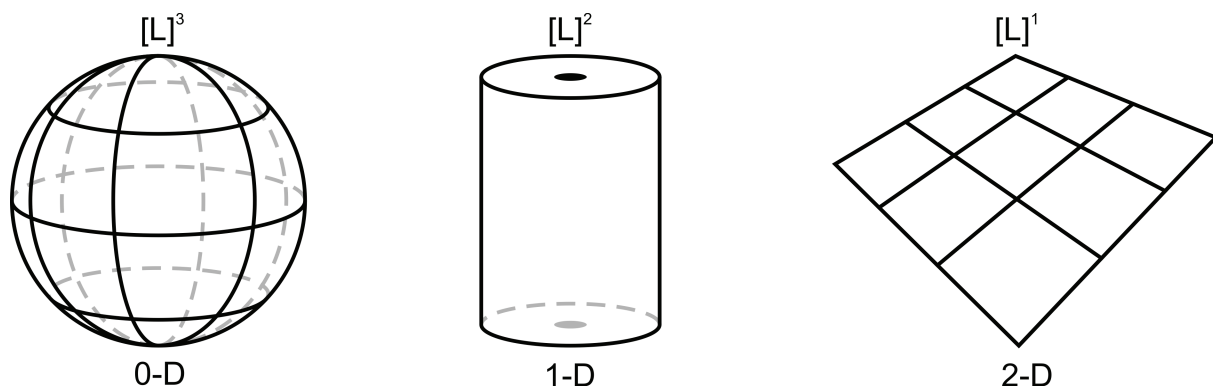


Figure 1 – Schematic classification of a nanomaterial according to the number of its external dimensions in (top row) and out of (bottom row) the nanoscale.

Perhaps the most known, DNA is a 1-D nanomaterial, namely, a nanowire (full; tubes are hollow). 1-D nanostructures are important in current and future mesoscopic physics. At this scale, in close proximity of the wavelength of the electron's wave function, electrons experience lateral quantum confinement, occupying distinct energy levels that differ from the continuum in bulk materials^[2]. This results in improved band-gap tuning for electronic devices^[3,4]. Mechanically, nanotubes/-wires provide anisotropy, facile strain relaxation and greatly exceed the strength of their bulk counterparts^[3,5,6]. In light absorption, this form factor produces extreme light trapping (reduced reflection) and increased defect tolerance^[3,7]. Similarly, their high surface area to volume ratio is useful in immersed contact applications such as gas sensing^[8] and water filtration^[9]. These benefits ultimately translate to increased efficiency, or conversely, to reduced quantity and quality of material necessary for equal efficiency, allowing for substantial cost reductions^[3].

1.1. History

Although retroactively tied to Richard Feynman's 1959 "There's plenty of room at the bottom" speech, the onset of a deterministic approach to nanoscience was brought on in the 1980s, among other things, by the invention of the scanning tunnelling microscope and the ensuing discovery of fullerenes in 1985 by Smalley and co-workers^[10]. These hollow macro molecules of sp^2 carbon, named after architect Richard Buckminster Fuller and his geodesic domes, were the symbolic and literal seeds of what would become the darling of modern research and nanotechnology: carbon nanotubes (CNTs).

Discovered in a fullerene reactor in 1991 by Sumio Iijima^[11], *tubular* fullerenes (not yet named CNTs) ushered in a new era in nanomaterials and carbon allotrope buzz. After years of overwhelming credit to Iijima for the discovery, the carbon community backpedalled half a century, realizing CNTs had been seen before^[12]. Mentions of tubular/hollow carbon/graphitic filaments/whiskers/fibres/fibrils began as soon as 1952, published in a Soviet journal in Russian^[13], followed by others. Yet, language, visibility, politics, but mostly insufficient resolution in imaging techniques relegated the findings. Still, the momentum of the 1991 discovery, those that followed and maturing characterisation techniques, would culminate in Kroto, Curl and Smalley's shared 1996 Nobel Prize in chemistry for their roles in discovering fullerenes, and the 2010 iteration in physics to Andre Geim and Konstantin Novoselov for their contributions to graphene. Nanotechnology is thus inextricably linked to fullerenes, which sparked research in CNTs and graphene, each with a more pronounced growth in publications than the previous (Figure 2). In fact, the '96 fullerene Nobel seems to have been the inflexion point for CNT research.

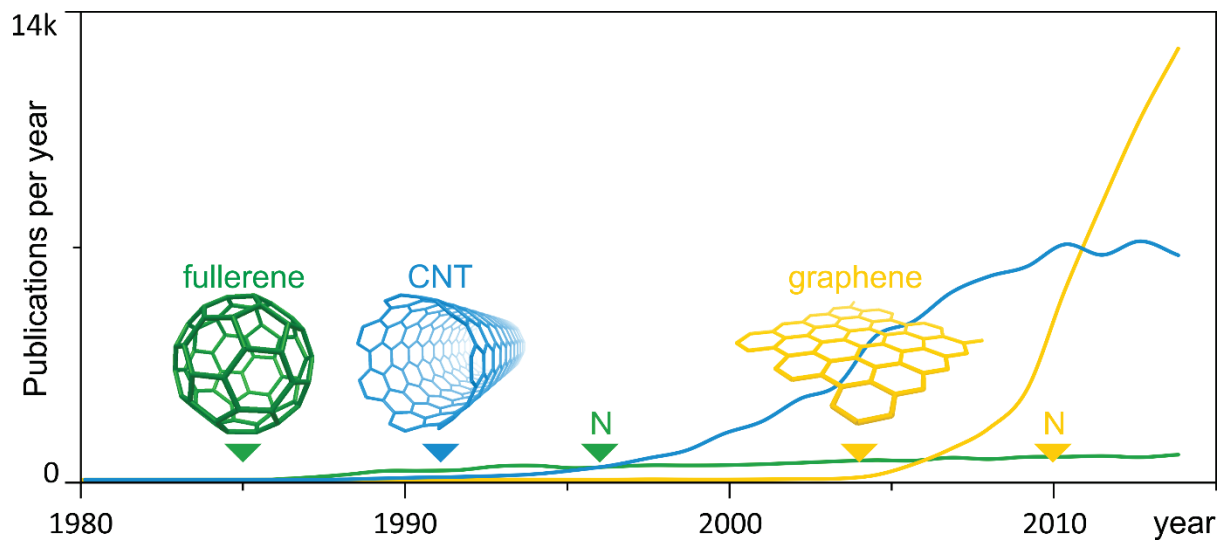


Figure 2 - Fullerene (green), CNT (blue) and graphene (yellow) discovery and Nobel prize (N) milestones, and publications per year. Data from Web of Science, corrected for the variety of nomenclatures for each species and cross-hits (e.g. "fullerene" in "tubular fullerene").

Although CNT research seems to have plateaued since 2010, with attention shifting towards its younger sibling, graphene, CNTs have achieved a market stronghold in several sectors. With ever-growing capacity and market, the nascent CNT industry caters over 60 % to polymer composites, as well as electronics, energy generation and others (Figure 3). The 2014 market of ~5 kT is foreseen to more than quadruple by 2022^[14].

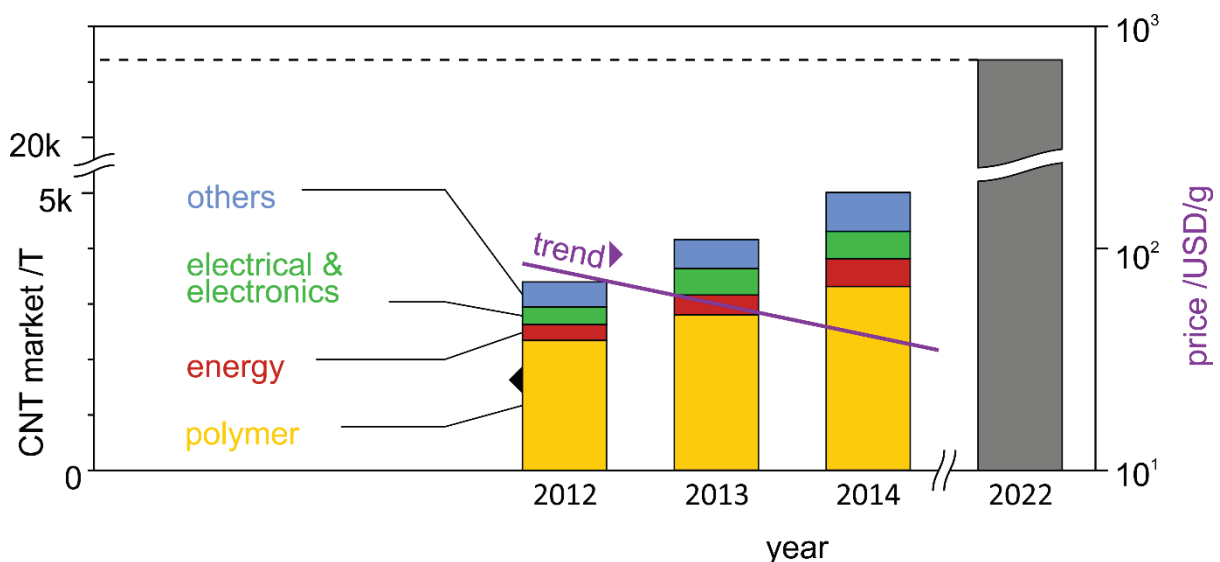


Figure 3 – Yearly world CNT market estimate by segment (in kT; left axis) and forecast ^[14]; gram price trend based on single-wall carbon nanotube prices of 1500 \$ in 2000, 50 \$ in 2010 and 2 \$ in 2016 (USD/g; right axis).

CNTs research has matured with currently hundreds of CNT manufacturers world-wide, capitalizing on 1500-2000 patents a year (surpassed by graphene in 2012)^[15]. The result of this is plummeting CNT prices (Figure 3: right axis), further enabling widespread adoption,

with a commercial success that is due to their outstanding physical properties that appeal to a wide variety of applications. In the following is a summary of the most important characteristics and properties of **ideal CNTs** (unless specified otherwise).

1.2. Properties

Carbon, the fifteenth most common element in the Earth's crust is extremely abundant and diverse. This back bone of organic life can adopt sp , sp^2 and sp^3 hybridisations thanks to its electronic structure and is present in a variety of allotropes, the most common of which is graphite.

When dragging a pencil along a piece of paper, the graphite in it exfoliates weakly bound layers of carbon. One such atom-thick layer, graphene, consists of a honeycomb lattice of sp^2 -hybridised, strongly-bonded carbon. This means every carbon atom, at the vertices of each hexagon, possesses three coplanar sp^2 orbitals and an orthogonal p_z orbital (Figure 4). Neighbouring collinear sp^2 orbitals form in-plane σ bonds, complemented by every other atom's parallel p_z orbital's π bond. These alternating double bonds, switching between neighbouring atoms create delocalised electrons, beyond common 6-membered ring aromaticity, in the whole graphene lattice, much like in metals.

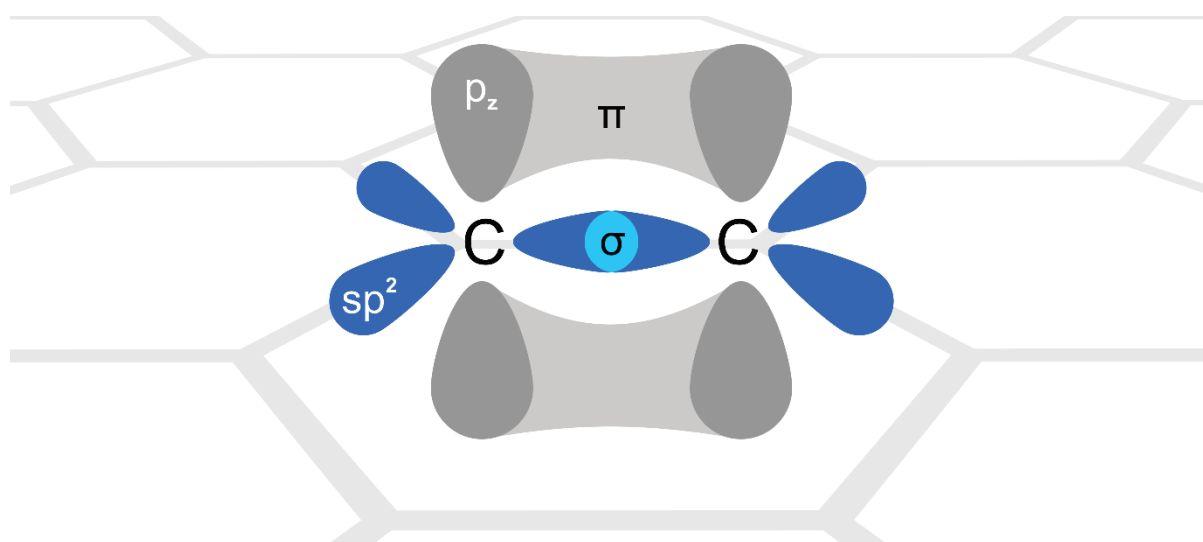


Figure 4 – sp^2 carbon lattice with two neighbouring atoms and the atomic and molecular orbitals at play.

A CNT is, **morphologically**, a layer of graphene, conceptually rolled around into a seamless cylinder. It is defined in the same manner, starting with an infinite graphene sheet, with

certain delimitations. Since a hexagonal lattice is not isomorphic in every direction, it can be rolled in different directions with different results. A hexagon's 6-fold rotational symmetry reduces the possible folding directions to 60° , and within this window, mirror symmetry narrows it down to half. This simplification leaves a 30° wedge of possible discrete folding directions, represented in a chirality map (Figure 5). Together with the width of the ribbon (i.e. circumference of the tube to be), these two parameters define unique CNTs. Mathematically, these are represented by the direction and norm of the chiral vector C_h . Originating at the vertex of the graphene wedge ($x = 0$; $y = 0$), it is composed of multiples (n,m) of 60° -disparate unit vectors (a_1, a_2) that navigate the lattice. Its length is the tube circumference $|C_h|$, its angle (to x) is the chiral angle θ , and its normal is the tube axis T. All this information can be trigonometrically derived from the (n,m) pair and the C-C bond length. Figure 5 shows an example $(9,3)$ C_h , the ribbon it defines (red dashed seems), and the resulting CNT. $(n,0)$ tubes are called *zigzag* ($\theta = 0^\circ$) (Figure 6a), $(n = m)$ are *armchair* ($\theta = 30^\circ$) (Figure 6b), and anything in-between is *chiral* (Figure 6c).

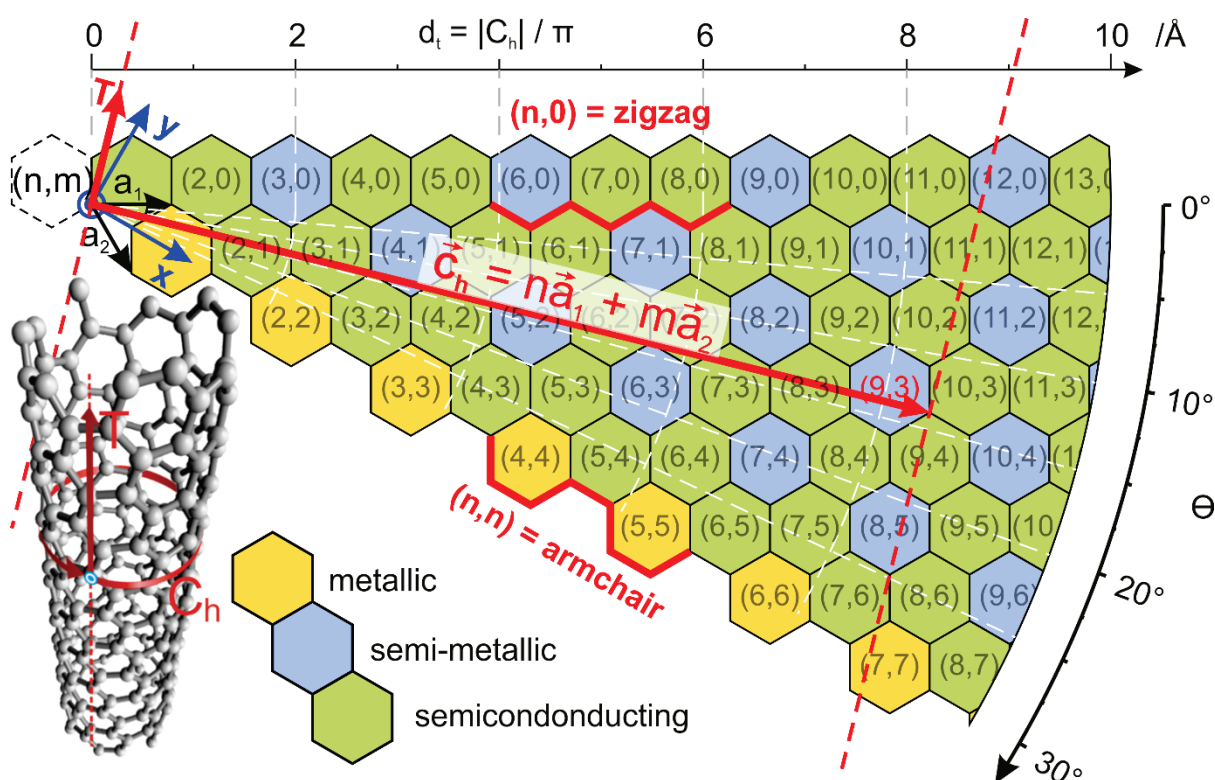


Figure 5 - CNT chirality map. 30° wedge of a symmetry-simplified infinite graphene sheet, defined by absolute (x,y) coordinates and unit vectors (a_1, a_2) . Tube-defining parameters C_h , T , d_t and θ are represented. Colour code key represents band gaps.

Until this point, CNTs of undefined length have been conceptualised, given their quasi-one-dimensionality and translational periodicity along the tube axis. Description of local CNT

morphology can be further axially expanded with the tube length; and radially, with the number of walls. Thus, as opposed to a single-wall CNT (SWCNT), a multiwall CNT (MWCNT) consists of a variable number of nested concentric tubes (Figure 6e), separated by a distance (0,32-0,35 Å) akin to that of interplanar separation in graphite (0,34 Å)^[16]. Double- and triple-wall CNTs are special cases of MWCNTs, presenting certain special properties. MWCNTs are multi-chiral, meaning that each nested tube has a different chirality, and are thus non-commensurate. These considerations are per the conventional *Russian Doll* model, whereas the lesser-known *Parchment* model, considering a single rolled-up sheet of graphene, can also be considered as a MWCNT. Finally, CNTs can be open at their ends or seamlessly capped with structures resembling half fullerenes (Figure 6d).

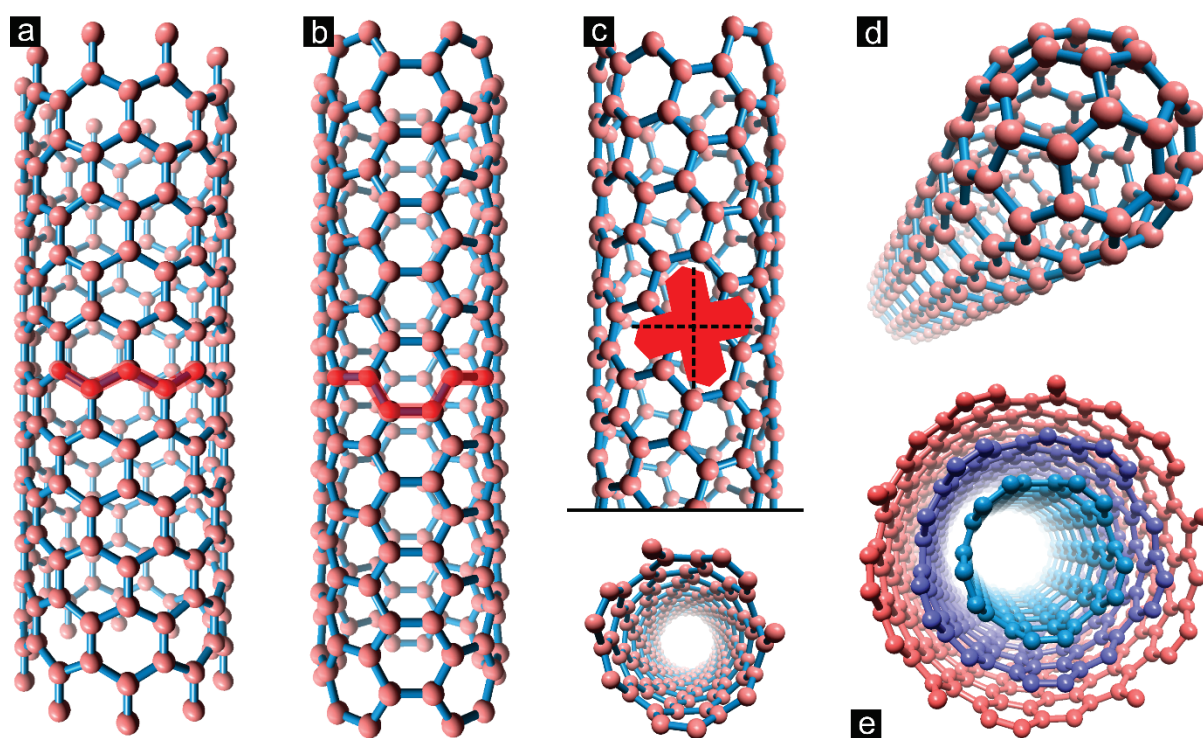


Figure 6 - CNT morphology: zigzag (a), armchair (b) and chiral tubes; capped tube end (d); MWCNT (e).

Beyond crystal structure and wall count, CNTs can possess a variety of short- and long-range order. Short-range order can be limited to separate tubes, bundles, ropes or agglomerates. Long-range order can be described ranging from unordered/random entanglements of spaghetti-like tubes, to branched networks of tubes interconnected with Y-junctions^[17], to relatively ordered states: bamboo or cup-stacked CNTs^[18] are axially-successive, stacked tubes, open or capped at one end and conically nested at the other; vertically aligned CNTs (VACNT), also referred to as CNT forests, bear long-range perpendicularity with respect to

their support or free surfaces. A closer look at VACNTs, though, reveals local entanglements and wavy bundles^[19]. Finally, at the sample level, CNTs can be observed in powder form, mats (thin self-sustaining layers), and threads. The following physical properties correspond to the axial tube direction unless specified otherwise.

Electrical properties

Physically, a CNT's C_h , or its chirality, encompasses a wealth of properties. The ca. 0-2,5 eV band gap^[20] and metallic-semiconducting conductivity (Figure 5) have a non-monotonic (n,m) dependence. The previously described delocalised π -orbital electrons provide the conductance along the tube axis. Armchair tubes with $n = m$ are metallic (zero band gap), $n - m = 3j$ tubes are semi-metallic (very small band gap), the rest $(n - m = 3j \pm 1)$ are semiconducting^[21]. The semi-metallic tubes are considered as such given their very low band gap which room temperature is sufficient to overcome, exciting electrons from the valence band to the conduction band^[22]. Consequently, roughly one third of tubes are metallic. All of this variability in the electrical properties of a tube is a consequence of the orientation of the graphene lattice with respect to the tube axis, or the conduction direction, determining the density of electron states at the Fermi level^[23].

The band gap in CNTs inversely relates to the tube diameter or its square. This is visualised in the Kataura plot, with several hyperbolic branches^[20]. Expanded to MWCNTs, their multi-chiral walls statistically contain at least one metallic tube, making all MWCNTs metallic^[24].

Carbon nanotubes are ballistic conductors, meaning electrons travel unscattered along the tube. Thus, assuming ideal contacts, the quantum conductance (G) of a metallic armchair nanotube is $G = G_0 N$ (Landauer formula). With conductance quantum $G_0 = 2e^2/h$, transmission probability $T = 1$ (no scattering), and two conduction channels N (sub-bands which cross the Fermi level), $G = 2G_0 = 6,45 \text{ k}\Omega^{-1}$ ^[23]. Excellent carrier mobility of $\sim 100.000 \text{ cm}^2 \text{ V}^{-1} \text{ s}^{-1}$ ^[25] and maximum current density of $\sim 4 \times 10^9 \text{ A cm}^{-2}$ ^[26] also exceed 10^3 -fold those of silicon and copper, respectively.

Because of these predictions and calculations, CNTs could extend Moore's law. The stated two-yearly doubling in the number of components per integrated circuit has held true for the past half century. As of 2012, the cadence has slowed down by half a year and is expected to

saturate. However, the size, conductivity and switchable conductance of CNTs have already proven their viability in future electronics^[27,28].

Since CNTs behave like metals, and electrical and heat transport both involve free electrons, the ballistic conduction in CNTs also provides them with superior thermal conduction, ca. ten times that of copper^[29].

Mechanical properties

Despite a slight influence of the chirality^[30], it is their network of covalent sp^2 bonds and cylindrical shape confer CNTs the highest *specific* strength and stiffness of any material known to date. SW- and MWCNTs have been theoretically predicted and experimentally observed to have Young's moduli around 1 TPa^[31] and tensile strengths of ca. 50-150 GPa^[32]. Yet these magnitudes attain greater significance when normalised to the corresponding density (ρ). Figure 7 shows the experimental specific stiffness vs specific strength of relevant structural materials.

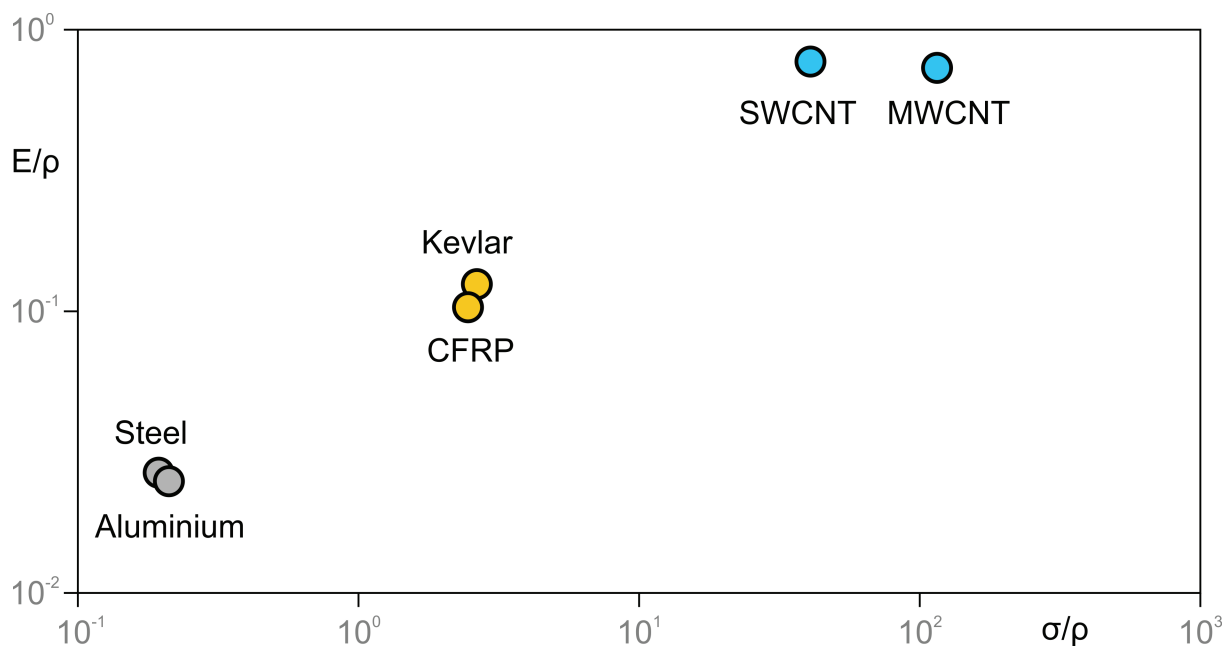


Figure 7 – **Experimental** specific stiffness (E modulus / density) vs specific strength of CNTs compared to those of relevant competing structural materials (CFRP: carbon fiber reinforced plastic). Double logarithmic scale.

SWCNTs have a compression yield point of 25 GPa, after which a transformation shifts this to at least 55 GPa with a bulk modulus of up to 546 GPa, harder than single-crystal diamond (420 GPa)^[33]. Radial hardness, as with other properties, is much lower. However, CNTs

demonstrate a lubricating effect in contacts, due to rolling and weak shear interactions between deformed walls, similar to the layers in graphite^[34].

CNTs have thus already disrupted materials engineering and industry, with around two thirds of their production oriented towards composites^[14]. One noteworthy application, previously an Eiffel tower-inspired reverie of the late 1800s and now at the centre of serious research efforts, is the construction of a space elevator. Modern concepts of this idea, a tensile tether stretched between earth's surface and a trans-geostationary orbital counterweight, indicate that CNTs are a possible candidate for the strength-to density requirements, taking the sci-fi pipe dream into the realm of physical plausibility.

Optical properties

Carbon nanotubes exhibit numerous interesting and useful optical properties including near-infrared photoluminescence (SWCNTs)^[35], electroluminescence^[36], record near-black-body absorbance (vertically aligned forests)^[7], Rayleigh scattering^[37] and Van Hove singularities^[38]. The latter is perhaps their greatest asset for their study. These quantised energy jumps in electronic transitions of the density of states (DOS) of SWCNTs result from one-dimensional confinement of electronic and phonon states, due to their described morphology^[37].

The corollary of this phenomenon is inelastic light scattering, by which an incident photon, matching a Van Hove singularity in the DOS of the valence and conduction bands, produces an up- (anti-Stokes) or downshifted (Stokes) emission frequency upon relaxation. This so-called Raman effect, complementary to Rayleigh (elastic) scattering, is a very powerful tool through which the photophysical process underlying the emission reveals detailed information about the structure, environment and phase chemistry of a CNT sample. In addition to photons, absorbed or emitted phonons, magnons and plasmons are also involved in the scattering process, satisfying the conservation of energy-momentum. Since phonons are a governing factor in mechanical, thermodynamic and further properties^[39], Raman spectroscopy, with little to no sample preparation is a core characterisation technique for CNTs.

The resonant nature of this technique thus excites tubes with bandgaps matching the exciting laser energy, plotted as intensity spectra as a function of the incident to emitted frequency shift, or Raman shift^[40]. Across this shift are numerous vibrational modes, each characteristic

of specific CNT features, as well as other carbonaceous and non-carbonaceous species commonly present in CNT samples. Additionally, several harmonic and combinatorial overtones of said modes can be observed. The most important modes specific to CNTs are the radial breathing (RBM), G, D and G' modes (Figure 8)^[37].

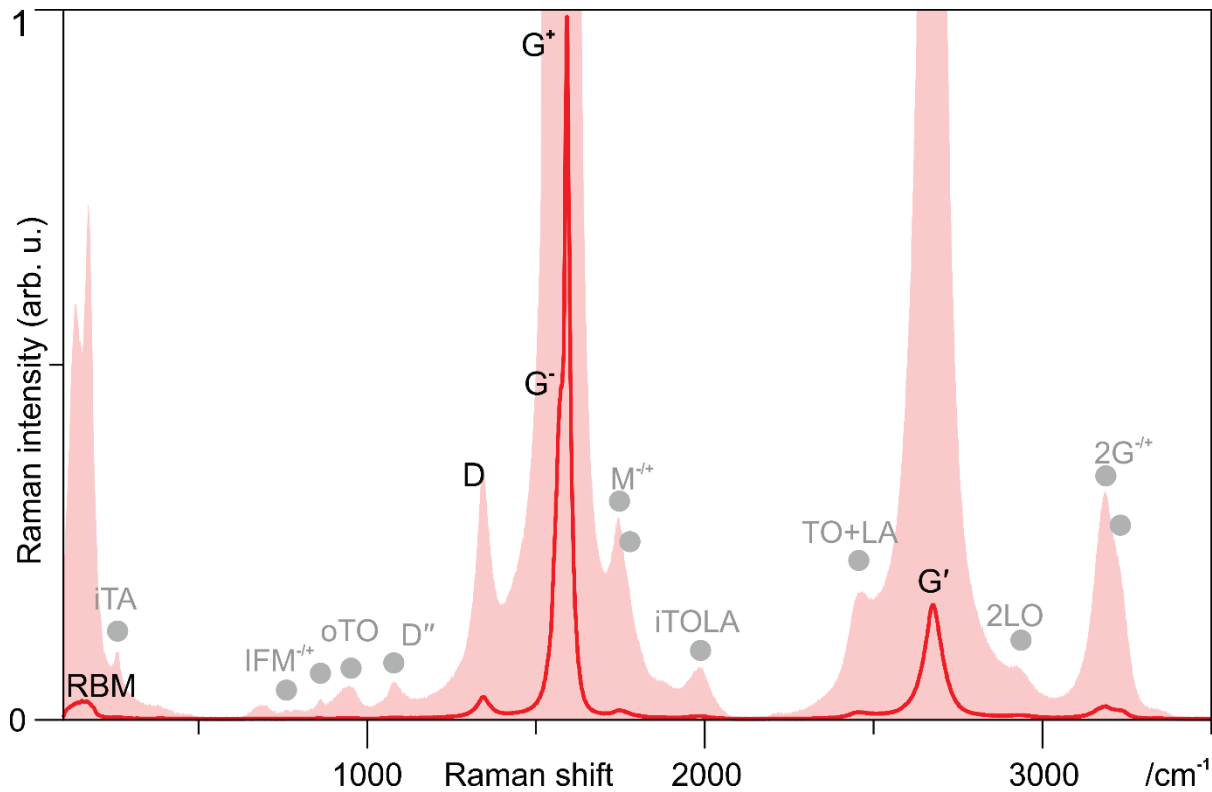


Figure 8 - Raman spectrum (red line) of synthesised SWCNT sample with expanded y-axis (pink surface) to observe more features^[37].

The radial breathing mode illustrates tube-radial atomic vibrations and is situated in the low frequency region of the Raman shift up to around 500 cm^{-1} ^[37]. This scattering event is of first order (single phonon) and its frequency is inversely proportional to the tube diameter (with different constants to account for tube-environment interactions). The RBM is characteristic of SWCNTs, but can also be observed in double- or triple-wall CNTs, above which the vibrations are dampened by the walls^[37].

The G (graphite) mode around 1580 cm^{-1} is analogous to that of graphite, with the peculiarity of splitting into several features due to curvature effects^[37]. The main contributions, G⁺ and G⁻, correspond to longitudinal (tube axis) and circumferential (tangential) vibrations^[37]. Their relative intensities can be used to roughly estimate the conductivity of a tube^[37]. The splitting of this first order mode is also extinguished by additional walls, and is thus absent in

MWCNTs^[37]. Building upon X-ray diffraction of graphite, the comparative peak width of G can be linked to the crystallinity of the sample^[41,42].

Activated by defects in the breathing modes of sp^2 -hybridised rings, the intensity of the second-order D mode is proportional to defect concentrations, but not to the amount sp^2 carbon^[42]. Thus, although sp^3 carbon has no D mode, sp^3 disturbances do contribute^[43]. The D mode is located around 1350 cm^{-1} ^[37]. Here, the comparative peak width can be linked to the variety of impurities present^[37].

The disorder-induced D mode gives rise to its overtone G' . This misnomer, found around 2700 cm^{-1} , arises from an electron backscattered by a second phonon, and, incidentally, is insensitive to defects^[44]. A perfect tube will produce G' intensities like that of G^+ ^[37].

In addition to the information provided by these individual modes, peak intensity or area ratios are commonly used to further characterise a sample. Thus, I_D/I_G is used to compare tube quality, particularly, attesting to the defect state of CNTs. High-quality tubes will have values approaching zero. Some commercial CNTs advertise quality based on a percentualised complementary of this ratio $Q = (1 - I_D/I_G) \times 100$, where low defects tend to 100 % Q ^[45]. Similarly, $I_{G'}/I_D$ can be used to indicate purity, since it eliminates chirality-dependent resonance and contaminant contributions that parasite the D-mode intensity^[46].

Limiting factors

With these superlative characteristics, CNTs are poised to outperform and dethrone many of materials science's historically top-ranking materials, from silicon to carbon fibre and diamond. However, the previous summary of prime physical CNT properties of have mostly considered ideal tubes, predictions and calculations thereof. Consequently, measured values can either deviate substantially from theory or be difficult to measure.

Within the accurately measurable magnitudes, several factors can limit, cancel or reverse any number of properties of single tubes, bundles or whole samples, creating a great divide between prediction and measurement well known to the CNT community. These factors can be intrinsic, inherent to the local tube, to sample geometry or chemistry; or extrinsic, processing-/handling-related.

The most basic intrinsic limitation can be the tube diameter. Small diameters cause extreme stress in the tube wall due to p_z orbital overlapping, in effect rendering very small tubes semiconducting. Large diameters, however, impair the structural cross-sectional rigidity of the tube, causing collapse and possible rupture at the bends, rendering the tube dual layer graphene^[47,48]. Extreme axial bending has the same effect as small diameters. Tube length, by extension, thus has the risk of entanglement and bending, causing disruption of the delocalised e^- cloud, charge carrier diffusion, chemical reactivity, functionalisation, and even strain and rupture.

Not to be confused with entanglement, agglomeration is a noteworthy impediment to performance, caused by tube-tube van der Waals forces. This increases inter-tube electronic coupling, diffusion, reduces mean free path and promotes poor contacting.

Crystal defects, or *local disorder*, are also serious chemical hindrances. Further limitations include impurities, or *environmental disorder*, such as amorphous, aromatic or other carbons, functional groups, and catalyst metals. This disorder can be present from the synthesis or be processing-related^[49].

Motivation 1 (see 2 Motivation and goals)

The sp^2 -conjugated lattice of CNTs is strongly bonded, yet not free of defects. Local disorder includes topological perturbations such as vacancies (Figure 9a), interstitials, adducts and polygonal distortions such as pentagons, heptagons, octagons and combinations thereof (Figure 9b)^[49]. Most of these defects can be short-lived intermediate consequences of one-another or more energetically favourable states. Figure 9c shows the effect of Thrower and Dienes defects on the long-range order of the lattice.

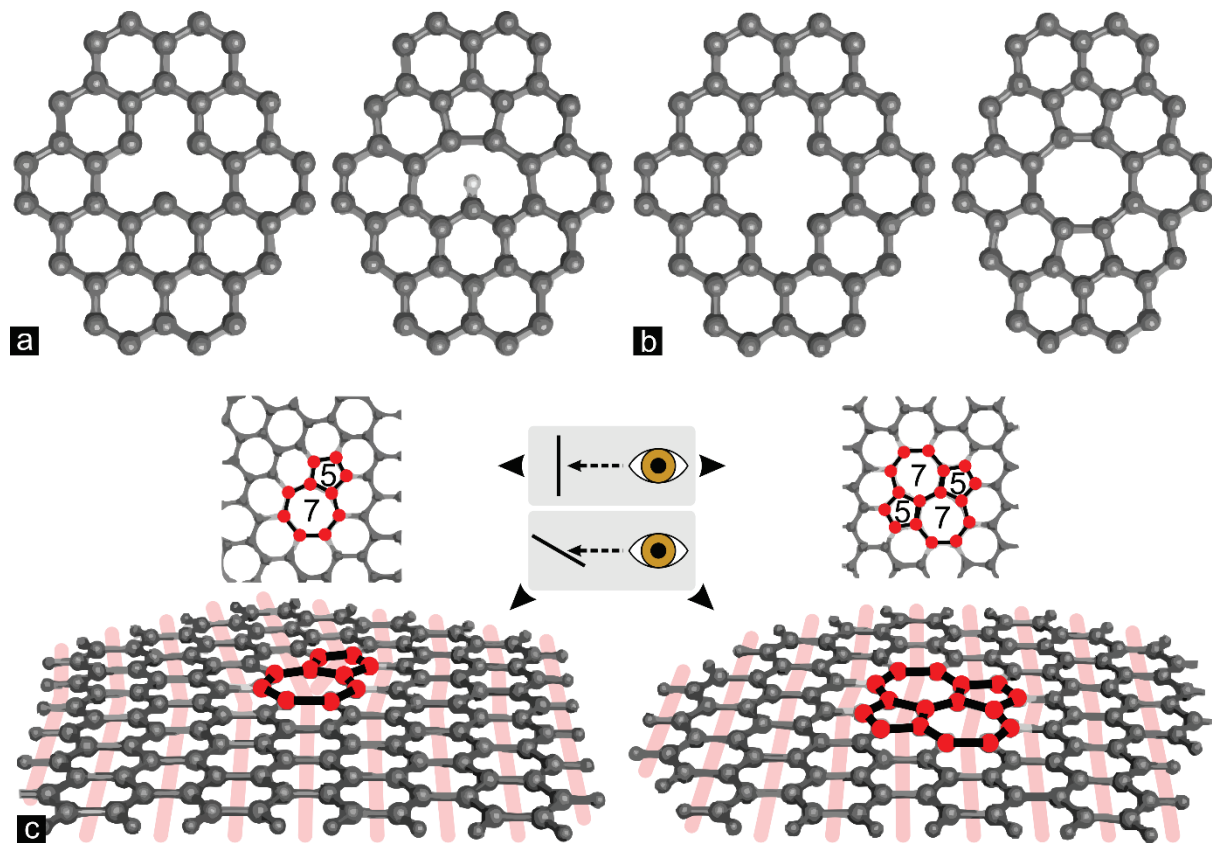


Figure 9 - Examples of local disorder in CNTs. Mono- (a) and di-vacancies before and after reconstruction (H-termination of the remaining dangling bond in (a)). (c) Single (Thrower) and double (Dienes) 5-7 defects and their effect (left), or absence thereof (right), on long-range order (perpendicular and angled perspectives with cell guidelines). Adapted from [49].

Processing and handling can cause most of the above complications. Poor dispersing, incapable of surmounting agglomeration, will cause higher contact resistance. However, energetic dispersion techniques such as ultrasound and centrifugation are known to cause damage to the CNTs, i.e. defects and impurities^[49]. Synthesis techniques must be fine-tuned to avoid or reduce the presence of metal catalyst particles and other impurities. Characterisation techniques using electromagnetic radiation, such as electron microscopes, Raman spectrometers and ion beams are known to damage CNTs^[50–55]. A very common MWCNT failure mode is telescopic disassembly, or *sword-in-sheath* mode, especially present in covalently-bonded MWCNT-matrix composites, a bond stronger than the van der Waals forces keeping the tubes nested. More generally, inter-tube load transfer, whether nested or adjacent, is a typical failure mode^[56–59]. An example of the latter, CNT threads fail to sustain loads comparable to that of single tubes (although improvable with radiation-induced cross-linking), due to tube pull-out^[60,61].

1.3. Synthesis

Growth

CNT synthesis can be broken down into carbon atomisation, transportation, nucleation and growth stages. The growth itself is a bottom-up process consisting in self-assembly of carbon atoms. The driving force for self-assembly can be random, collision-based within the mean free path of the atomic and molecular displacement, or through catalytic adsorption and precipitation. Let's consider nucleation and growth together as an actual growth system, with the necessary carbon and conditions for growth pre-existing.

sp^2 hybridisation, being the ground state of carbon systems, is the most stable and energetically favourable even at high temperatures^[49]. This also seems to be the case for tube configurations, which reduce the amount of edges, dangling bonds, and streamline the carbon input with quasi-1-D growth^[62,63].

Catalytic growth

Growth can involve a catalyst, usually a metal seed, not to be confused with various catalytic agents that can also be involved such as gases and substrates. These catalysts have traditionally been 3d valence transition metals (e.g., Fe, Ni, Co), but noble metals (Au) and *poor* metals (In, Pb) have also been proven^[64]. Finally, various ceramics, semiconductors and hybrid metal/metal oxide systems can catalyse tube formation^[64]. There is no scientific consensus on the exact growth mechanisms, save for a few models, also called modes. Most commonly referred to are the tip and base growth modes (Figure 10), derived from supported catalyst growth by chemical vapour deposition^[63,65–67].

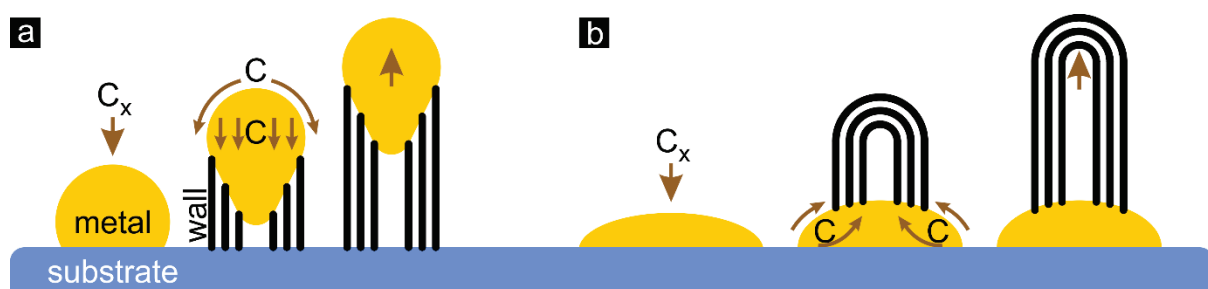


Figure 10 - Tip (a) and base (b) growth models. C_x are the various precursor species.

Both involve carbon solution in (substrate-supported) molten metal particles and diffusion up to saturation and sp^2 precipitation. In one case, weak metal-substrate interaction (low wettability) allows the carbon to precipitate at the metal/substrate interface and detach the

particle, with sustained growth at the tip^[66,68]. With high wettability, this does not occur and precipitation takes place at the free surface, initially as a dome, sustained as a cylinder pushing up from the metal at its base^[69].

CNT growth can be suspended (with consequent deposition) or substrate-bound. A more general substrate-free definition can thus be extended to physisorption or chemisorption of carbonaceous species in a molten metal particle (resembling the base model, with no base or tip to distinguish from) involving vapour- or solid-liquid-solid (VLS and SLS) mechanisms that consist in the adsorption of vapour/solid. Through initial precipitation, encapsulation of the particle or partial dissolution of fullerenes, outwards growth occurs due to layer instabilities and the formation of critical nuclei^[62]. The number of walls and tubes per particle depends on the metal, its particle size and a body of experimental parameters.

Catalyst free growth

All carbon systems were actually among the pioneering works of CNT synthesis^[11,70]. Carbon nanotubes have been shown to self-assemble from nanodiamond particles, coalescing fullerenes and various sp^2 systems driven by curvature around carbon agglomerates or on graphitic surfaces^[62,64].

Synthesis techniques

Let's now connect the physical growth models to their experimental realisation. An atomised carbonaceous input is therefore required in a protective atmosphere (carbon and oxygen are very reactive), generally combined with elevated temperatures and controlled pressures. The carbonaceous feedstock can be solid, liquid or gaseous, requiring vaporisation, spraying and/or disproportionation. This transition is brought on by different energy sources such as electric arcs, plasma, heat, laser radiation or combinations thereof.

Methods can be judged upon tuneable wall count (SW-/MWCNT), diameter and chirality, as well as quality (low defect density), purity (carbonaceous, catalyst or other), yield, scalability, energetic efficiency and cost. In the following is a summary of the main synthesis methods: arc discharge (Arc), chemical vapour deposition (CVD) and laser ablation (LA).

Arc discharge

Iijima and co-workers were able to convincingly image (MW)CNTs for the first time when analysing fullerene soot, produced in an arc discharge (Arc) reactor^[11]. This first method for tubular fullerene synthesis involved vacuum electric arcing between two high-purity graphite electrodes (Figure 11). As a result, the sublimated anode builds up on the cathode as a black powdery soot, yielding up to a 30 wt% mix of SW- and MWCNTs.

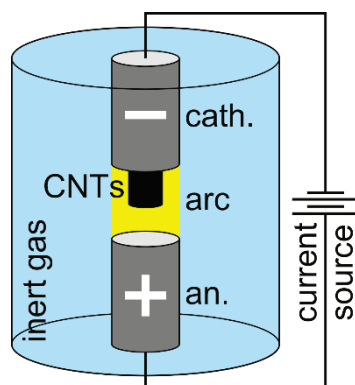


Figure 11 - Arc discharge schematics

The CNTs undergo collision-based atmospheric growth in the field lines of the electric arc. The low tuneability and quality are due to the energy-intensive wandering arc dynamics, dictated by the graphite purity, the evolving electrode shape (consumption vs deposition) and the resulting field lines.

Chemical vapour deposition

First confirmed in 1993 by José-Yacamán et al., chemical vapour deposition (CVD) consists in the substrate-mediated disproportionation of an organic gas flow in a heated reactor (Figure 12)^[71].

This method has found wide-spread adoption due to its simpler operation and cost and energy efficiency. Indeed, aside from the fact that the only energy input is heat, extracting carbon from a decomposing gas can be ten times less energy-consuming than graphite vaporisation^[72].

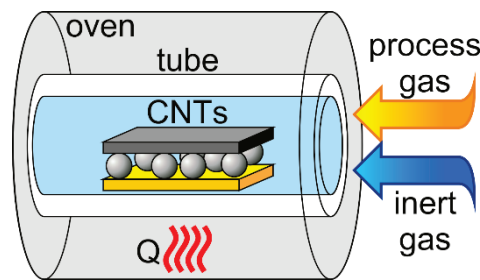


Figure 12 - CVD schematics

Laser ablation

Guo and co-workers developed laser ablation for CNT synthesis in 1995^[73], in which the energy for carbon atomisation is supplied by a high-power laser impinging on a carbonaceous target inside a tube furnace (Figure 13) which provides the ambient energy for growth, atmospheric and/or substrate-bound.

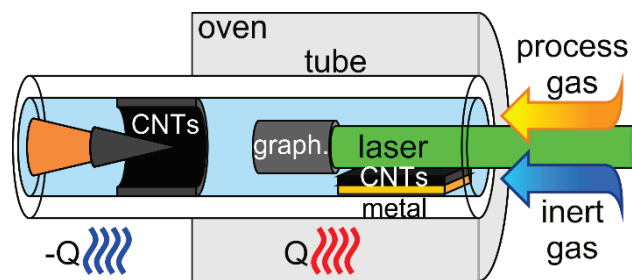


Figure 13 - Laser ablation schematics.

Apart from this heat, atmospheric growth is controlled by mean free path parameters: pressure, tube geometry, gas flow, laser energy^[62]. This suspended growth can occur in the reflected plume opposite the target, in its proximity, or carried by the protective gas flow (usually in the same direction as the laser, to avoid interference). These tubes can thus land on substrates in different locations in the chamber and on the chamber walls. The latter can be aided by cooling (air or water) at extremity of the chamber tube, exit the furnace.

Substrate bound growth can be catalysed by physisorption in metal, usually a thin layer that dewets at the furnace temperature to produce nano-/microparticles and nucleate the growth. Suspended growth occurs in laser ablation of graphite, or SWCNTs can be catalysed by metal powder mixed into the target^[74].

Pulsed laser deposition of SWCNTs

The advantage of laser ablation is the temporal separation of the target atomisation and the tube formation stages, providing a better control of the growth conditions^[62]. Even more so,

when using a pulsed laser, in what is termed pulsed laser deposition (PLD), allowing for the ablation products to develop out of the beam, between each pulse. Continuous wave lasers can ablate carbon without added heat from a furnace^[75], yet pulsed lasers offer higher peak powers in discrete pulses and better control of the plume dynamics^[62].

For these reasons, and because PLD produces high yields and a more narrow diameter distribution of CNTs^[76], the method has been thoroughly studied. Table 1 shows a summary of PLD parameters and their relation to CNT yield and diameter, in the form of the dependence of the latter in degree (from unknown to pronounced) and type (linear / logarithmic / complex / peaked).

Table 1 - Process parameter Influence on SWCNT abundance and diameter in PLD ^a. Adapted from^[62].

		Yield		Diameter			
		Dependence		Dependence			
Parameter		Degree	Type	Refs.	Degree	Type	Refs.
Target	Precursor	±		[77,78]	?		
	Morphology	±		[79]	?		
Catalyst	Quantity	+	peaked	[80]	-		[80]
	Type	+	complex	[74]	+	complex	[81–83]
	Mixture	+	peaked	[74,84]	+	log	[83]
Atmosphere	Temperature	+	peaked	[82,85,86]	+	linear	[82,83,87]
	Gas	+		[86,88]	+	complex	[83]
	Pressure	+	peaked	[86,89]	+	log	[83,90]
	Gas flow velocity	+	peaked	[91,92]	- *		[93]
Laser	Pulse count	±		[94]	?		
	Plume confinement	±		[95]	± *		[95]
	Frequency	±		[96]	- *		[97]
	Combined beams	±		[98]	- *		[99]
	Pulse duration	±		[100]	- *		[100]
	Wavelength	±		[101]	- *		[101]
	Fluence	+	peaked	[91,102]	± *		[102,103]

^a Key: pronounced (+), observable (±), negligible or none (-), unknown (?), cannot be unambiguously attributed (*), log (logarithmic), peaked (local maximum/peak – see Figure 14).

This has brought research to a set of parameters that can be observed throughout PLD literature as a window of optimal temperature, gas flow velocity, pressure and laser fluence, with respect to CNT abundance (Figure 14). These four parameters seem to peak and intersect around 1200 °C, 1 cm/s, 65 kPa and 1,5 J/cm².

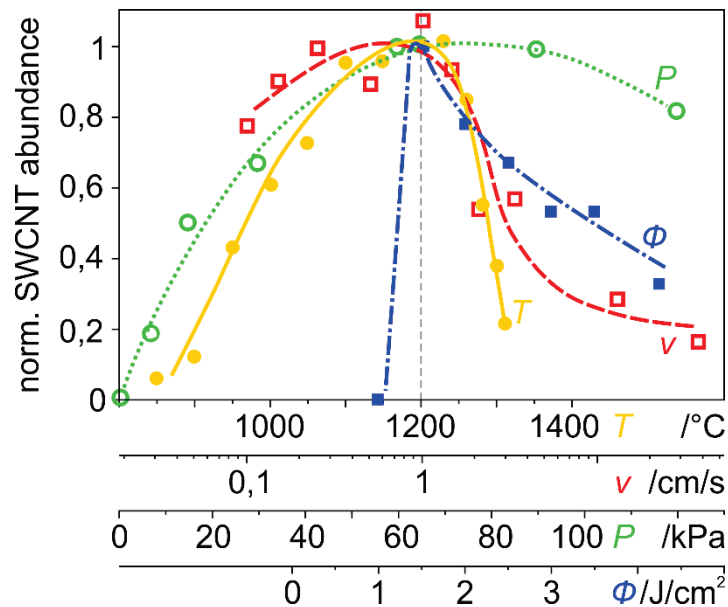


Figure 14 – Influence of the furnace temperature T (solid circles, solid line), the carrier gas flow velocity v (open squares, dashed line) and pressure P (open circles, dotted line), and the laser fluence ϕ (solid squares, dash-dot line) on the relative SWCNT abundance in the laser evaporated soot^[91]. Each curve represents the effect of variation of one parameter with all other specified in Table 1 constant. Adapted from^[62].

The laser fluence and the furnace temperature are responsible for the ablation of the graphite and metal mixture in the target. From this point on, the temperature, the gas flow velocity and the pressure, together, guarantee a sufficiently dense and displacing gas atmosphere for the ablation production to condense before reaching a solid substrate. The time scale of SWCNT growth by PLD can be mapped to roughly one second^[91,93,104–107], although tube geometry and gas flow parameters can delay deactivation and quenching. Figure 15 is a loose schematisation of the results summarised in^[62].

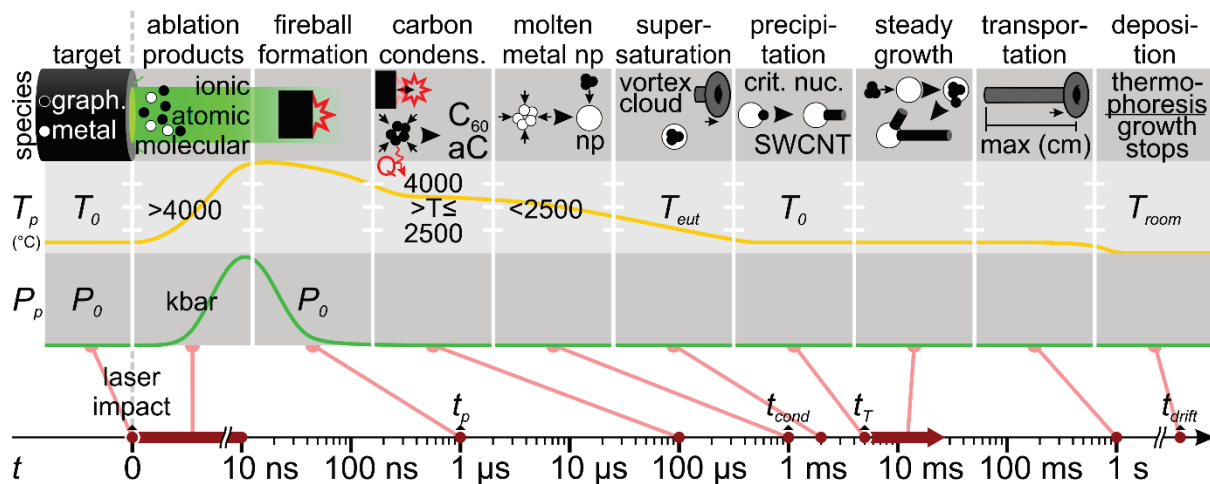


Figure 15 - First second of SWCNT life: time (t) scale of the ablation products, their temperature (T_p , yellow curve) and their pressure (P_p , green curve). Initial temperature (T_0) and pressure (P_0), (any) fullerene (C_{60}), amorphous carbon (aC), fireball time (t_p), nanoparticle (np), condensation time (t_{cond}), eutectic temperature (T_{eut}), thermal equalisation time (t_T), room temperature (T_{room}). Summary of the time scale and rough qualitative curves of the data described in [62,91,93,104–107].

The ionic, atomic and molecular ablation products are produced above the sublimation temperature of carbon and at a few kilobars, in under 10 ns; up until 1 μ s, a fireball forms and the pressure relaxes to initial levels; at 100 μ s, the fireball moves away from the target with the temperature returning below sublimation and carbon condenses to fullerenes and amorphous carbon, releasing heat that maintains the temperature above 2500 $^{\circ}$ C; metal condensation into molten nanoparticles, which requires an order of magnitude longer, ca. 1 ms, begins to solve the carbon upon contact; at 2 ms, most carbon ablation products are condensed, in a ring vortex-shaped cloud at the eutectic temperature of the metal-carbon mix. Supersaturation and the driving force for catalytic graphitisation set in; the temperature returns to initial values only after 5 ms and graphitic precipitation sets in which, upon attaining a critical nucleus, preferentially adds atoms to the circumference and begins CNT growth; steady state growth sets in by 5 ms and continues until quenched at a cold collector through a thermophoretic force.

Alternative carbon feedstocks

Given the abundance of carbon sources, science has explored a wide variety of them for CNT synthesis amongst vegetable (camphor, turpentine oil, eucalyptus oil, palm oil), mineral (coal, coal gas), nanocarbons (C_{60} fullerenes, CNTs) and petrochemical carbons (heavy oil residue, tire powder, carbon fibre, carbon black, asphalt).

Fluid catalytic cracking catalyst residue (FC3R), a carbonaceous reject of the petrochemical industry currently wasted in landfills, is a faujasite zeolite agglomerate covered in graphitic carbon. To understand the volume and availability of this material: FC3R is often referred to as catalyst coke (CC) and assigned to petroleum coke (PC) statistics. In 2014, the US alone produced roughly 320 M barrels of PC, of which 73 % was marketable (Figure 16), of which in turn 84 % was exported^[108] (60-90 USD/T (01/2015)^[109]). Yet, marketable coke must be relatively pure carbon; that is why CC, an indirect 2,7 % of every barrel of crude (Figure 16), with its high amounts of zeolite, is not considered as such. Spent FCC catalyst is the largest catalyst waste category in refineries^[110]: in 2006, 0,5 MT of FCC catalyst were being used worldwide^[111], which will inevitably end up in landfills due to lacking technology, profitability and regulation.

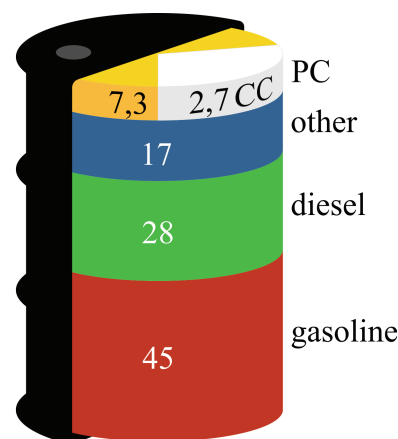


Figure 16 - Approx. 2014 U.S. crude barrel yield (%) ^[112]: of the 10 % PC, 73 % is marketable and 27 % is non-marketable catalyst coke. Estimated from 2014 US production (3,2 B (10⁹) barrels of crude ^[113], 0,32 B barrels of PC ^[108] and 85 M barrels of CC ^[114]).

If the blossoming CNT industry is to develop into a sustainable one, alternative, renewable, reused or more environmentally friendly sources are to be found.

Motivation 2 (see 2 Motivation and goals)

2. Motivation and goals

This work was organised around identified challenges that, when addressed, would make the largest impact towards the improvement of this new and promising material, within the realm of feasibility with the techniques at hand. The following selected challenges were the motivation for their corresponding goals.

Motivation 1: Crystal defects, or *local disorder*, are serious chemical hindrances. Further limitations include impurities, or *environmental disorder*, such as amorphous, aromatic or other carbons, functional groups, and catalyst metals. This disorder can be present from the synthesis or be processing-related. CNT purity and quality have experienced asymptotic development and are a major impediment to technological breakthroughs.

Beyond synthesis tuning, the observed but understudied effect of laser annealing was studied, as a fast, contactless and ambient method to correct crystal defects and remove impurities, including those produced by processing and wear.

Goal 1 (see *Results and discussion* 4.1 and 4.2)

Motivation 2: Standard carbon precursors are of petrochemical or mining origin. If the blossoming CNT industry is to develop into a sustainable one, alternative, renewable or more environmentally friendly sources are to be found.

Promises of efficiency in CNT-based products should be accompanied by material sustainability, in order to imagine a future with volume production. FC3R is explored as carbon feedstock for CNT synthesis by pulsed laser deposition (PLD).

Goal 2 (see *Results and discussion* 4.3)

Goal 1 also has the virtue of contributing to Goal 2, in that it reduces the need for fine-tuned synthesis with high purity precursors, allowing for more robust synthesis using alternative carbon sources, followed by laser annealing, to achieve similar quality CNTs.

The binding principals of this work, and thus its title, thus consist in an all-laser approach to synthesise and anneal carbon nanotubes (Figure 17), towards efficiency and sustainability.

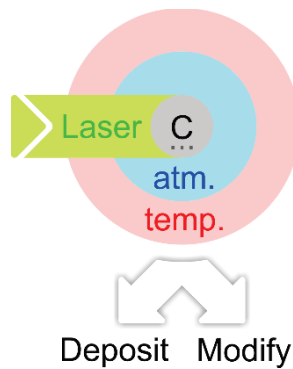


Figure 17 – Summarised global strategy and parameters to adress the defined goals. Title of the work: “Laser and carbon: nanotube synthesis and annealing”.

SWCNTs were chosen to be the main object of study and thus production, because of their simpler behaviour, predictable properties, and extra features and stronger resonance in Raman spectroscopy, compared to MWCNTs (see 1.2 *Properties*).

Pulsed laser deposition was selected to synthesise the SWCNTs due to its narrower diameter distribution, better control of the growth dynamics and capability to process complex carbon precursors (such as FC3R), compared to other methods (see 1.3 *Synthesis*).

Laser was used to anneal SWCNTs given the flexibility of the technique, the ambient conditions, the fast treatment times and scalability (see *Results and discussion* 4.1 & 4.2)

3. Materials and methods

3.1. CNT synthesis

Oven-laser apparatus: Pulsed laser deposition

CNT samples were synthesised by pulsed laser deposition (PLD), following the pioneering work by Guo et al.^[73], combined with Suda's et al.^[115,116] take on the procedure (Figure 18). Hereby, a carbonaceous target is vaporised inside a tube furnace, under a controlled atmosphere and temperature, by a high-power pulsed laser impinging on the target. The vaporised species then travel and deposit on a collecting surface.

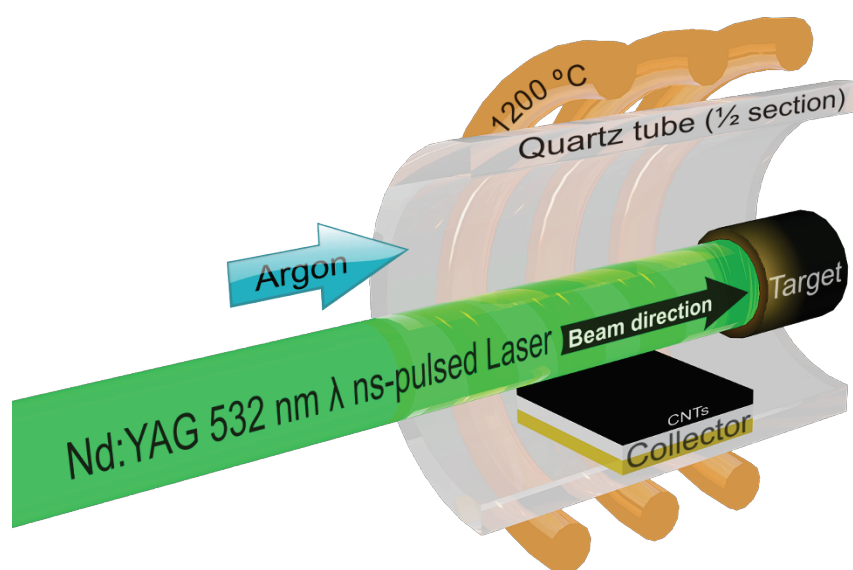


Figure 18 - Basic principles of pulsed laser deposition of carbon nanotubes

More precisely (Figure 19), a vertically-polarised, 532 nm wavelength-laser (solid state Nd:YAG Newport-SpectraPhysics Quanta-Ray 290) with a 10 ns pulse at 10 Hz was used as the radiation source. Its fundamental 10 mm diameter was then masked to 8 mm for a precisely irradiated area, higher power density and to stop reflections from re-entering the laser system. Figure 19 summarises the specifications with which the system was conceived.

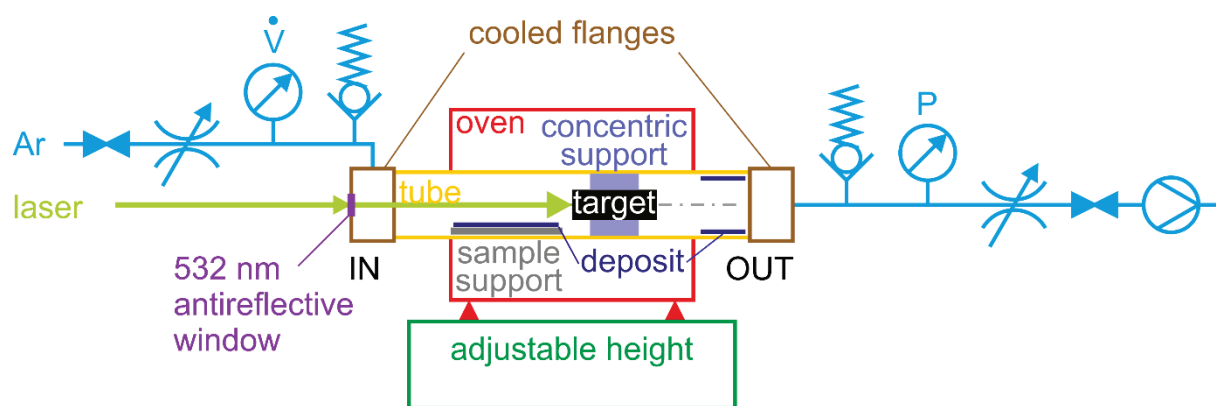


Figure 19 – Specification and functional schematics of oven-laser apparatus

The growth chamber consisted of a quartz tube (90 cm long, 29 mm interior diameter, 3 mm wall thickness), with two brass flanges on either side, screw-tightened with deformed static ring seals, for atmospheric closer. Due to the rubber seals, the flanges were air-cooled with ventilators. The gas and laser IN flange was equipped with an antireflective (532 nm) window and a gas inlet.

Inside the chamber and in the centre of the hot zone, the laser impinged on a carbonaceous feedstock (target) (Figure 20), held in place concentrically to the tube by a graphite holder with three alumina pins. The target holder was held in place by a graphite tray, that also held samples for CNT deposition (collectors). The assembled sample and target holders were inscribed in an exact 29 mm circle (inner tube diameter) to guarantee their absolute and relative positions. The pin assembly was pressure-based, and the graphite parts were machined, all in order to avoid using glue and ensure temperature resistance.

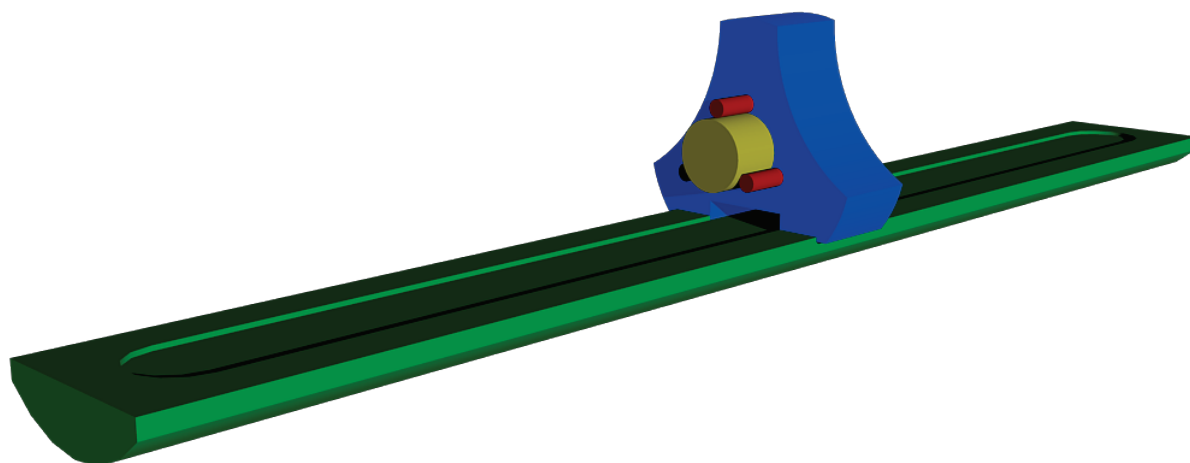


Figure 20 – Target and sample assembly: target (yellow) held by three alumina pins (red), force-assembled in the target holder (blue), carried by the sample tray (green).

Targets were fabricated from three different sources: machined graphite cylinders (\varnothing 8 mm x 5-6 mm); cold-pressed (same dimensions) blend of ball-milled (60 rpm) graphite and 1,2 at% metal (equal parts Ni and Co) catalyst powders (binary metal targets significantly increase yield^[117]); grinded and faceted FC3R rock, of appropriate shapes for the target holder.

CNT deposition occurred on the cooled quartz tube and a copper cone both at the OUT extremity, where CNT mats were peeled off. Deposition in the furnace hot zone also took place in the direct up- and downstream vicinity of the target vaporisation. Here thin films and cold pressed metals were placed on the collector tray. Thin films (materials and parameters in *Results and discussion* 4.3) were DC magnetron-sputtered on commercial SiO/Si wafers (500 ± 25 mm Si + 250 nm SiO₂) by physical vapour deposition (PVD).

On the **gas inlet** side, high purity argon (N6.0) was fed through a valve and a flow controller, with an emergency 1,5 Atm release valve. After exiting the chamber, the gas was run through another emergency valve, a pressure gauge, a needle valve and a close-off valve to a rotary pump.

A **tube furnace** with an alumina tube (60 mm inner diameter), carried the quartz tube chamber, centred and thermally isolated with wax foam. The weight of the chamber, however, was carried by steel supports on each flange. These align the chamber with the laser, leaving two degrees of freedom along and around said axis. These degrees, however, have no bearing on the correct laser impact, thanks to the parallel beam and the centred

target. The oven was loaded on a hydraulic table with adjustable height, to adapt to the existing laser system's fixed height and avoid the use of further optics.

Experimental run-through

An experimental run-through consists in target and/or collector fabrication, laser orientation (coaxially centring on both IN and OUT flanges, thus guaranteeing a beam path through the target), target and sample tray loading and positioning (assembly and insertion with a mm-graded rod), chamber sealing, vacuum pump-down (rough vacuum), oven heating ramp (5 °C/min up to threshold), temperature threshold (700-1200 °C), gas inlet (Ar N6.0), gas flow and pressure setting ($0,3 \leq p \leq 1,5$ bar, $1 \leq Q \leq 10$ sccm), laser setting and radiation ($3 \leq P \leq 12$ W), and inverse-order shut down during temperature ramp-down, under vacuum. A glimpse of the actual experimental setup is shown in Figure 21.

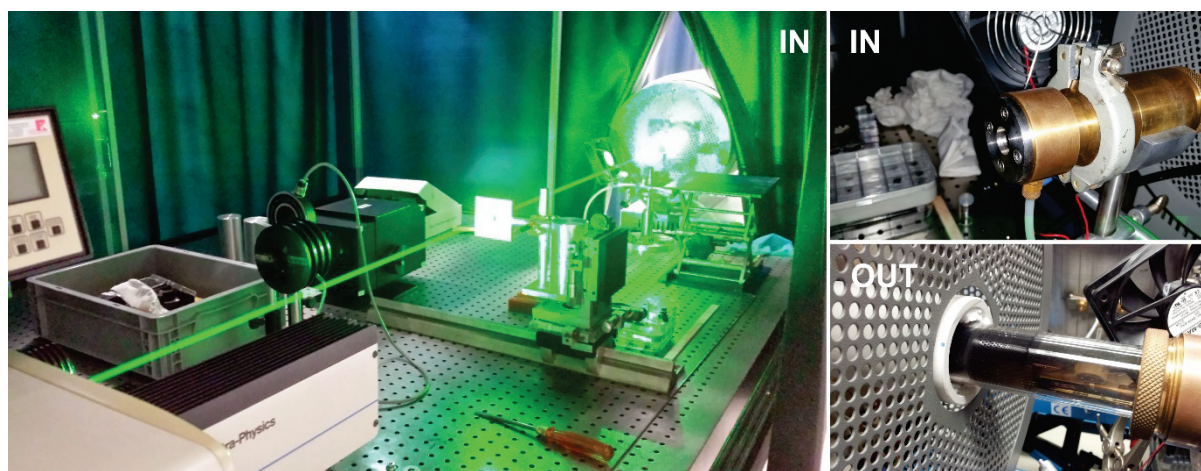


Figure 21 – Experimental PLD oven-laser apparatus with laser and gas IN and OUT sides. CNT deposition can be observed on the quartz tube OUT side.

3.2. Processing

Laser radiation for CNT annealing was produced at two different scales, each with a different laser system. At μm scale, the laser of the Raman system described in 3.3 *Characterisation* was used in ambient conditions. Attenuation levels were achieved through a combination of the built-in filters and a progressively metal-coated disc, rotated to specific levels of transmittance.

At the mm scale, a second system was used with a 940 nm (1,39 eV) wavelength diode laser (500 W LDM 500-20, Laserline). For sample scanning, this laser was mounted on a three-axis CNC system (Bosch-Rexroth).

Mechanical damage was introduced into CNT samples using laboratory-scale shear mixing, an ultrasound bath and centrifugation.

3.3. Characterisation

Rough sample characterisation was performed on a dual-beam workstation (FEI Helios NanoLab 600): scanning electron microscopy (SEM) at acceleration voltages of 5-15 kV was used for bare imaging; a focused (Ga^+) ion beam (FIB) provided in-situ milling for sub-surface access. Approximate species identification/distinction was possible with through-the-lens, secondary electron and energy dispersive X-ray spectroscopy detectors.

Very local sample resolution relied on transmission electron microscopy (TEM; JEOL 2100F) at 200 kV on drop-casted CNT dispersions in ethanol, on a copper grid with a lacey carbon film (Gatan).

High-volume and -sensitivity phase characterisation was conducted with X-ray diffraction (XRD; X'Pert MPD) with $\text{Cu K}\alpha$ radiation in a θ - θ geometry configuration; and Raman spectroscopy (Renishaw inVia) at 532 nm (2,33 eV) continuous wave excitation (Figure 22). A 50 \times objective with a numerical aperture of 0,75 produced a spot size between 2,9 and 25,1 μm , discussed in the results.



Figure 22 - Renishaw inVia Raman system. Closed sample chamber and system (left) and opened (right).

Thermogravimetry (TG) and differential scanning calorimetry (DSC) were carried out on a Netzsch-Gerätebau Jupiter 449.

Electric resistance measurements were performed on a micromanipulator stage (Signatone S-1160B-8N), with silver needles as contacts, mounted on 3-axis μm adjustment screws (Signatone S-725, 10 μm resolution). Optical calibration of contact position was done through an in situ optical microscope (Leica StereoZoom, 1,5 \times objective, 10 μm resolution)

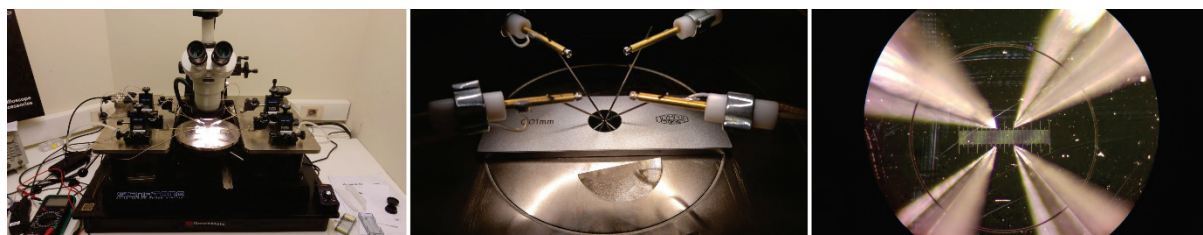


Figure 23 – Electrical resistance measurement setup (left), close-up of contact calibration on a micrometer ruler (centre), view through microscope (right).

Gas adsorption was studied on a gold-coated water-cooled microbalance (MDC SQM-310) with an AT-cut ($\approx 35^\circ$) quartz crystal in a steel vacuum chamber, injected with hydrogen through a needle valve with pressures monitored by a capacitive gauge (MKS instruments Baratron).

4. Results and discussion

The results presented (embedded) in the following are full, self-contained papers (with references) and have been published in an international peer-reviewed journal.

4.1. In situ tracking of defect healing and purification of single-wall carbon nanotubes with laser radiation by time-resolved Raman spectroscopy

N. Souza, M. Zeiger, V. Presser, F. Mücklich

RSC Advances, July 08, 2015

DOI: 10.1039/C5RA09316C

RSC Adv., 2015, 5, 62149-62159

12 pages

This work is the first of two parts addressing **Goal 1**.

Reproduced from Ref.^[55] with permission from the Royal Society of Chemistry.

Accessible online at <http://xlink.rsc.org/?DOI=C5RA09316C>

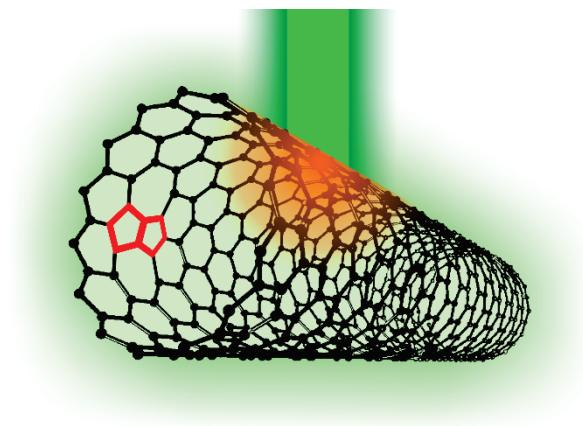


Figure 24 - Graphical abstract: defective (red pentagons) SWCNT irradiated with green (532 nm) light, producing heat (orange glow).

Cite this: *RSC Adv.*, 2015, 5, 62149

In situ tracking of defect healing and purification of single-wall carbon nanotubes with laser radiation by time-resolved Raman spectroscopy†

N. Souza,^{*a} M. Zeiger,^{ab} V. Presser^{ab} and F. Mücklich^a

Defects and impurities in carbon nanotubes (CNTs), inherent to all synthesis routes, are generally addressed by thermal and/or chemical post treatments. These require atmosphere control, time-consuming temperature ramping, chemical handling, and often incur further defects. Furthermore, certain applications require nanotube treatments, such as dispersion, that cause further unwanted damage. Laser radiation was found to drastically increase purity, crystallinity and mean inter-defect distance while reducing defects, as indicated by Raman spectroscopy, effectively annealing our single-wall CNTs. Laser power density and radiation times, in other words, fluence, were optimised. When applied to CNTs with mechanically induced defects, these were almost fully eliminated. In addition to the tuned annealing of CNTs, unintentional sample modification can occur during Raman measurements if the influence of the power density and the exposure time are underestimated or disregarded. Fast laser radiation times and simple manipulation outdo common purification treatments. Additionally, selective shape and site-specific parameters come into play such as interference patterns. Such arrangements of alternating tube quality, that is, in a CNT mat, could be interesting for preferred electronic conduction paths and find applications in, for example, interdigitated electrodes or sensors.

Received 18th May 2015
Accepted 6th July 2015

DOI: 10.1039/c5ra09316c

www.rsc.org/advances

1. Introduction

Largely unnoticed for decades after their initial 1952 discovery by Radushkevich and Lukyanovich,¹ carbon nanotubes (CNT) were presented to the world in 1991 by Sumio Iijima.² Since then, CNTs have struggled to meet the predictions of theoretical models touting unprecedented properties, such as mechanical strength or electrical conductivity.^{3–5} The majority of the shortcomings have been due to the low crystallinity and purity of the produced material, thus partly directing research at controlling said characteristics. Although certain applications require defective CNTs (*e.g.*, gas sensing,⁶ polymer matrix composites⁷), many benefit from defect-free tubes (*e.g.*, processors,⁸ metal matrix composites⁹). In either case, the performance of the end product is highly sensitive to the crystallinity and purity of the CNTs.

Inherent in-sample CNT-synthesis byproducts (impurities, or *environmental disorder*) include transition metals used as catalysts in the carbon feedstock and/or substrates. Besides

various functional groups, as-synthesised samples most commonly contain other forms of carbon such as graphite, fullerenes, onion-like carbons (OLC), amorphous carbon and hydrocarbons.¹⁰ These secondary phases are found in and around the tubes and at their extremities, in the form of nanoparticles or larger aggregates, and can represent up to 90 wt%.¹¹

Despite their strongly bonded sp²-conjugated lattice, intrinsic CNT defects (*local disorder*) are not uncommon. Certain topological perturbations are more energetically favourable than others, some are short-lived intermediate states that evolve towards more stable configurations, and others can migrate, merge, interact, or even annihilate. Equilibrium concentrations of vacancies, interstitials, adducts, and polygonal distortions (pentagons, heptagons, octagons, and combinations thereof) range typically between 10^{−33} to 10^{−15} for CNTs synthesised by chemical vapour deposition (CVD) at 1200 °C.¹⁰ In single-wall CNTs (SWCNTs), defect migration barriers can be as low as 1 eV (vacancy) at temperatures as low as 100–200 °C,¹² and carbon interstitials are highly mobile at a cost of 0.1 eV.¹⁰ At 3.5 eV net cost, Dienes defects¹³ (double Thrower defect:¹³ pentagon–heptagon pair) can exist up to an average of 1 μm^{−1}.¹⁰ These energy barriers are very small considering the high amount of thermal energy available during certain synthesis procedures, such as laser ablation.

The distinction between *local* and *environmental* disorder, applied to macroscopic bulk materials does not bear the same

^aDepartment of Materials Science, Saarland University, 66123 Saarbrücken, Germany.
E-mail: n.souza@mx.uni-saarland.de

^bINM – Leibniz Institute for New Materials & Department of Materials Science, Saarland University, 66123 Saarbrücken, Germany

† Electronic supplementary information (ESI) available: Beam diameter calculation, full laser irradiances and exposure times. See DOI: 10.1039/c5ra09316c

importance. Although impurities are a notorious issue limiting properties of most bulk materials, point lattice defects are, to a certain extent, of little importance for the overall performance.¹⁰ When leaving the world of 3-D materials, however, we see that 1-D structures are only as good as their weakest link, and defective CNTs experience abrupt decay in mechanical, optical, and electrical properties (with certain exceptions, *e.g.*, brightened photoluminescence through sp^3 defects¹⁴). Thus, we have seen over the last years an increased interest in not only tuning synthesis routes for purer and more crystalline CNTs, but also purifying and healing intrinsic defects, post-synthesis. To this end, a variety of mechanical, chemical, thermal, and radiation techniques exist.

Wide-spread mechanical treatments include centrifugation, mixing, microfiltration, and ultrasonication,^{10,15–17} and can effectively separate different species from the CNTs by capitalising differing densities, form factors and weak chemical bonding. These methods rely on liquid processing in suspensions. In contrast, chemical purification relies mainly on the low reactivity of CNTs when treated with acids or bases. Tube ends, whether open or closed, and the side walls of small tubes are chemically much more reactive due to edges, polygonal distortions, and curvature-induced strain, even in an ideal tube (although, metallic tubes seem to be more reactive than semi-conducting ones¹⁸). Yet, even defective tubes are less reactive compared to sample contaminants including other nanocarbons.¹⁰ This unique feature allows for effective removal of carbonaceous species and metal impurities; however, this comes at a price: tube caps and the outer walls of multiwall CNTs (MWCNT) or complete SWCNTs may also be oxidised, shortened, or even removed. This net material loss accompanies the formation of new defects and attached functional groups. Finally, thermal purification, perhaps the simplest, consists in heating a sample under a certain atmosphere.¹⁹ In air, oxidation is the predominant mechanism of purification, while protective atmospheres favour thermal decomposition and healing *via* increased defect mobility. In both cases, desorbed impurities can be removed effectively by a gas flow or further liquid-state treatments.

Some methods can more effectively than others eliminate impurities and/or defects and combinations of different methods can improve results. It is important to note that the aforementioned methods are usually rather time-consuming and possibly even damage the CNTs.¹⁰ Furthermore, laborious liquid processing may include surfactants, solvents, and other dispersing agents that need to be removed and is incompatible with certain applications such as direct CNT thread spinning. Thus, advanced alternative methods yielding high purity CNTs are still in high demand and under extensive investigation.

In contrast to the aforementioned methods, one facile treatment emerges as a fast, and contactless alternative, capable of bridging the stated drawbacks. It is well known that electromagnetic radiation can be used to modify the structure of CNTs, indeed the electron beam in a transmission electron microscope (TEM) can cause knock-on defects at an accelerating voltage of 80 kV.²⁰ In fact, electromagnetic radiation has been mostly used to damage, rather than fix, in order to study

defects, improve adhesion to a polymer matrix or improve sensitivity/selectivity in gas sensing.²¹ In this sense, CNTs have been blasted with the full spectrum of radiation from X-rays²² to microwaves,^{23,24} both of which produce defects, while the latter drives heating and intermixing to improve acid purification rates.

Until now, few studies have explored the spectrum in-between, from ultraviolet to infrared light. On the one hand, based on the limited literature, several noteworthy studies infer a promising ability to purify and heal defects in pristine (as-produced) or pretreated (annealed or oxidised) CNT samples with the help of different lasers. On the other hand, others report the lack of any positive effect,^{25–28} or selective removal of metallic or semiconducting tubes.^{29–31} However, in the literature, CNT purification and healing with laser has been limited in scope and data volume. Power, wavelength and atmosphere have been explored to a certain extent, yet radiation times and technical applications are missing. This has motivated us to revisit the method of laser irradiation to tune the CNT structure and the sample environment, as a method for healing and purification.

Illustrating the importance of choosing suitable processing parameters, one noteworthy study by Hurst *et al.* found no structural improvement when exposing SWCNTs to 30 s of pulsed 193 nm excitation in N_2 ; yet, repeated with 248 nm in ambient air drastically enhanced the results.³² In such studies, structural information is readily available by monitoring the D/G signal intensity ratio (I_D/I_G) by Raman spectroscopy.³³ The 2012 study by Judek *et al.* on MWCNTs employed a non-pulsed (constant wave, CW) 514 nm exposure yielding a moderate drop in the defect concentration after 120 s.³⁴ A notable 94% drop in I_D/I_G of randomly ordered SWCNTs was achieved by a CW 785 nm laser at 573 kW cm⁻² in air.³⁵ In general, the oxidising environment seems to be crucial, yielding the best results compared to inert atmospheres. Only two studies with protective atmospheres were able to put forth a marginal improvement. A detailed summary of laser healing and purification in the literature can be found in Table 2 (Section 3.4).

A central goal of our study is to explore in detail the use of laser radiation to heal and purify CNTs. To evaluate these characteristics, a Raman spectroscope was chosen, providing alternating *in situ* radiation and characterisation. We will concentrate on SWCNTs for probing interactions with light. They provide better metrics in Raman spectroscopy since they exhibit a radial breathing mode (RBM) and more readily exhibit changes than their multiwall counterparts. MWCNTs have more complex reactions due to several non-commensurate, multi-chiral walls with interlayer couplings and other phenomena.³²

Aside from the CNT synthesis itself (in our case: laser ablation), defects and impurities may stem from CNT manipulation and certain post-treatments. Breaking up CNT agglomerates into stable dispersions is paramount to many applications including composite processing, which relies heavily on a homogenous distribution of tubes throughout the matrix.³³ It was thus important for us to broaden the scope of our work beyond as-grown defects to include such processing-derived damage. We will thus apply 532 nm laser light to pristine and

damaged SWCNTs in ambient air with varying power and exposure times.

2. Experimental

2.1. CNT synthesis

SWCNT samples were synthesised by pulsed laser deposition (PLD). A carbonaceous feedstock pellet (target) was consolidated by cold-pressing a blend of ball-milled powders, namely, graphite and 1.2 at% metal catalysts (equal parts Ni and Co). The target was vaporised by a pulsed laser (solid state Nd:YAG 10 Hz 10 ns-pulse Newport-SpectraPhysics Quanta-Ray 290) inside a furnace at 1200 °C under 3 sccm Ar at 0.7 bar. The synthesis follows the experimental work of Guo *et al.*³⁴

After 30 min of deposition, the CNTs were collected downstream from the ablation plume on the fan-cooled quartz tube end (as opposed to a copper collector), outside of the hot zone, by peeling them off and stretching them over silica glass substrates (standard laboratory grade). These freestanding SWCNT thin films (*i.e.*, buckypaper) constitute the starting material for the experiments. All samples for pre/post-characterisation and laser treatment were extracted from the same batch. Note that the term pristine is used here to denote an original state or purity as opposed to completely pure.

2.2. Mechanically induced damage

Beyond as-grown defects, processing-derived defects were targeted to study the effect of the laser treatment. Common CNT processing includes dispersion to break up agglomerates which hinder certain properties. Composite processing (non templated) relies heavily on dispersion to achieve a homogenous dispersion of the tubes throughout the matrix.³³ A common dispersion procedure was thus applied to the starting material in order to introduce further defects, typical in CNT composites. A sample was dispersed in ethylene glycol, subjected to 2 min of laboratory-scale shear mixing at (5000 RPM), 10 min of ultrasound (room temperature bath; 35 kHz; 860 W), and 30 min of centrifugation (4500 RPM).

2.3. Material characterisation

Scanning electron microscopy (SEM) afforded an initial morphological characterisation using an FEI Helios NanoLab 6000 system. Thermogravimetry (TG) and differential scanning calorimetry (DSC) were carried out using a Netzsch-Gerätebau Jupiter 449 setup with 10 mg of pristine starting material, heated at 10 °C min⁻¹ up to 800 °C in air, yielding approximate proportions of existing species. Transmission electron microscopy was carried out on a TEM (JEOL 2100F) operated at 200 kV. Samples for transmission electron microscopy (TEM) were prepared by dispersing fibres in ethanol and drop casting them on a copper grid with a lacey carbon film (Gatan).

Raman spectra were collected with a Raman spectrometer (Renishaw inVia) with 532 nm (2.33 eV) CW excitation through a 50× objective with a numerical aperture of 0.75, producing a 2.91 μm spot (calculation in the ESI Fig. S1†) on the sample. The focus was carried out with respect to the laser spot sharpness, rather

than that of the sample, to ensure reproducible laser radiation. The power setting for all Raman measurements was set to 8.8 μW (0.13 kW cm⁻² = I_0). This was chosen below a threshold of 0.0176 mW (2.65 kW cm⁻² = I_{th} ; determined within this study, on the same basis), beyond which modification is observed in these SWCNTs. The analysis of the CNT state, pre- and post-laser-treatment, will be presented as characterised by their distinctive Raman vibrational modes RBM, D, G (G⁻ and G⁺), and G'. Because isolated peak intensities are of little meaning, this study will be based on qualitative and quantitative peak ratio comparisons, as opposed to integrated sub-peak areas. All Raman spectra were collected from 100 to 3500 cm⁻¹ and baseline-corrected with a straight line through the middle of the base noise over the complete range, with no observed fluorescence. Peaks were deconvoluted and fitted with Lorentzian functions.

2.4. Laser irradiation

Samples were irradiated in the same Raman system used for characterisation, with the same laser and the same conditions. A large array of attenuation levels were obtained by combining the pre-set attenuators of the spectrometer with a progressively metal-coated disc that was manually rotated to a certain level of transmittance. All powers were measured at the focal point with a power meter (Coherent LaserCheck; 10 nW resolution).

In our study, we investigated three facets of CNT structure modification as a result of applied laser radiation, namely, the influence of laser power, exposure time, and the difference between as-synthesised and mechanically damaged tubes. (1) First, the incident laser power (herein referred to as laser power or power, as opposed to the nominal laser power) was varied with fixed exposure time. (2) The ensuing optimal power was then fixed with varying exposure times. (3) Values for optimised laser power and exposure time derived from (1) and (2) were then used to study the healing of mechanically introduced damage to the CNT structure. Five sweeps were carried out for each varied parameter.

The laser power P was swept over 3 orders of magnitude from 8.8 μW to 8.8 mW producing an irradiance I of up to *ca.* 132 kW cm⁻² (see ESI Fig. S2a†) with a fixed exposure time of 130 s. Different interval step-sizes were adapted to the rate of signal change of the Raman spectra to track structural changes. Since one sweep was carried out on a single spot, each measurement presents the state of the tubes as a result of all preceding exposures. Although, as the results will show, accumulated and direct radiation produced identical results. In addition, the exposure time of single shots was varied between 0.1 and 200 s (Fig. S2b†) with intervals equally adapted to the rate of change of the Raman signal and a fixed power of 0.88 mW. Again, each measurement presents the state of the tubes as a result of all preceding exposures; thus, accumulated exposure times reach 680.8 s.

3. Results and discussion

3.1. As synthesised freestanding SWCNT mats

SWCNT mats, *ca.* 10 μm thick, with randomly aligned bundles were collected after synthesis. All samples showed an average

10 nm bundle diameter and a large amount of impurities according to SEM and TEM micrographs (Fig. 1a–d). TG clearly shows a three-stage mass loss corresponding to four distinct DSC peaks (Fig. 1e). Although several overlapping effects are responsible for mass loss, certain conclusions can be put forth. Due to the generally high surface area of SWCNT samples ($285 \text{ m}^2 \text{ g}^{-1}$ for $\varnothing 1.3 \text{ nm}$ SWCNTs, see ref. 35), the majority of the initial 24 wt% drop in mass can be associated with the loss of weakly adsorbed surface groups and their oxidation (foremost water). Between 387 and 396°C , we see another loss of 22 wt% which aligns with the effective removal of amorphous carbon as supported by the strong exothermic DSC peak, outweighing a possible weight gain from the oxidation of catalyst metal nanoparticles. With *ca.* 54% remaining mass, a third stage represents continuous oxidation of SWCNTs until *ca.* 624°C with a residual 5 wt% sample mass remaining. The latter represents the remaining non-volatile metal catalyst particles which remain unaffected up to 800°C . From these data, it can be inferred that the initial sample contained *ca.* 60 wt% SWCNTs of the total carbonaceous species.

The measured Raman spectrum (Fig. 2a) is characteristic for SWCNTs with well-defined D and G modes, overtones and combination modes, and, at low wavenumbers, radial breathing mode (RBM) vibrations. The emergence of rather broad Raman peaks with overlapping D and G modes confirms low crystallinity, and graphitic and disordered contaminants. The D- and G-band peaks found in graphite have a much higher intrinsic linewidth compared to the extremely narrow peaks of pure SWCNTs;³⁶ thus, the broadened peaks indicate the presence of non-CNT carbon nanoforms in the as-synthesised samples.

The RBM arises from radial vibrations of the carbon atoms, and their frequency can be linked to the tube diameter:³⁷

$$\omega_{\text{RBM}} = \frac{234}{d_t}$$

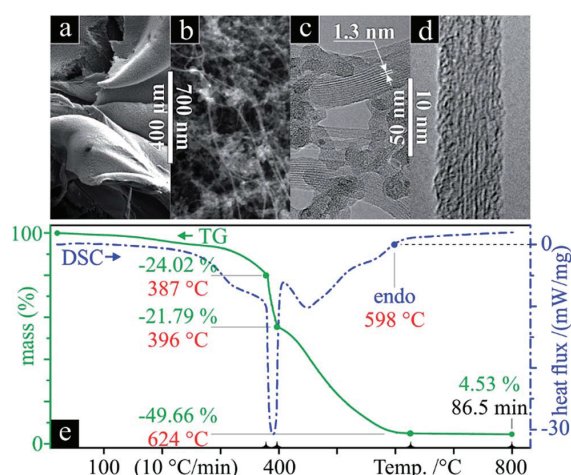


Fig. 1 SEM (a and b), TEM (c and d), TGA and DSC (e) of the pristine SWCNTs.

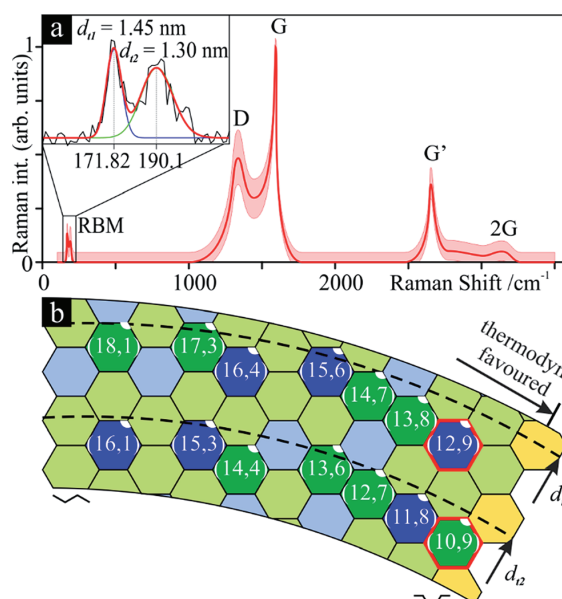


Fig. 2 Raman spectrum averaging 10 individual scans (a) and chirality map (b) of the starting material. Light green, blue and yellow indicate semiconducting, metallic and semi-metallic tubes. The darker cells with chiral vector are the possible tubes as per RBM frequencies. The thick, red outlined cells ((10,9) & (12,9)) are near-armchair and thermodynamically favoured.

According to this, the sample contains a narrow diameter (d_t) distribution with two distinct peaks indicating tube diameters of 1.45 nm (d_{t1}) and 1.30 nm (d_{t2}), the former slightly more intense. Considering near-armchair tubes are more thermodynamically favourable and predominantly produced,³⁸ it is possible that the former are semiconducting (10,9) tubes and the latter are metallic (12,9) (Fig. 2b). Yet, with a spectral resolution of *ca.* 1.3 cm^{-1} , these conclusions remain approximate.

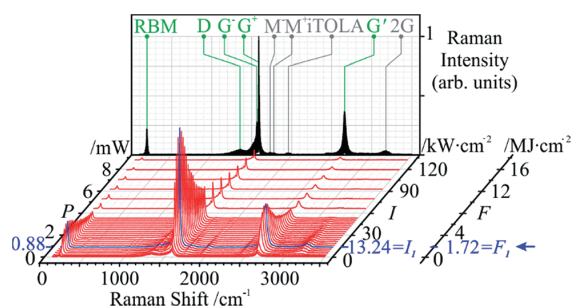


Fig. 3 Power sweep: Raman signal vs. power (P), power density (I) and fluence (F). A sharp non-proportional increase in the intensity of the graphitic order-induced RBM, G and G' modes is observed up to 0.88 mW (blue spectrum, marked by arrow), followed by a gradual signal intensity drop. Peaks are labelled (green & underlined, for those used in this study) on the rear plane containing the accumulated shadows of all spectra.

The initial Raman indicators for tube defects and purity are $I_D/I_G = 0.49$ and $I_{G'}/I_D = 0.72$, respectively.

Due to curvature effects in small-diameter tubes (e.g., SWCNTs), the G mode splits into two peaks: G^- and G^+ . In this case, the longitudinal (tube axis) vibrations of the latter are the main contribution to this mode, *versus* the circumferential vibrations, which become more visible with the laser treatment. This intensity disparity and the narrow shape of G^- indicates predominant semiconducting tubes,³⁶ G^+ will thus replace G in the defect ratio in this study.

The generalised I_D/I_G ratio is commonly used to indicate tube *quality*. The D mode is activated by a defect in the breathing modes of sp^2 -hybridised rings and its intensity is proportional to defect concentrations, but not to the actual amount of sp^2 carbon³⁹ (this only holds for an inter-defect distance above ~ 2 nm;⁴⁰ in our case, it remains between *ca.* 39 and 800 nm; calculated with I_D/I_G and the excitation wavelength: see Section 3.2). An sp^2 lattice disturbed by sp^3 -bonded carbons will thus contribute to the signal, although pure sp^3 -hybridised carbon shows no D mode.⁴¹ The disorder-induced nature of the double-resonance D mode *versus* the in-plane vibrations of the graphitic structure of the G mode attests to the defect state of the tubes.⁴² A high-quality sample will thus approach a ratio of zero.

The second harmonic of the D mode, G' , arises from a two-phonon, second-order Raman scattering process and is insensitive to tube defects. Instead of a defect, a second phonon backscatters an electron.⁴³ A high-quality sample produces spectra free of any signal contribution from defects with G' intensities comparable to that of G.³⁶ Due to this, $I_{G'}/I_D$ is often used as an indication of sample *purity* (i.e., absence of contaminants).⁴² This ratio removes conflicting chirality-dependent resonance issues and contaminant contributions that parasitize the D-mode intensity (as confirmed by TGA and SEM in ref. 42), confirming and expanding on I_D/I_G .⁴⁴

3.2. Influence of laser power

Taking the spot area, A , into account, the power density, or irradiance I , affords a comparison to previous studies and ranges between 0.04 and 44.9 kW cm^{-2} . However, we note that the fluence, F , is actually a more meaningful expression of the energy input that the sample is submitted to; in our experiments, F is in the range of 17.2 kJ cm^{-2} to 17.2 MJ cm^{-2} and defined from the laser power, P , and exposure time, t , as follows:

$$F = \frac{Pt}{A}$$

It should be noted that all Raman spectra were obtained at the non-modifying irradiance I_0 . The twenty-nine Raman spectra (Fig. 3) show a sharp increase in the order-induced modes (as opposed to disorder induced) RBM, G and G' up to 13.24 kW cm^{-2} (I_1) followed by a slower decline. The disorder-induced D mode increases slightly up to $\sim 2.65 \text{ kW cm}^{-2}$ (I_{th}) followed by a gradual decrease in signal strength.

The selected Raman modes (Fig. 4) more clearly display a strong non-proportional amplification, a maximum at I_1 , and a

gradual decay. Apart from sample chemistry, the Raman signal strength is sensitive to concentration, aggregation state (i.e., bundling),⁴⁵ excitation wavelength, and laser power. Since the two latter parameters were kept constant, the increase in Raman signal must be associated with another factor. Although laser radiation can cause bundling of tube ends in CNT forests, thus contributing to a signal increase,²⁶ our randomly ordered samples make this rather unlikely. The effect of laser absorption by amorphous carbon to explain the initial increase of all the SWCNT features can only be limited, due to the equally intensified G' mode. The signal decay above I_1 can be attributed to material loss.

Although peak ratios are unaffected by spectrum normalisation, Fig. 4 shows important signal changes that can only be seen when not normalising the datasets to a certain value. Note that only the smaller 1.30 nm tubes (d_{t2}) have been plotted as RBM_2 , since the signal of the larger 1.45 nm (d_{t1}) tubes (RBM_1) barely increases (see Fig. 8, left inset). RBM_2 increases so strongly that we can eventually even see its overtone (Fig. 8, right inset).

Peak ratios and their change as a function of irradiance (Fig. 5) provide us with a more pertinent look at the state of the tubes. The irradiance I_{th} (maximum of I_D at 2.65 kW cm^{-2}) was chosen as a threshold, below which no CNT modification is observed. It marks the onset of a sharp drop in $I_D/I_{G'}$, showing signs of saturation around 5.30 kW cm^{-2} (Fig. 5a) and assuming a rather constant value at I_1 . Here, $I_{G'}/I_D$ has risen to 12-fold its initial value (0.72). If indeed aromatic carbon rings and olefinic/conjugated carbon chains contribute to the G mode, these occur at lower wavenumbers than that of SWCNTs and, if detectable, would have altered the peak profile, its Lorentzian fit, and the resulting position. This was not observed, yet, their supposed contribution to G would rapidly decrease with the first curing steps, since these molecules are highly volatile under laser radiation⁴⁶ and they can be incorporated in further tube growth.⁴⁷ Again, to circumvent the inaccuracies that may accompany the $I_D/I_{G'}$ ratio, $I_{G'}/I_D$ complements the characterisation. These two parameters, common indicators of defect and purity states, experience a 92% and 1180% improvement (at I_1), respectively, with respect to the pristine material (at I_0). Following this point, the defect density is stable and the purity

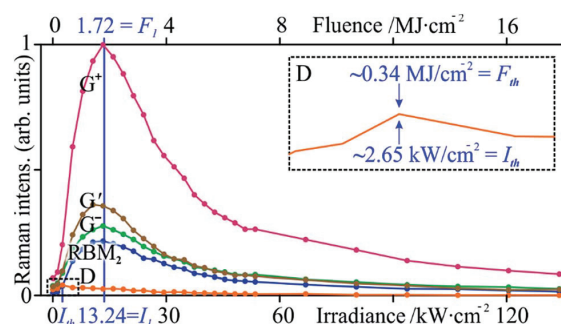


Fig. 4 Peak intensity variations of the studied Raman modes *versus* laser power. All modes peak at I_1 except for D, at $I_{th} = 0.9 \text{ kW cm}^{-2}$.

fluctuates with a gradual downwards tendency, possibly due to tube opening. The obtained drop in defect density is similar to that of Fabbro and Da Ros,⁴⁸ who utilised a CW 785 nm radiation at 573 kW m⁻² in air. Their *ca.* 40-fold irradiance can be partly explained by a lower absorbance at said energy (1.58 eV) for both SWCNTs⁴⁹ and amorphous carbon⁵⁰ although their sample has different and more varied tube diameters and chiralities, which further govern absorbance.

In a further analysis of tube crystallinity, the double resonance nature of the D band can be related to the mean inter-defect distance (L_a), derived from the *coherence length* in graphite,^{51,52} through a function of the inverse I_D/I_{G^+} ratio and the excitation wavelength λ , 532 nm in this case:

$$L_a = 2.4 \times 10^{-10} \lambda_{\text{laser}}^4 \left(\frac{I_D}{I_{G^+}} \right)^{-1}$$

Initially intended to describe the mean in-plane crystallite size in graphite,⁵³ the expression has since been extended to graphitic materials in general, including nanocarbons^{54,55} and CNTs.⁵⁶

Lower defect concentrations imply a statistically greater separation between defects; thus, as the fluence increases, L_a saturates around I_1 (Fig. 5b) with a maximum at 105 kW m⁻² and almost identical fluctuations as the purity (I_{G^+}/I_D). This makes sense, since G^- and G^+ have a similar behaviour and, mathematically, L_a is an amplification of an inverse I_D/I_{G^+} .

Another useful tool for the analysis of tube crystallinity is the full width at half maximum (FWHM or Γ) of a given Raman peak: a narrower vibrational band correlates with higher material crystallinity.⁵⁷ However, since aromatic or benzene clusters in amorphous carbon contribute to the signal of the D mode,⁴¹ its peak narrowing would only indicate a reduction in the variety of species resonating at this frequency. An order-induced peak is more appropriate and the G mode presents the strongest signal intensity, thus reducing error. The FWHM of a deconvoluted G^+ (Γ_{G^+}) shows a 70% drop and saturates around 7.9 kW cm⁻² (Fig. 5b), followed by a marginal 0.9 cm⁻¹

widening (below a local spectral resolution of 1.1 cm⁻¹). This trend aligns well with that of the defect density and the purity.

Fig. 5c presents two peak ratios from which further conclusions can be drawn. I_{G^-}/I_{G^+} represents the G-mode splitting gap, that is, the G^+ -normed intensity difference between the two peaks. G-mode splitting appears in SWCNTs and although G^+ is only sensitive to d_t , G^- depends on the tube being metallic/semiconducting³⁶ in frequency (ω) and intensity. Metallic SWCNTs produce similar intensities for both peaks while semiconducting tubes have a very weak G^- signal. In this case, I_{G^-} went from around double I_{G^-} to almost quadrupling it at I_1 . Since 532 nm radiation is known to selectively burn metallic tubes,^{29–31} the increased G^+-G^- gap aligns well with metallic tubes being removed, producing a G band more closely resembling that of semiconducting tubes.³⁶ Therefore, it is very likely that after the preferential removal of metallic tubes, predominantly semiconducting SWCNTs (the speculated (10,9) tubes with d_{t2} from Fig. 2) remain at I_1 . This is supported by the 20-fold growth of the I_{RBM2} vs. a mere doubled I_{RBM2} (Fig. 8). Although the d_{t2} tubes are smaller, and thus more reactive and prone to oxidation, according to Huang *et al.*, this removal of the larger metallic tubes is related to chirality rather than size.²⁹ This, together with the faster growth of I_{RBM2} vs. I_{G^+} (Fig. 5c), points to competing mechanisms of defect removal, sample purification and loss of metallic tubes.

The strong overall increase in Raman signal strength together with the mentioned Raman indicators strongly point to an increasing level of graphitisation, defect healing, and sample purification. 130 s of 13.24 kW cm⁻² (*i.e.*, 1.72 MJ cm⁻²) is roughly equivalent to 10.7×10^{25} eV cm⁻². At the single nanotube level, the energy input is equal to 10.7×10^{11} eV nm⁻² and, thus, well above the binding and migration energies for interstitials, vacancies, and other defects.¹⁰ A heat conduction model puts the surface temperature of a MWCNT film under *ca.* 80 mJ cm⁻² of green laser light at around 800 °C.⁵⁸ Above this temperature, Gorbunov and Jost argue that further growth of SWCNTs can be induced⁵⁹ and we must consider that there is a

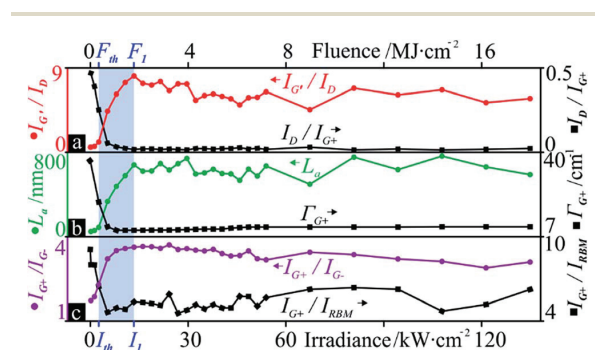


Fig. 5 From top to bottom, all versus irradiance and fluence: Raman purity (normalized I_{G^-}/I_D) and quality (I_D/I_{G^+}) indicators (a); inter-defect distance (L_a) and full width at half maximum of G^+ (Γ_{G^+}) (b); G^+ vs. G^- growth, *i.e.* G mode splitting gap (I_{G^-}/I_{G^+}), and G^+ vs. RBM growth, *i.e.* gap between the two main order-induced peaks (I_{G^+}/I_{RBM2}) (c).

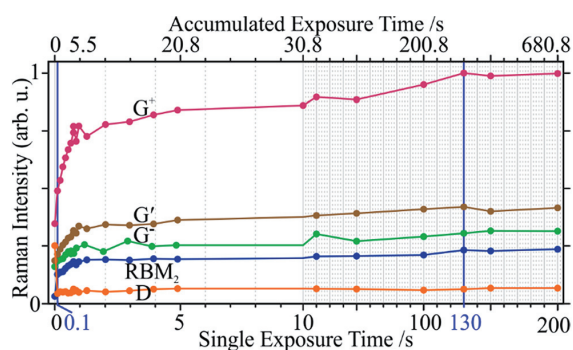


Fig. 6 Peak intensity variations of the studied Raman modes vs. single and accumulated (nonlinear) exposure times. The D mode saturates abruptly after a 0.1 s shot, while the other modes need 130 s to do so. The time scale proportionality is stretched in the first ten seconds to show more detail.

huge abundance of carbon in the sample. High-temperature synthesis of SWCNTs (*e.g.*, laser ablation) produces abundant adsorbed, reactive carbons. The ground state of carbon systems, sp^2 hybridisation, remains more stable than sp^3 at high temperatures,¹⁰ which promotes the growth of graphitic carbon even in amorphous carbon.⁶⁰ We thus have the temperature and the carbon necessary for graphitization and tube growth. Although carbon nanotubes can coalesce,⁶¹ the absence of peak shifts in the spectra indicate no such occurrence. For the same reason, the creation of new polygonal defects can be excluded (except for Dienes or Stone–Wales defects), since these cause changes in helicity and diameter, neither of which are observed in our experiments.

The optimal irradiance seems to be I_1 , 13.24 kW cm^{-2} , which when used to treat 20 different pristine sample locations with a direct exposure (no preceding step-wise increments) produces very reproducible results (Fig. 8). Interestingly, the I_1 spectrum from Fig. 4 (tubes exposed with all intermediate irradiances up to and including I_1) fits perfectly within this spectrum. This means that, at this exposure time (130 s), the previous energy input has no effect and tube state is solely a function of the last shot. Furthermore, repeated exposures with I_1 bear no observable (Raman) effect on the tubes with equally fitting spectra.

If accumulated exposures, measured in energy or fluence, have no influence on the tube state, then the exposure time is either irrelevant or too long to observe any singularities. A study of the exposure time, well below 130 s, was thus carried out.

3.3. Influence of exposure time

At the optimal fixed irradiance of 13.24 kW cm^{-2} (I_1), all Raman modes experienced signal amplification and eventual saturation with varying exposure times from 0.1 s to 200 s. All peak intensities saturated at 130 s (single shot if not specified otherwise), except for D, which instantly dropped to a minimum at 0.1 s (Fig. 6). Over 50% of the total changes occur within the first second of accumulated exposure.

The purity does not seem to improve for an exposure longer than 1 s (Fig. 7). Carried by the stark signal decrease of the D mode, the defect density saturates at 0.1 s. Since this was the shortest (possible) exposure time, a more accurate portrayal of the sample evolution within this interval is not available. However, as with the power sweep, the defects are quickest to react to the radiation in terms of power and time. The removal of impurities requires longer times, due to the elimination of metal catalysts and metallic tubes which can leave behind open tubes. Again, a direct shot with a certain exposure time produced identical results to that of accumulated exposures of equal or lower times. This implies a build-up of slow thermal effects, necessary to remove impurities and correct defects. SWCNTs have a thermal conductivity at least 6- and 25-times that of graphite and amorphous carbon, respectively, and 10-times the thermal diffusivity.⁶² Hence, the temperature will rise much slower in the tubes due to more efficient energy transfer.

Although the purity and the defect density both saturate after *ca.* 1 s of exposure, peak intensities continue to increase until

130 s, possibly due to defect correction competing with metallic tube removal. The 130 s mark (t_3) was thus taken as an optimal exposure time and, together with I_1 , were found to best heal defects and remove impurities. Direct laser curing with I_1 and t_3 was thus carried out on 20 different sample locations and averaged (Fig. 8). The low standard deviation attests to the reproducibility and even accommodates the corresponding spectra with previous incremental powers and times.

In order to explore the degree of sample modification resulting from these two parameters, in and around a produced laser spot, we performed two $20 \mu\text{m}$ ($1 \mu\text{m}$ step) Raman line-scans, intersecting at the centre of said spot. The remaining parameters were identical to all other Raman measurements. I_D/I_{G^+} was calculated for each point and plotted, both scans showing Gaussian distributions in concordance with a Gaussian beam profile. Considering rotational symmetry of the beam, a 3-D surface was extrapolated from the 2-D Gauss curves resulting in a $20 \times 20 \mu\text{m}^2$ grid, covering the laser spot and its surroundings (Fig. 9). The surface is slightly elliptical, due to the beam shape, which loses its symmetry in the beam path

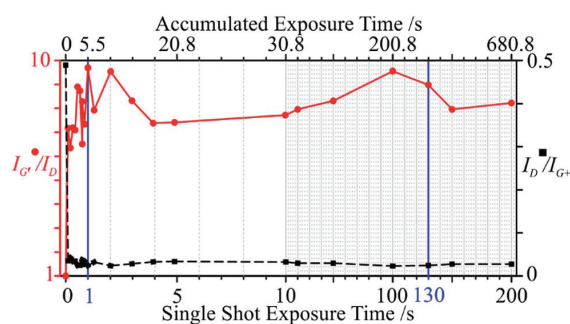


Fig. 7 Raman defect and purity ratios vs. exposure time. The time scale proportionality of the single shot exposure is stretched in the first ten seconds to show more detail. The accumulated time axis is nonlinear.

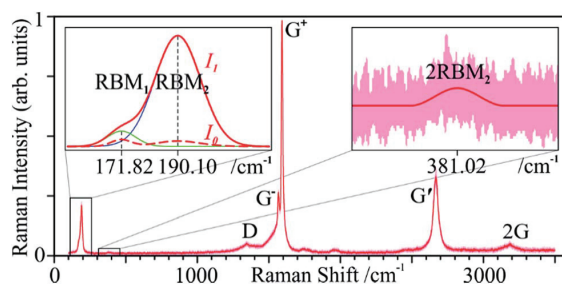


Fig. 8 Raman spectrum after optimal irradiance $I_1 = 13.24 \text{ kW cm}^{-2}$. The 20-location average (red) has a very low standard deviation (pink). An exposure of other sample regions with this irradiance including previous step-wise exposures produces spectra that fit within this standard deviation. Left inset: the RBM bands vs. those before the laser treatment (I_0 , dashed). Right inset: RBM_2 is so intense that its overtone 2RBM_2 is visible. $R^2 > 0.99$.

upon expansion and several reflections within the spectrometer.

This plot shows very local modification to the tubes, with the best results in the centre of the spot. However, a beam diameter of *ca.* 3 μm results in a modification reaching $\sim 11 \mu\text{m}$ (full width at tenth maximum). This difference and the change of the Raman modes over time underline Hurst's findings⁶³ in which the purification and annealing mechanisms are not limited to photochemical processes (governed by irradiance), but include photothermal effects. In agreement, we find that the CNTs are modified well beyond the beam diameter and the modification evolves over 130 s.

Each Raman spectrum was acquired directly following every laser curing step. Due to this, it is safe to assume that the sample temperature increase produced during curing had dissipated back to room temperature upon Raman excitation. This is confirmed by the absence of peak shifts in our spectra. Furthermore, a sample temperature assessment from Stokes/anti-Stokes considerations would provide that of the Raman excitation, not of the curing. In order to obtain the latter, spectra would have to be acquired during curing, excluding the possibility of varying the exposure time. Nevertheless, this was attempted and produced almost exclusively saturated spectra (even at RBM and G' modes), hindering any data evaluation.

3.4. Laser healing and purification of mechanically damaged SWCNTs

In order to improve load transfer and electrical and thermal conduction, carbon nanotubes need to be dispersed before they can be used as fillers in composites. Agglomerates are generally broken up by a combination of sheer mixing, ultrasound,

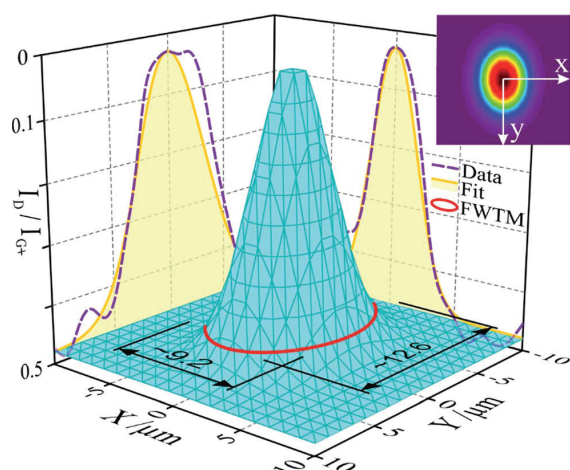


Fig. 9 I_D/I_{G^+} over a single, irradiated spot. The asymmetric (slightly elliptic due to beam shape) 3-D Gaussian surface results from the combined parameters of two 2-D Gausses ($R^2 > 0.98$) fitted over b-splined experimental data from intersecting Raman line maps. Note: the vertical axis is inverted to better view the 3-D surface. An average diameter of 10.9 μm (full width at tenth maximum; red ellipse) greatly exceeds the original 2.91 μm beam diameter.

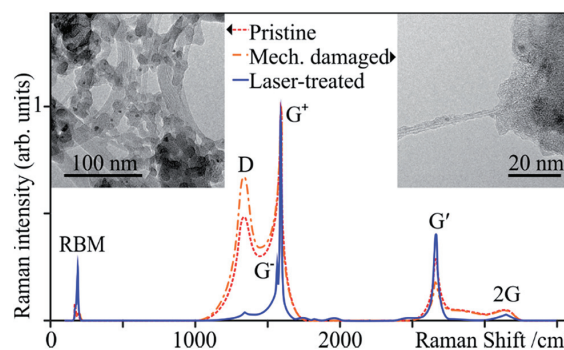


Fig. 10 Raman spectra of the pristine, mechanically damaged and laser-treated SWCNTs. The insets show TEM micrographs of the pristine (left) and the mechanically damaged (right) samples.

centrifugation, and sometimes aided by functionalization. As a result, in addition to the mechanical energy, collapsing cavitation bubbles produce severe heating and pressure.⁶⁴ All of these techniques may thus produce defects and impurities in CNTs to various degrees.^{64–67} In the case of polymer matrices, defective tubes actually improve matrix/reinforcement cohesion, still enhancing the properties of the matrix. In metal matrices, the damage is critical. In either case, damage and impurities can produce excessive degradation and physical property decay. In our experiments, we subjected pristine tubes to short shear mixing and ultrasonication times.

These samples present small tube bundles well below the initial 10 nm, indicating successful deagglomeration, and, as expected, damaged tubes and abundant non-CNT material (Fig. 10 “Mechanically damaged” spectrum and inset). The damaged tubes show a drastic drop in purity, $I_{G'}/I_D$, as a result of CNT exfoliation and the accumulation of graphitic and carbonaceous material from the mechanical damage. These damaged tubes were then laser-treated with the previously optimised parameters (I_1 and t_3) and characterised by Raman spectroscopy (Fig. 10 “Laser treated” spectrum and Table 1). After laser treatment, the defect density $I_D/I_{G'}$ drops from 0.67 to 0.04 (94%), nearly the same final value as that observed after laser annealing the pristine SWCNTs, yet a proportionately greater improvement (compared to 92%). The purity rises almost 17-fold. The recuperation is almost full, with final values similar to those of the laser-treated pristine tubes.

Table 2 puts the results presented in this study into context, with a summary of experimental conditions from the literature in which laser radiation improved the sample quality.

Table 1 Raman defect, purity and crystallinity indicators of a pristine, damaged and laser-treated SWCNT sample

	Pristine	Damaged	Treated
$I_D/I_{G'}$	0.49 ± 0.07	0.67 ± 0.03	0.04 ± 0.01
$I_{G'}/I_D$	0.72 ± 0.09	0.47 ± 0.04	8.56 ± 0.01
$\Gamma_{G'}$	35.89 ± 0.10	41.21 ± 0.90	12.01 ± 0.11

Table 2 Summary of laser irradiation of CNTs in literature with sample improvement (quantified or otherwise, as given), ordered by ascending wave length (λ). $\Delta(I_G/I_D)$ and $\Delta FWHM$ (of a given peak) are variations normed to the initial value and integer-rounded. Improvement denotes a reduction in either indicator (i.e. negative percentage). Note that in order to include them in this table, many values were calculated graphically (when not given otherwise) or inverted (some authors report I_G/I_D) and are therefore approximate references of what was published. Dashed cells concern unavailable data. The present study (in bold) is included for comparison^a

Sample	VA/RO	Atm.	CW/PW	λ (nm)	I (kW cm ⁻²)	t (s)	F (J cm ⁻²)	$\Delta(I_D/I_G)$ (%)	$\Delta FWHM$ (%)	Ref.
SWCNT	RO	N ₂	PW	193	0.65×10^{-3}	30	—	0	D: -10	63
SWCNT	RO	Air	PW	248	0.45×10^{-3}	30	—	-45	D: -24	63
CNT ^b	RO	Air	PW	248	—	60×10^{-9}	0.05	"Higher emission current"		68
DWCNT	RO	Ar	PW	355	0.016	13.3	—	-9	—	61
SWCNT	RO	Air	CW	418	1.2×10^{-7}	—	—	-88	—	69
MWCNT	RO	Air	CW	514	100	120×10^{-9}	—	-27	G: 0; D: -15	70
SWCNT	RO	Air	CW	514.5	25	—	—	-77	—	71
MWCNT	RO	Air	PW	532	—	6×10^{-9}	1	-17	—	72
MWCNT	RO	Air	PW	532	—	5×10^{-9}	285	-69	—	58
MWCNT	RO	Air	PW	532	—	5×10^{-9}	0.075	-21	—	27
SWCNT	RO	Air	CW	532	13.24	130	17.2×10^5	-94	G⁺: -71	This study
SWCNT	RO	Air	CW	632.8	1.0×10^{-7}	—	—	-64	—	69
MWCNT	VA	Air	CW	663	91.72	90	—	-86	—	73
SWCNT	RO	Air	CW	785	573	—	—	-94	—	48
MWCNT	RO	Air	PW	1064	—	6×10^{-9}	0.46	-70	—	58
MWCNT	VA	CO ₂	—	1064	0.019	—	—	"Purification" (SEM)		74

^a Key – vertically aligned (VA), Aka forest/randomly ordered (RO) sample; treatment atmosphere (atm.); constant wave (CW)/pulsed wave (PW) laser; laser irradiance (I); exposure time (t); laser fluence (F). ^b The type of nanotube was not specified.

4. Conclusions

The behaviour of SWCNTs post radiation with 532 nm laser light in air has been characterised, as probed by Raman spectroscopy. Peak intensity changes, ratios, and widths have been plotted vs. a wide range of power densities and exposure times. An optimal fluence of 1.72 MJ cm^{-2} was determined with 0.88 mW on a $2.91 \text{ }\mu\text{m}$ spot (13.24 kW cm^{-2}) for 130 s. Although 1 s (13.24 kJ cm^{-2}) produces similar results in terms of defects and purity, further peak intensification reveals ongoing processes up to ca. 130 s. There is evidence of thermal annealing of defects and removal of non-CNT carbonaceous species and metallic tubes. The optimised laser parameters were applied to tubes with induced mechanical damage resulting in a full recovery, compared to treated pristine tubes. The spatial characterisation of a laser-treated spot revealed a slightly elliptical Gaussian distribution of the tube modification over a surface twelve times that of the laser spot.

Exposure times are often neglected in CNT irradiation studies, excluding any measure of energy input. We show that even at high power densities, the time scale of tube modification reaches 130 s, with over 50% in the first second. It should be noted that the optimal fluence for annealing and purification corresponded to a mere 5% power setting in the Raman spectrometer and a similar exposure time to that of a single-accumulation $100\text{--}3500 \text{ cm}^{-1}$ scan. That is to say, CNT Raman data should be collected with previous knowledge of modification thresholds, as advised by Fabbro and Da Ros.⁴⁸

The added value of this study lies in three aspects: (1) the wide-ranging and thorough variation of the power density; (2) idem for the exposure time, not considered elsewhere; and (3) the application to a real problem in the CNT community,

namely, recovery of composite processing-based damage. As shown by our study, laser irradiation is an interesting and promising technique for CNT purification and defect removal, especially for surface or discrete tube treatments. Fine-tuned localised heating resulting in precision healing and purification, together with the removal of metallic or semiconducting tubes, could produce preferred electronic conduction paths in CNT films and improve existing treatments for CNT-based field effect transistors and sensors.

Acknowledgements

The authors acknowledge the EFRE Funds of the European Commission for support of activities within the AME-Lab project. This work was supported by the SUMA2 Network Project, 7th Framework Program of the European Commission (IRSES Project No. 318903), and the CREATE-Network Project, Horizon 2020 Program of the European Commission (RISE Project No. 644013). Thanks to Dr Daniel Weingarth and Dipl.-Ing. Robert Drumm (INM) for TG and DSC analyses and helpful discussions. Dr Sebastián Suárez, M.Sc. Federico Lasserre (Saarland University) and Prof. Dr Esteban Ramos Moore (Pontifical Catholic University of Chile) are kindly acknowledged for corrections and discussions. VP and MZ thank Prof. Eduard Arzt (INM) for his continuing support.

Notes and references

- 1 L. V. Radushkevich and V. M. Lukyanovich, O strukture ugleroda obrazujucesja pri termiceskom razlozenii okisi ugleroda na zeleznom kontakte, *Zurn. Fisic. Chim.*, 1952, **26**, 88–95.

- 2 S. Iijima, *Nature*, 1991, **354**, 56–58.
- 3 N. Hamada, S. Sawada and A. Oshiyama, *Phys. Rev. Lett.*, 1992, **68**, 1579–1581.
- 4 J. Mintmire, B. Dunlap and C. White, *Phys. Rev. Lett.*, 1992, **68**, 631–634.
- 5 R. Saito, M. Fujita, G. Dresselhaus and M. Dresselhaus, *Phys. Rev. B: Condens. Matter Mater. Phys.*, 1992, **46**, 1804–1811.
- 6 J. A. Robinson, E. S. Snow, Ş. C. Bădescu, T. L. Reinecke and F. K. Perkins, *Nano Lett.*, 2006, **6**, 1747–1751.
- 7 M. Wong, M. Paramsothy, X. J. Xu, Y. Ren, S. Li and K. Liao, *Polymer*, 2003, **44**, 7757–7764.
- 8 M. M. Shulaker, G. Hills, N. Patil, H. Wei, H.-Y. Chen, H.-S. P. Wong and S. Mitra, *Nature*, 2013, **501**, 526–530.
- 9 J. Stein, B. Lenczowski, E. Anglaret and N. Fréty, *Carbon*, 2014, **77**, 44–52.
- 10 P. G. Collins, in *Oxford Handbook of Nanoscience and Technology: vol. 2: Materials: Structures, Properties and Characterization Techniques*, ed. A. V. Narlikar and Y. Y. Fu, 2010, ch. 2.
- 11 J. Liu, A. Rinzler, H. Dai, J. Hafner, R. Bradley, P. Boul, A. Lu, T. Iverson, K. Shelimov, C. Huffman, F. Rodriguez-Macias, Y. Shon, T. Lee, D. Colbert and R. Smalley, *Science*, 1998, **280**, 1253–1256.
- 12 A. V. Krashenninnikov, P. O. Lehtinen, A. S. Foster and R. M. Nieminen, *Chem. Phys. Lett.*, 2006, **418**, 132–136.
- 13 M. Monthieux and J. C. Charlier, *Carbon*, 2014, **75**, 1–4.
- 14 Y. Piao, B. Meany, L. R. Powell, N. Valley, H. Kwon, G. C. Schatz and Y. Wang, *Nat. Chem.*, 2013, **5**, 840–845.
- 15 H. Jia, Y. Lian, M. O. Ishitsuka, T. Nakahodo, Y. Maeda, T. Tsuchiya, T. Wakahara and T. Akasaka, *Sci. Technol. Adv. Mater.*, 2005, **6**, 571–581.
- 16 S. Bandow, A. Rao and K. Williams, *J. Phys. Chem. B*, 1997, **5647**, 8839–8842.
- 17 K. B. Shelimov, R. O. Esenaliev, A. G. Rinzler, C. B. Huffman and R. E. Smalley, *Chem. Phys. Lett.*, 1998, **282**, 429–434.
- 18 E. Joselevich, *ChemPhysChem*, 2004, **5**, 619–624.
- 19 A. Suri and K. S. Coleman, *Carbon*, 2011, **49**, 3031–3038.
- 20 J. H. Warner, F. Schäffel, G. Zhong, M. H. Rummeli, B. Büchner, J. Robertson and G. A. D. Briggs, *ACS Nano*, 2009, **3**, 1557–1563.
- 21 I. V. Anoshkin, A. G. Nasibulin, P. R. Mudimela, M. He, V. Ermolov and E. I. Kauppinen, *Nano Res.*, 2012, **6**, 77–86.
- 22 T. Murakami, K. Asai, Y. Yamamoto, K. Kisoda and C. Itoh, *Eur. Phys. J. B*, 2013, **86**, 187.
- 23 H. Sun, J. Wei, J. Sun, C. Ning, J. Zhu, Y. Jia, S. Yang, H. Zhu, K. Wang, D. Wu, Y. Zhao, R. Vajtai and P. M. Ajayan, *RSC Adv.*, 2014, **4**, 15502.
- 24 K. MacKenzie, O. Dunens and A. T. Harris, *Sep. Purif. Technol.*, 2009, **66**, 209–222.
- 25 T. Nakamiya, T. Ueda, T. Ikegami, K. Ebihara and R. Tsuda, *Curr. Appl. Phys.*, 2008, **8**, 400–403.
- 26 K. Ramadurai, C. L. Cromer, A. C. Dillon, R. L. Mahajan and J. H. Lehman, *J. Appl. Phys.*, 2009, **105**, 093106.
- 27 T. Nakamiya, F. Mitsugi, K. Semba, R. Kozai, T. Ikegami, Y. Iwasaki, Y. Sonoda and R. Tsuda, *Thin Solid Films*, 2010, **518**, 6604–6608.
- 28 J. R. Mialichi, M. J. S. P. Brasil, F. Iikawa, C. Verissimo and S. A. Moshkalev, *J. Appl. Phys.*, 2013, **114**, 024904.
- 29 H. Huang, R. Maruyama, K. Noda, H. Kajiura and K. Kadono, *J. Phys. Chem. B*, 2006, **110**, 7316–7320.
- 30 M. Mahjouri-Samani, Y. S. Zhou, W. Xiong, Y. Gao, M. Mitchell and Y. F. Lu, *Nanotechnology*, 2009, **20**, 495202.
- 31 A. Roch, T. Roch, E. R. Talens, B. Kaiser, A. Lasagni, E. Beyer, O. Jost, G. Cuniberti and A. Leson, *Diamond Relat. Mater.*, 2014, **45**, 70–75.
- 32 C. Thomsen and S. Reich, *Light Scattering in Solids IX*, 2007, vol. 232, pp. 115–232.
- 33 S. Suarez, F. Lasserre and F. Mücklich, *Mater. Sci. Eng., A*, 2013, **587**, 381–386.
- 34 T. Guo, P. Nikolaev, A. G. Rinzler, D. Tomanek, D. T. Colbert and R. E. Smalley, *J. Phys. Chem.*, 1995, **99**, 10694–10697.
- 35 Y. Ye, C. C. Ahn, C. Witham, B. Fultz, J. Liu, A. G. Rinzler, D. Colbert, K. A. Smith and R. E. Smalley, *Appl. Phys. Lett.*, 1999, **74**, 2307.
- 36 M. S. Dresselhaus, G. Dresselhaus, R. Saito and A. Jorio, *Phys. Rep.*, 2005, **409**, 47–99.
- 37 C. Fantini, A. Jorio, M. Souza, M. Strano, M. Dresselhaus and M. Pimenta, *Phys. Rev. Lett.*, 2004, **93**, 147406.
- 38 V. Artyukhov, E. Penev and B. Yakobson, arXiv, 2014, **5**, 4892.
- 39 C. Casiraghi, A. Hartschuh, H. Qian, S. Piscanec, C. Georgi, A. Fasoli, K. S. Novoselov, D. M. Basko and A. C. Ferrari, *Nano Lett.*, 2009, **9**, 1433–1441.
- 40 A. C. Ferrari, *Solid State Commun.*, 2007, **143**, 47–57.
- 41 J. Schwan, S. Ulrich, V. Batori, H. Ehrhardt and S. R. P. Silva, *J. Appl. Phys.*, 1996, **80**, 440.
- 42 R. A. DiLeo, B. J. Landi and R. P. Raffaele, *J. Appl. Phys.*, 2007, **101**, 064307.
- 43 S. Reich and C. Thomsen, *Philos. Trans. R. Soc., A*, 2004, **362**, 2271–2288.
- 44 R. Saito, A. Grüneis, G. G. Samsonidze, V. W. Brar, G. Dresselhaus, M. S. Dresselhaus, A. Jorio, L. G. Cançado, C. Fantini, M. A. Pimenta and A. G. Souza Filho, *New J. Phys.*, 2003, **5**, 157.
- 45 A. I. López-Lorente, B. M. Simonet and M. Valcárcel, *Analyst*, 2014, **139**, 290–298.
- 46 U. Brand, H. Hippler, L. Lindemann and J. Troe, *J. Phys.*, 1990, **94**, 6305–6316.
- 47 L. Pang, L. Prochazka and R. Quezada, *Fuel Energy Abstr.*, 1995, **36**, 189.
- 48 C. Fabbro and T. Da Ros, *Carbon*, 2014, **76**, 96–104.
- 49 H. Kataura, Y. Kumazawa, Y. Maniwa, I. Umez, S. Suzuki, Y. Ohtsuka and Y. Achiba, *Synth. Met.*, 1999, **103**, 2555–2558.
- 50 N. D. Baydoğan, *Mater. Sci. Eng., B*, 2004, **107**, 70–77.
- 51 F. Tuinstra and L. Koenig, *J. Chem. Phys.*, 1970, **53**, 1126.
- 52 A. C. Ferrari and J. Robertson, *Phys. Rev. B: Condens. Matter Mater. Phys.*, 2000, **61**, 14095–14107.
- 53 L. G. Cançado, K. Takai, T. Enoki, M. Endo, Y. A. Kim, H. Mizusaki, A. Jorio, L. N. Coelho, R. Magalhães-Paniago and M. A. Pimenta, *Appl. Phys. Lett.*, 2006, **88**, 1–4.
- 54 L. G. Cançado, A. Jorio, E. H. M. Ferreira, F. Stavale, C. A. Achete, R. B. Capaz, M. V. O. Moutinho, A. Lombardo, T. S. Kulmala and A. C. Ferrari, *Nano Lett.*, 2011, **11**, 3190–3196.

Paper

RSC Advances

- 55 M. A. Pimenta, G. Dresselhaus, M. S. Dresselhaus, L. G. Cançado, A. Jorio and R. Saito, *Phys. Chem. Chem. Phys.*, 2007, **9**, 1276–1291.
- 56 S. Suarez, F. Lasserre, O. Prat and F. Mücklich, *Phys. Status Solidi A*, 2014, **211**, 1555–1561.
- 57 L. Ian, *Handbook of Raman Spectroscopy. From the Research Laboratory to the Process Line*, CRC Press, New York, Basel, 2001, vol. 28.
- 58 T. Nakamiya, T. Ueda, T. Ikegami, F. Mitsugi, K. Ebihara, Y. Sonoda, Y. Iwasaki and R. Tsuda, *Thin Solid Films*, 2009, **517**, 3854–3858.
- 59 R. Eason, *Pulsed Laser Deposition of Thin Films*, John Wiley & Sons, Inc., Hoboken, NJ, USA, 2006.
- 60 H.-J. Scheibe, D. Drescher and P. Alers, *Fresenius. J. Anal. Chem.*, 1995, **353**, 695–697.
- 61 Y. Zhang, T. Gong, J. Wei, W. Liu, K. Wang and D. Wu, *J. Phys. Chem. C*, 2007, **111**, 2901–2905.
- 62 M. Akoshima, K. Hata, D. N. Futaba, K. Mizuno, T. Baba and M. Yumura, *Jpn. J. Appl. Phys.*, 2009, **48**, 05EC07.
- 63 K. Hurst and A. Dillon, *J. Phys. Chem. C*, 2008, **112**, 16296–16300.
- 64 H. J. Park, M. Park, J. Y. Chang and H. Lee, *Nanotechnology*, 2008, **19**, 335702.
- 65 Y. Wang, J. Wu and F. Wei, *Carbon*, 2003, **41**, 2939–2948.
- 66 P. Garg, J. L. Alvarado, C. Marsh, T. A. Carlson, D. A. Kessler and K. Annamalai, *Int. J. Heat Mass Transfer*, 2009, **52**, 5090–5101.
- 67 S. Song, H. Yang, R. Rao, H. Liu and A. Zhang, *Catal. Commun.*, 2010, **11**, 783–787.
- 68 J. Yotani, S. Uemura, T. Nagasako, H. Kurachi, H. Yamada, T. Ezaki, T. Maesoba, T. Nakao, M. Ito, T. Ishida and Y. Saito, *Jpn. J. Appl. Phys.*, 2004, **43**, L1459–L1462.
- 69 P. Corio and P. Santos, *Chem. Phys. Lett.*, 2002, **360**, 557–564.
- 70 J. Judek, C. Jastrzebski, A. Malolepszy, M. Mazurkiewicz, L. Stobinski and M. Zdrojek, *Phys. Status Solidi*, 2012, **209**, 313–316.
- 71 L. Zhang, H. Li, K.-T. Yue, S.-L. Zhang, X. Wu, J. Zi, Z. Shi and Z. Gu, *Phys. Rev. B: Condens. Matter Mater. Phys.*, 2002, **65**, 073401.
- 72 T. Nakamiya, T. Ueda, T. Ikegami, F. Mitsugi, K. Ebihara and R. Tsuda, *Diamond Relat. Mater.*, 2008, **17**, 1458–1461.
- 73 Z. H. Lim, A. Lee, K. Y. Y. Lim, Y. Zhu and C.-H. Sow, *J. Appl. Phys.*, 2010, **107**, 064319.
- 74 X. Bai, D. Li, D. Du, H. Zhang, L. Chen and J. Liang, *Carbon*, 2004, **42**, 2125–2127.

Supporting Information

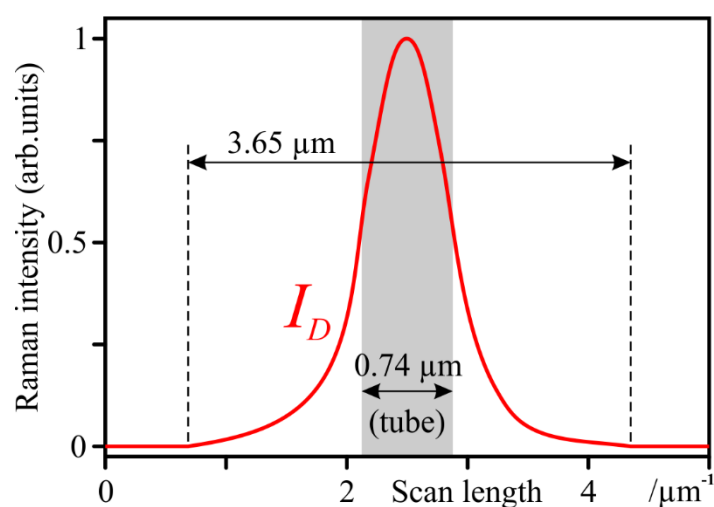


Figure S1 - Beam spot diameter determination: A Raman scan of an amorphous carbon fiber from ¹ with 0.175 mW. The known tube diameter (0.74 μm) was subtracted from the length of the monitored increment and decay in I_G . The resulting beam spot diameter is 2.91 μm .

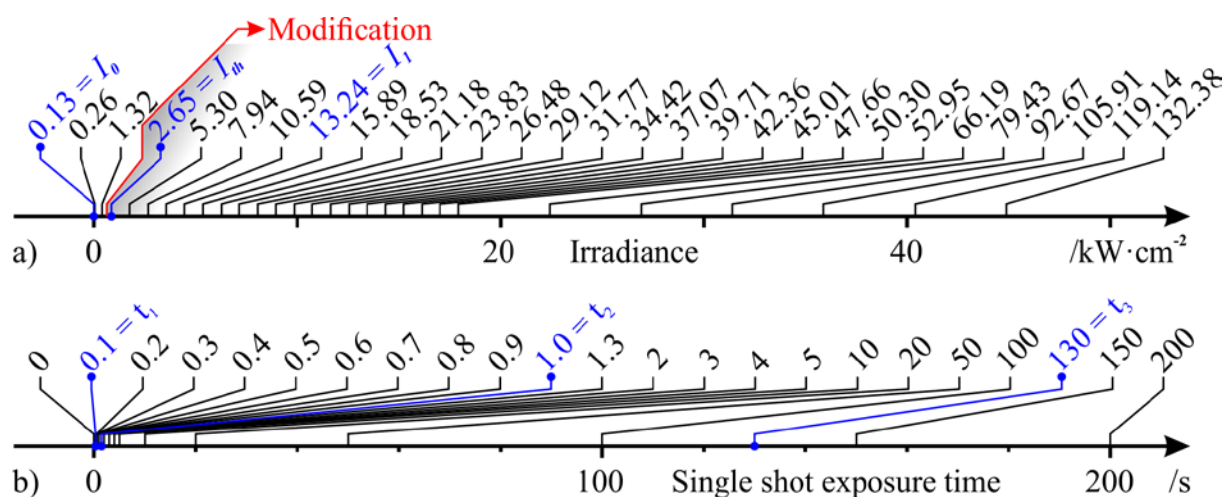


Figure S2 - Laser irradiance (a) and exposure time sweeps (b) – Different intervals adapt to the rate of change of the Raman signal. Values I_0 , I_{th} , I_1 and t_{1-3} are reference values for observed singularities.

- 1 M. Golshadi, J. Maita, D. Lanza, M. Zeiger and M. G. Schrlau, *Carbon N. Y.*, 2014, **80**, 28–39.

4.2. Scaling up single-wall carbon nanotube laser annealing: effect on electrical resistance and hydrogen adsorption

Nicolas Souza, Martín Roble, Donovan E. Diaz-Droguett, Frank Mücklich

RSC Advances, December 31, 2016

DOI: 10.1039/c6ra27794b

RSC Adv., 2017, 7, 5084 – 5092

9 pages

This work is the second of two parts addressing **Goal 1**.

Reproduced from Ref.^[118] with permission from the Royal Society of Chemistry.

Accessible online at <http://xlink.rsc.org/?DOI=C6RA27794B>

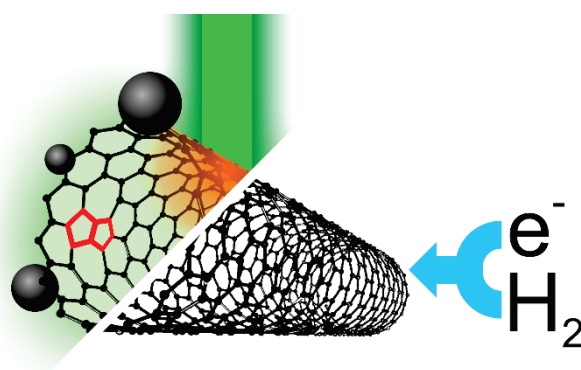


Figure 25 - Graphical abstract: defective (red pentagons) and contaminated (black spheres) SWCNT irradiated with green (532 nm) light, producing heat (orange glow). Right: defect- and impurity-free SWCNT injected with electrons and hydrogen.

Cite this: *RSC Adv.*, 2017, 7, 5084

Scaling up single-wall carbon nanotube laser annealing: effect on electrical resistance and hydrogen adsorption

Nicolas Souza,^{*a} Martín Roble,^b Donovan E. Diaz-Droguett^b and Frank Mücklich^a

Carbon nanotube (CNT) performance is highly sensitive to crystallinity and purity. These parameters are generally maximized to capitalise on the outstanding intrinsic properties of these 1-D nanocarbons. This presents challenges from their synthesis, through their manipulation, up to their inclusion in the final product. Many of these challenges can be addressed through fine-tuning the synthesis, yet CNT handling and processing (e.g. dispersion) often incurs unavoidable damage, with consequent drops in crystallinity and purity, and thus in overall performance. Laser annealing stands out as a contactless, fast and localised treatment, capable of drastic healing and purification. We previously demonstrated a near-full recovery of substantial processing-related damage to SWCNTs, applying very local (μm) laser radiation. Here, we scale-up our findings 10³-fold to entire as-produced samples (mm), confirming our previous findings of recrystallization and purification, and extend the scope to excellent correlation with non-trivial, ca. one-third, electrical resistance and hydrogen adsorption, at double the CNT thermogravimetry-based purity.

Received 5th December 2016
Accepted 31st December 2016

DOI: 10.1039/c6ra27794b

www.rsc.org/advances

1 Introduction

Evolving imaging techniques took nearly forty years to confirm the existence of new and exciting helical microtubules of graphitic carbon.^{1,2} In the following quarter century of – now named – carbon nanotube (CNT) research, major efforts to approach their extolled theoretical properties have successfully outperformed materials science's once senior materials.^{3–5} CNTs are thus poised to replace some of these materials within the foreseeable future, maturing into a nascent CNT industry. Yet the theoretical/experimental divide still holds, and at its core are insufficient crystallinity and purity, resulting in capped mechanical, electrical and optical properties.

While certain uses benefit from defective CNTs,^{6–8} most rely on the contrary.^{4,9} Advances in research have therefore made enormous leaps in optimising synthesis routes with current commercial quality >95% (understood as high purity and crystallinity). Equally intensive efforts into post-synthesis purification by mechanical, chemical and thermal techniques have further improved CNT quality.^{10–14}

Now, with such fine-tuned synthesis and complementary purification, a case can still be made for improved quality in: (1) applications that are highly sensitive to lattice defects or impurities; (2) excessively time- and cost-intensive synthesis

and/or purification; (3) inadequate purification due to further contamination/damage; (4) incompatible purification with certain applications when liquid processing-based; (5) unavoidable processing-related CNT damage and sulying (e.g., dispersion: ball milling, shear-mixing, ultrasonication, centrifugation, functionalisation);^{15–19} (6) wear-related damage.

Point (1) easily finds proponents in CNT electronics and threads. In the previous iteration of this study,²⁰ we examined current purification techniques, arguing points (2) to (5). Additionally, most are limited to purification and do not heal crystal defects. Accordingly, we presented the first in-depth study of CNT purification and healing, with power- and time-resolved laser radiation, standing out as fast, contactless and ambient.²⁰ A thorough review of the state of the art, including sample, atmosphere and laser characteristics, revealed a limited body of literature with understudied phenomena, often tangential to other core subjects.

With wide-ranging power and time variations, we were able to optimise single-wall CNT (SWCNT) quality and purity and base the modifications on energy density input. Combining several simple, established indicators based on Raman spectroscopy (peak ratios and widths), we showed a 94% improvement in crystallinity and a near 17-fold increase in purity. Finally, we applied these optimised parameters to successfully recover composite processing-based (dispersion) damage, addressing point (5).

Apart from the Raman effect, our assertions were based on the high mobility and thus low migration energies for vacancies (1 eV),²¹ interstitials (0.1 eV)¹⁰ and Dienes defects (3.5 eV)²² at

^aDepartment of Materials Science, Saarland University, 66123 Saarbrücken, Germany. E-mail: n.souza@mx.uni-saarland.de

^bInstituto de Física, Facultad de Física, Pontificia Universidad Católica de Chile, Casilla 306, Santiago, Chile

temperatures as low as 200 °C,²¹ well below that of the applied radiation, putting the energy at the single nanotube level at $\sim 10^{12}$ eV nm⁻²,²⁰ and a pondered surface temperature around 800 °C.²³ Although edges (open ends) and curvature-induced strain (small diameters and tube caps) are very reactive, carbonaceous impurities are even more so, thus effectively removed in an oxidative air atmosphere. Consequently, together with an abundance of carbonaceous material, the right conditions are present for further tube growth,²⁴ removal²⁵/incorporation²⁶ of aromatic carbon rings and olefinic/conjugated carbon chains, and general defect healing and impurity removal. Also competing and observed is chirality-based light absorption, by which 532 nm radiation preferentially excites (and removes) metallic tubes, as does 1064 nm radiation with semiconducting tubes.²⁷

However, the affected *ca.* \varnothing 11 μ m area from our study²⁰ rendered further site-specific correlative measurements very difficult. Given that sweeping assertions are not possible as to the governing mechanisms and the validity of the chosen Raman indicators, we decided to scale-up our findings to a sample-relevant measure that would allow for further scrutiny.

Here, we present a 10^3 -fold scaled-up treatment of SWCNTs with laser radiation in three phases: (1) energy density optimisation at the μ m scale, analogous to the previous study;²⁰ (2) transposition of said parameters to a more powerful laser with a greater beam diameter and a scanning laser head, for full sample treatment; (3) evaluation of the modification with Raman spectroscopy, and – previously unfeasible and non-existent in the literature – correlation with thermogravimetry (TG), electrical resistance and hydrogen adsorption measurements.

Raman-based improvements, analogous to our previous findings, of 90% in crystallinity and 20-fold purity could this time be contrasted with further correlative measurements, convincingly furthering our narrative with *ca.* one third the electrical resistance and hydrogen adsorption, and double the purity and crystallinity as per TG.

This points more clearly to impurity removal, even more so to defect healing/recrystallisation, as a result of tuned laser radiation, and allows for a more confident assertion as to its beneficial effects, supporting our previous claims. Finally, this scale-up brings our proposed method closer to industrial applicability. Combined with today's fine-tuned synthesis methods, laser radiation could possibly bring about previously unseen levels of CNT quality, or conversely, provide savings through simpler and robust CNT synthesis combined with laser post-treatment, resulting in quality equal to the former.

In this sense, our approach fits especially well in current post-synthesis CNT treatment efforts: "If you cannot beat them, join them". Instead of putting great effort into synthesising the right nanotube, post-growth treatments can bridge shortcomings in CNT synthesis. Chiral separation techniques such as selective chemistry, gel chromatography, dielectrophoresis, selective oxidation, ultracentrifugation and DNA wrapping chromatography have proven successful yet laborious.²⁸ On the other hand, metallic tubes can be laser-removed from the mix of chiralities in logic gates, leaving only switchable

semiconducting tubes;^{27,29,30} semiconducting tubes can be laser-removed, leaving only metallic tubes for metal matrix composites and contacts;²⁷ the field emission in CNT mats and powders can be enhanced with laser radiation for screens, improving uniformity and turn-on voltage;^{31,32} the tensile strength of CNT threads can be boosted by triggering tube-interlinking, chemically or with electron radiation, which improves load transfer;^{33,34} finally, fully analogous to CNTs due their sp² carbon, the electrical conductivity in graphene inks can be improved by laser radiation.³⁵

2 Materials and methods

2.1 SWCNTs

SWCNT mats were grown by pulsed laser deposition (PLD): a pulsed parallel laser beam (solid state Nd:YAG 10 Hz 10 ns-pulse Newport-SpectraPhysics Quanta-Ray 290) vaporises a carbonaceous cold-pressed target (ball-milled graphite, 0.6 at% Ni, 0.6 at% Co) inside a quartz tube furnace at 1200 °C flooded with 5 sccm of Ar at 0.7 bar. After one hour of deposition, the mats were peeled off the fan-cooled quartz tube end, exit the furnace. These pristine SWCNT mats, stretched over laboratory-grade silica glass substrates, constitute the object under study. Commercial arc-grown SWCNTs (Plasmachem) were also used to compare their hydrogen adsorption capacity.

2.2 Laser irradiation

This procedure reproduces our previous study,²⁰ intended to find optimal irradiation parameters. Initial local radiation (1) was carried out with the 532 nm (2.33 eV) continuous wave (CW) laser of the Raman system presented below (see 2.3), producing a 2.91 μ m laser spot.²⁰ Desired power attenuation levels were achieved by combining built-in filters with a rotationally, progressively metal-coated disc. With a power P from 0.176 to 1.76 W and fixed exposure time of 130 s, the sample was alternately irradiated with incremental powers (0.176 mW steps) and analysed by Raman spectroscopy *in situ*. Following the power sweep, a deduced optimal power P_1 was fixed in a second sweep on a different sample location, this time with varying exposure times t , from 0.1 to 0.5 s (0.1 s increments), also with intermittent Raman scans. The time sweep thus concluded on an optimal exposure time t_1 , in addition to the existing optimal power P_1 .

These parameters define the relevant energy density input, or fluence, composed of power density or irradiance, and exposure time. The irradiated area, defined by the beam spot diameter d_1 , completes the optimal fluence F_1 (eqn (1)):

$$F_1 = \frac{P_1 \times t_1}{\pi(d_1/2)^2} \quad (1)$$

This allows for a quick determination of the energy that is beneficial to SWCNTs, with fast radiation and *in situ* analysis, nimbler than a larger laser system with *ex situ* characterisation. A scaled-up radiation (2) was then carried out with a 940 nm (1.39 eV) diode laser (500 W LDM 500-20, Laserline),

at equal fluence, maintaining the optimised irradiance and exposure time ($t_1 = t_2$) (*i.e.* equal fluence) and a new beam spot diameter of 6 mm (d_2) (measured on irradiated polyimide and confirmed by mirroring CNT laser tracks with and without a 6 mm alumina mask on the sample, and confirming identical data spreads). Equal irradiance also reduces the unknown quantities and the uncertain physical effect of varying the exposure time together with the area. Thus, a simplified $F_1 = F_2$ gives the following expression for the sought scaled-up power P_2 :

$$P_2 = P_1 \left(\frac{d_2}{d_1} \right)^2 \quad (2)$$

Since the intention was to allow for sample scanning for complete treatment and/or patterning, the exposure time t_1 determined the scanning speed of the laser head, controlled by a three-axis CNC system (Bosch–Rexroth). To avoid anomalous power-up (threshold and shutter) events and acceleration effects, irradiation began outside of the sample, scanned across at constant speed and finished outside of the sample. A point on a sample is thus irradiated during t_1 as the beam diameter d_2 scans centred across it at a speed v :

$$v = d_2/t_1 \quad (3)$$

In a single line scan, eccentric points will receive shorter exposure times and lower power due to a Gaussian beam profile. Therefore, for full sample treatments, several line scans were performed at 50% track overlap, assuming d_2 is measured at the full-width at tenth maximum (FWTM) (worst case) (Fig. 1).

A point on the sample will therefore experience either (1) the summed power from every passage (Fig. 1: Σ) or (2) only the site-specific maximum power (Fig. 1: max.). In our previous study we observed that accumulated exposures of equal power or time had no effect on the SWCNTs, only producing changes upon an increase of either.²⁰ Thus, we believe the second scenario to be more realistic, with a sample-average 84% of the peak power (Fig. 1: av.). If the measured beam diameter were to correspond to a value below the FWTM (*e.g.*, $1/e^2$, $1/e$, full width at half-maximum), the radiation profile would be smoother and the average closer to peak power.

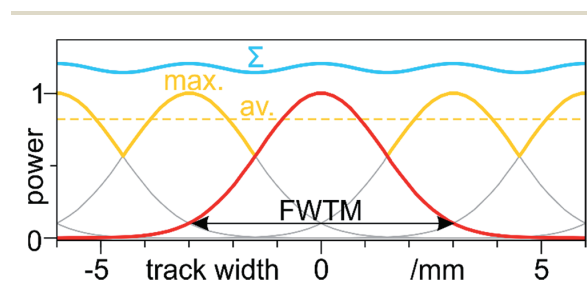


Fig. 1 Cross-section of 50%-overlapped (at the FWTM) Gaussian power profiles vs. track width, resulting from laser scanning. Highlighted are maximum power crests (yellow max.), their average (yellow dashed av.) and the sequential sum of every passage (blue Σ).

2.3 Material characterisation

Raman spectroscopy (Renishaw inVia) was carried out with 532 nm (2.33 eV) CW excitation and a 50 \times objective with 0.75 numerical aperture (see results for beam spot diameter). The laser power was set to 8.8 μ W (below a modification threshold of 17.6 mW as calculated previously²⁰ and confirmed here), and spectra were acquired between 100 and 3500 cm^{-1} with a 2400 line per mm grating. Spectra were baseline corrected through full-range noise linear regression. Standard indicators were extracted from the peak position and intensity ratios of Lorentz-fitted deconvolutions of Raman modes RBM, D, G⁺ and G'. Tube diameters d_t were calculated with $d_t = 234/\omega_{\text{RBM}}$.³⁶ Argumentation on the origin of these modes and the validity of their use can be found in our previous study.²⁰ Although peak ratios are unaffected by inter-spectrum normalisation, we have kept multi-spectrum datasets non-normalised to observe concentration- and crystallinity-sensitive effects in the Raman signal. The initial local radiation was studied *in situ*, while the scaled-up radiation was analysed in 12 mm line maps with a 0.5 mm step across a single laser-treated track, post treatment and *ex situ*.

In the same manner, 2-point electrical resistance measurements were performed on a micromanipulator stage (Signatone S-1160B-8N), along a 12 mm line map with a 0.5 mm step, centred across a single track. Two silver needles, each mounted on 3-axis μ m adjustment screws (Signatone S-725, 10 μ m resolution), contacted the SWCNT mat, penetrating its full thickness with a tip separation of *ca.* 200 μ m. This was calibrated optically, through an *in situ* optical microscope (Leica Stereo-Zoom, 1.5 \times objective, 10 μ m resolution) and a μ m ruler. The needle leads were PC-controlled and set at a constant voltage source of 2 V. Five line maps were carried out at different locations along the track.

For gas adsorption measurements, a fully scanned SWCNT sample region was dispersed in isopropyl alcohol with 7 min ultrasound, drop casted on a gold-coated microbalance AT-cut ($\sim 35^\circ$) quartz crystal and dried in ambient conditions. The water-cooled (20 $^\circ\text{C}$) microbalance (MDC SQM-310) was placed in a steel vacuum chamber and pumped down to a base 1.2×10^{-7} kPa by turbo and rotary pumps. Once isolated with a gate valve, the chamber was injected with hydrogen through a needle valve up to pressures between *ca.* 0.4 and 13.3 kPa, measured with a capacitive gauge (MKS instruments Baratron). For each pressure iteration, the *in situ* shift in resonance frequency Δf (eqn (4)) of the quartz crystal at saturation, with respect to that in vacuum, determined the adsorbed H_2 mass Δm based on Sauerbrey's equation:

$$\Delta f = -\frac{2f^2}{A\sqrt{\rho\mu}}\Delta m \quad (4)$$

where f is the resonant frequency, ρ is the density, μ is the shear modulus and A is the effective area. These are known constants of the quartz crystal, and together, their term is labelled C_t , approximately 81 $\text{Hz cm}^2 \mu\text{g}^{-1}$. Each hydrogenation step lasted 7 min before returning to base pressure and repeating. H_2 adsorption capacity is thus reported in wt% of the deposited

Paper

RSC Advances

mass on the quartz crystal as a function of injected pressure. Standard deviations (σ) are a result of the quasi-saturation frequency, which slightly increases after the injection-driven drop. Deposited masses are calculated from eqn (4) compared to the bare crystal. More information on this method can be found here.^{37,38}

SWCNT/ethanol dispersions, drop-casted on copper grids with a lacey carbon film (Gatan) were observed in a transmission electron microscope (TEM) (JEOL 2100F) at 200 kV. Thermogravimetry (TG) was carried out in a combined setup (Netzsch-Gerätebau Jupiter 449) with 10 mg of pristine and treated SWCNTs, heated at $10\text{ }^{\circ}\text{C min}^{-1}$ up to $800\text{--}900\text{ }^{\circ}\text{C}$ in air.

3 Results and discussion

3.1 Pristine SWCNT mats

The prepared SWCNT mats are 20 to 30 μm thick and are composed of randomly aligned \varnothing 10–40 nm bundles (Fig. 2a). Amorphous carbon covers the bundles (Fig. 2b) and permeates the sample in nodules, along with catalyst particles (Fig. 2a – bottom right). TG confirms the abundant carbonaceous species with a strong, early combustion around $400\text{ }^{\circ}\text{C}$, which slows down and saturates around $600\text{ }^{\circ}\text{C}$ (Fig. 2c).

CNT literature is awash in mentions of difficultly quantifiable purity. Two TG-based purity parameters, $T_1\%$ and m_R , are generally accepted parameters in commercial tubes.³⁹ Hereby, the mass and its derivative (equivalent to differential scanning calorimetry data) are used to identify different mass loss events and quantify water, CNT, non-CNT carbon, and metal/non-volatile species. The first is taken at $200\text{ }^{\circ}\text{C}$, point up to which the mass loss is attributed to adsorbed/trapped sample water (Fig. 2c – point A). Point B delimits the CNT species and arises from the T_1 abscissa, the minimum between the strongest

exothermal peak in the mirrored derivative mass ($-m'$) and the following peak. Further mass loss corresponds to other carbonaceous species until $625\text{ }^{\circ}\text{C}$ (point C), followed by non-volatiles/non-carbonaceous species. These four proportions thus allow for a carbonaceous purity of the CNTs (CNTs/CNTs + C), referred to as $T_1\%$, and the residual mass m_R , both corrected for initial moisture. Here, we find a $T_1\%$ of 46.7% and a m_R of 4.7%.

3.2 Local laser radiation: power and time

Their initial Raman signal (Fig. 3: red spectrum at 0 mW) presents an I_D/I_{G^+} of 0.09 and an $I_{G'}/I_D$ of 3.01. The radial breathing mode (RBM) is dominated by two main contributions (Fig. 3: inset against back plane), deconvoluted to 167.94 and 186.82 cm^{-1} , indicating a very narrow tube diameter distribution of 1.25 to 1.39 nm (inversely).

As the radiation power was increased, the intermittent Raman signal increased for all order-induced modes, RBM, G and G' (Fig. 3: dashed yellow peak paths). This strong non-proportional intensification reaches a maximum at 0.528 mW (Fig. 3: red spectrum at 0.528 mW). Since sample concentration did not increase nor did tube ends bundle, which are possible causes for signal increase,⁴⁰ we can posit impurity removal and recrystallization based on the following: the signal increase is not proportional for any mode; G^+ grows proportionately more than G^- and RBM; only one RBM peak grows, while the other is sustained. This also indicates metallic tube removal at this wavelength (532 nm),^{27,29,30} as previously clarified.²⁰ As to the disorder-induced D mode, a slight initial rise, possibly due to the removal of adsorbed water, is followed by an abrupt drop. This, to a certain extent, could explain an initial dampening of the other vibrational modes through the presence of carbonaceous contaminants. Yet the non-proportional behaviour of said modes, again points to competing mechanisms, removing

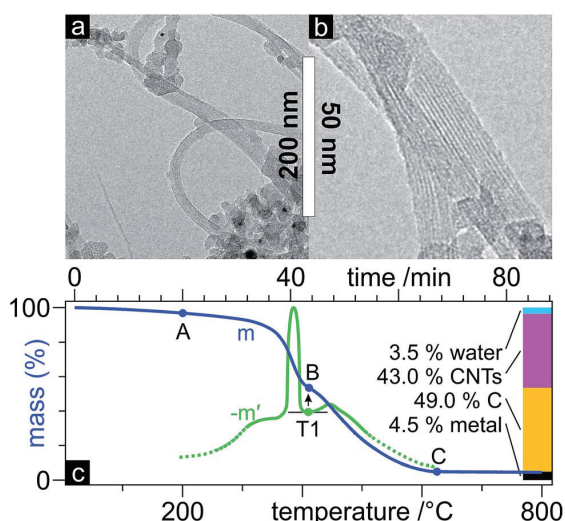


Fig. 2 TEM micrographies (a and b) of the pristine SWCNTs and TG mass (m) and (mirrored) derivative mass ($-m'$) curves (c) with global proportion bars.

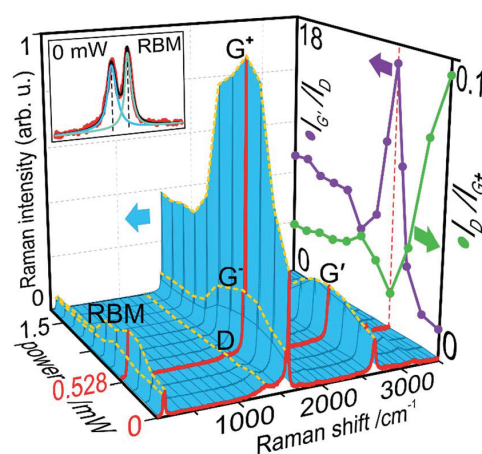


Fig. 3 Raman signal vs. power (blue 3-D surface) with highlighted (red) initial (0 mW) and optimal (0.528 mW) spectra, peak intensity variations (yellow dashed lines) of modes RBM, D, G^- , G^+ and G' , and a zoomed-in RBM (top-left rear plane); I_D/I_{G^+} and $I_{G'}/I_D$ ratios (right-hand plane).

defects, impurities and metallic tubes. Above 0.528 mW, all modes experience a more gradual decay, stabilising at levels below their initial values. This can be explained by tube damage and loss, with energy densities above that tolerable by these SWCNTs.

Given that proportionality – or a lack thereof – is key in Raman data, the I_D/I_{G^+} and $I_{G'}/I_D$ ratios further support the current narrative, both reaching their extremes at the same power of 0.528 mW (Fig. 3: right-hand plane). As previously seen, the defect density I_D/I_{G^+} is the first to react to the radiation with a near straight drop to a minimum 0.019. The purity index $I_{G'}/I_D$ barely changes after the first irradiation and then brusquely peaks at 16.7. These indicators further reveal the damaging effect of laser radiation above this power, both decaying until 0.88 mW. Tube damage, opening and burning contribute to these fluctuations, with defect density and purity often mirroring each other. Passed this point, these two ratios stabilise at values in between their extremes. These indications of increasing graphitisation and purification point to 0.528 mW as an approximate optimal power P_1 .

The next parameter necessary for a meaningful optimisation of the energy input is the exposure time. To this end, the power was fixed at P_1 during a sweep of the exposure time with intermittent Raman scans (Fig. 4). Again, the same non-proportional amplification of RBM (one of two peaks), G (mainly G^+) and G' , and decline of D, are observed, saturating around 0.3 s.

I_D/I_{G^+} drops promptly at 0.1 s and steadies by 0.3 s, to a minimum of 0.012. As previously observed, impurity removal is a longer process, and thus $I_{G'}/I_D$ reaches its maximum 20.74 in a less pronounced manner at 0.4 s. Therefore, a combined optimum is reached for both markers at t_1 0.4 s. In view of the subsequent scale-up, this time was taken where the observed markers plateaued, without accommodating for any further signal (isolated peaks) increase. This sweep saw an improvement upon both optimised markers, compared to the power

sweep, likely due to the extremely reduced time scale, far exceeded at 130 s exposures. P_1 and t_1 thus provide a measure of energy input for optimal laser healing and purification of the SWCNTs, 0.4 s of 0.528 mW, or 0.21 mJ.

3.3 Scale-up

At this point, we had optimised the laser energy based on Raman indicators, at a constant irradiated area in the μm scale. A scale-up to an industry relevant mm scale, carried out at constant irradiance, following eqn (2), was fed with the obtained parameters:

$$P_2 = P_1 \left(\frac{d_2}{d_1} \right)^2 = 0.528 \text{ mW} \left(\frac{6 \text{ mm}}{2.91 \times 10^{-3} \text{ mm}} \right)^2 = 2.2 \text{ kW}$$

This value for P_2 greatly surpasses the maximum available 500 W and is more than CNTs can sustain. For the scanning speed v , d_2 and t_1 in eqn (3) return 15 mm s^{-1} . To confirm the excessive power, a sample was treated with a 15 mm s^{-1} scan at 500 W and 6 mm spot size, with no remaining tubes as per Raman. Although scaling up laser radiation across different lasers and wavelengths can prove challenging, with absorption characteristics at play, we evaluated a possible false premise, namely d_1 .

This Raman laser beam diameter was calculated based on the Raman signal variation while scanning across an amorphous carbon fibre of known diameter.²⁰ We challenged said measurement with an alternate approach: (1) a power meter was partially covered with a compacted opaque (verified) layer of SWCNTs, as particularly good light absorbers, to avoid reflection and diffraction; (2) the power meter was placed on the sample stage with its surface at the focal plane and the CNTs blocking any transmission; (3) moving the power meter in a straight line across the focal plane, the displacement was measured for a power variation from 0 to its maximum, yielding $25.1 \mu\text{m}$ (Fig. 5).

Now, there is inherent complexity in measuring Gaussian-profile beam diameters without a beam profiler. The initial approach might fall short due to the sensitivity threshold of the Raman spectrometer, in the parts-per-million for carbon phases, at the centre of the beam. Yet the wide-ranging, asymptotic arms of the Gaussian profile, when falling below said threshold, were possibly cut off, underestimating d_1 . On the other hand, this new approach can be seen as an overestimation. Indeed,

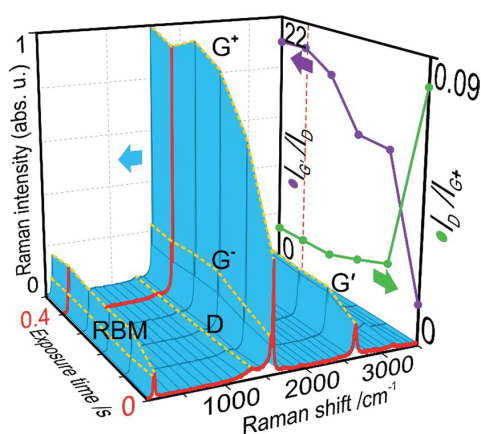


Fig. 4 Raman signal vs. exposure time (blue 3-D surface) with highlighted (red) initial (0 s) and optimal (0.4 s) spectra, peak intensity variations (yellow dashed lines) of modes RBM, D, G^- , G^+ and G' ; I_D/I_{G^+} and $I_{G'}/I_D$ ratios (right-hand plane).

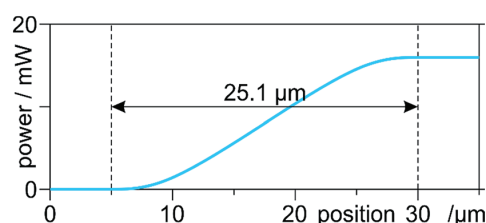


Fig. 5 Measured power vs. stage position. The transition of ca. $25.1 \mu\text{m}$ is the average of five scans.

Paper

RSC Advances

measures were taken to avoid reflection and diffraction, yet they cannot be ruled out completely; not to mention, fluorescence and stray light. These phenomena falsely widen the detection area for the power meter. This does not invalidate our previous results, since it only changes the irradiance values, not the underlying phenomena. In order to build upon our proof of concept from said study, we continued with this new value for d_1 . Finally, note that this is not a direct transposition of radiation from the μm to the mm scale, since it only considers the emission, not the absorption, which is strongly dependent on wavelength. Thus, this remains an approximate reference for mm-scale modification of SWCNTs.

This 8-fold beam diameter was referred into eqn (2), returning a P_2 of 30.17 W. This time, a 15 mm s^{-1} scan at 30 W did not visibly burn the tubes and was further probed. Based on the satisfactory results, resembling what was expected, the apparent fruition of this scale-up was validated with enough accuracy for the frame of this study.

Electron microscopy cannot carry the burden of proof concerning local/environmental disorder. The very local nature of TEM does not allow for conclusive results, furthermore its preparation through sonication rises questions with respect to the homogenous reallocation of impurities throughout the sample and ultrasound is known to cause defects in SWCNTs. Nonetheless, the laser-treated sample was observed in TEM, unfortunately, with no major differences compared to the pristine state. TG, however, provides information on a much greater sample size and is thus more statistically relevant. Fig. 6 shows a much higher oxidation-onset temperature for the laser-treated SWCNTs, pointing to a higher degree of graphitization and less defects and disorder. A T_1 of 90.7% almost doubles the pristine 46.7% SWCNT purity.

A single laser scan across a sample was then further analysed by Raman spectroscopy and electrical resistance measurements (Fig. 7). The plotted I_D/I_{G^+} and I_{G^+}/I_D (Fig. 7a) along a 12 mm line across the track show different extensions in their deviation from their initial pristine values, but both exceed the 6 mm track. This is to be expected, since photothermal and photochemical effects govern the laser treatment.⁴¹ The thermal component and the excellent heat conduction of SWCNTs thus produce a heat-affected zone (HAZ) beyond the irradiated area.

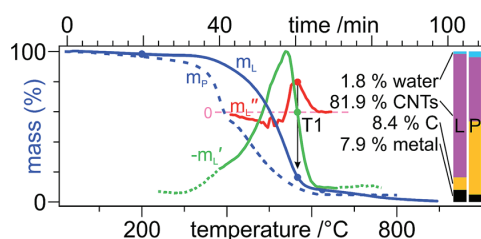


Fig. 6 TG mass (m_L) (blue) and (mirrored) first ($-m'_L$) (green) and second (m''_L) (red) derivative curves with global proportion bars of the laser-treated (L) samples, as well as the mass curve (m_P , dashed) and proportion bars of the pristine (P) sample. In the absence of a distinct second peak in $-m'_L$, its inflection point (local maximum in m''_L) determines T_1 .³⁹

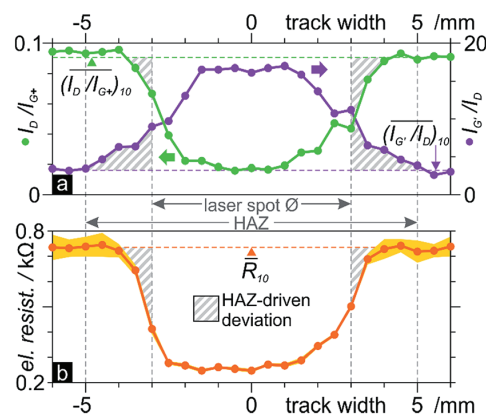


Fig. 7 12 mm scans across a laser track at 0.5 mm steps of: (a) Raman I_D/I_{G^+} (left, green) and I_{G^+}/I_D (purple, right) ratios; (b) 200 μm electrical resistance (five scan average points with σ surface). The dashed lines indicate 10-point pristine averages. The hashed surface denotes data points that deviate from this value, outside the track, and are thus HAZ-driven.

Judging from I_{G^+}/I_D , the HAZ extends *ca.* 10 mm, an extra 2 mm on either side of the track. Although not smooth, both plots present bell-shaped curves. That of the defect density, I_D/I_{G^+} , deviates from its pristine state 0.5–1 mm beyond the track, half as much as the purity I_{G^+}/I_D . This indicates that defects are less sensitive to temperature than impurities. Peak values of either I_D/I_{G^+} and I_{G^+}/I_D of *ca.* 0.02 and 17, respectively, did not reach those from the local radiation (0.01 and 20, respectively), possibly from a slightly overestimated d_1 .

Since the scaled-up radiation was performed with 940 nm (1.39 eV) vs. the local 532 nm (2.33 eV), the slight disparity in Raman parameters could be discussed by means of the absorption characteristics at each wavelength. However, chirality-dependent absorption mechanisms and our polychiral sample render this discourse moot.

The electrical resistance also presents a bell-shaped curve, from a pristine 0.74 k Ω to 0.25 k Ω in the middle of the track (Fig. 7b). That is a third of the resistance in the laser-treated tubes. The negligible standard deviation compared to the variability outside the track shows how laser radiation homogenises the sample. The plot resembles that of I_D/I_{G^+} , in its asymmetry and width. This makes sense, given that electrical conduction in a SWCNT occurs through the delocalised π -cloud electrons. These are provided by the orthogonal p_z orbitals which, in the presence of crystal defects, are distorted or absent (vacancies). Although tube wall contaminants can perturb its electronic states and cause depletion or accumulation of carriers⁴² and purification does improve conduction, crystallinity seems to have a greater influence. The improved conductivity is also attributable to the known preferential removal of semiconducting tubes with near infrared wavelengths (785–1064 nm),²⁷ leaving primarily metallic tubes due to the 940 nm radiation. This therefore confirms our previously theorised preferred conduction paths, along the laser-annealed track, *versus* other directions, and

confirms the findings of Del *et al.* who improved conductivity in graphene inks with laser annealing.³⁵

Finally, the effect of the laser treatment on hydrogen adsorption was studied on samples taken from the centre of the track and an unaffected region. A commercial SWCNT sample was also put to the test to provide a normalised context regarding methodology and achievable pressures. All three samples show an uninterrupted mass/pressure proportionality, which slows down at 3–5 kPa towards apparent saturation (Fig. 8a). The laser-annealed tubes show a 30 to 50% adsorption compared to the pristine tubes throughout the range of probed pressures, with a final *ca.* 0.5 and 1 wt% (respectively) around 14 kPa. The commercial tubes maintain 20 to 30% superior values over the pristine tubes, approaching them around saturation followed by a slight divergence, reaching around 1.3 wt%. Crystallinity, purity and tube diameters are summarised in Fig. 8b for structural correlations.

The governing hydrogen storage mechanism is currently unclear,⁴³ but there is consensus on the fact that defective CNTs perform better.^{43,44} CNTs are extremely porous and offer high surface area for adsorption on and in the tubes, with overlapping potential fields on opposite walls creating attractive forces.⁴⁵ Hydrogen storage is physisorption-like in nature, with preferential adsorption on defect sites.^{43,44} This correlates perfectly with our results, showing the laser-annealed tubes, with less defects (Fig. 8b), well below the storage capacity of the pristine tubes. Furthermore, larger tube diameters and small bundles improve hydrogenation, by freeing up surface in otherwise restrained tubes.⁴⁴ This explains the superior capacity of the commercial sample, which, although equally defective as the laser-treated tubes, has far larger tubes than the other samples (Fig. 8b: black segments). No significant differences in

the adsorption kinetics were observed, with 120 to 80 s saturation times (from inlet to resonance frequency stabilisation) throughout the range of pressures. For comparison, Pd films (less porous) saturate in around 50 s under equal conditions,³⁷ and multiwall CNTs do so in under 100 s.⁴⁶

Concerning the effect of impurities in CNT samples, studies often compare pristine and acid-purified tubes: claims of higher H₂ uptake are often correlated with higher purity due to enhanced surface area⁴⁵ or opened ends.⁴⁷ However acid treatments are known to cause severe damage in the crystal lattice,⁴⁰ thus clouding said results with undiscussed competing effects of multiplied active defect sites. Among our directly comparable samples, pristine and laser-annealed, the latter are much purer due to the laser treatment, yet fared unfavourably with respect to H₂ uptake. This either contradicts the literature or marks crystallinity as decisive in the corresponding adsorption mechanisms. Considering the removed metal catalysts – advantageous for gas adsorption⁴⁷ – during laser radiation, the same argument can therefore be made for the governance of crystallinity.

Dedicated hydrogenation studies have tested pressures in the 10 MPa range, with earlier mixed reports and overestimated results, now stagnating at around 1.7 wt%.⁴³ This not dissimilar value at an order of magnitude the pressure, provides context and understanding of the qualitative differences in our samples (note that our samples were not pre-baked or moisture-free sealed, and can thus contain up to 10 wt% water, obscuring results). This is a further confirmation that laser radiation recrystallises and purifies the SWCNTs. Lastly, the reduced standard deviation, as with the electrical resistance, underlines the homogenising effects of the radiation.

4 Conclusions

We optimised a 25 μm spot of 532 nm laser radiation on SWCNTs, extracting 0.528 mW of power and 0.4 s of exposure time from comparative Raman peak intensity ratios that maximise crystallinity and purity. This was scaled-up at constant fluence to a 6 mm spot, scanning-head, 940 nm laser, translating to 30 W and 15 mm s⁻¹ scanning.

A laser line-scan across a sample reached Raman ratios close to those at the μm scale. A heat-affected zone of above-average purity and crystallinity reached respectively 2 and 1 mm on either side of the track, confirming slow, thermal purification and photonic excitation-driven recrystallisation. The centre of the track showed an average 250 Ω electrical resistance, a third of the 750 Ω in the untreated tubes. These points correlated more closely with those of the crystallinity, in shape and extension, indicating the dominant effect of lattice defects on electrical resistance, which disrupt the delocalised e⁻ cloud, compared to impurities. Laser-treated tubes from the centre of the track demonstrated 30 to 50% the hydrogen adsorption capacity of untreated tubes. Since hydrogen uptake occurs mainly at defect sites, this implies more crystalline and pure laser-annealed tubes.

This scaled-up, simple, efficient and ambient treatment puts forth (1) abundant and upfront indications that laser radiation

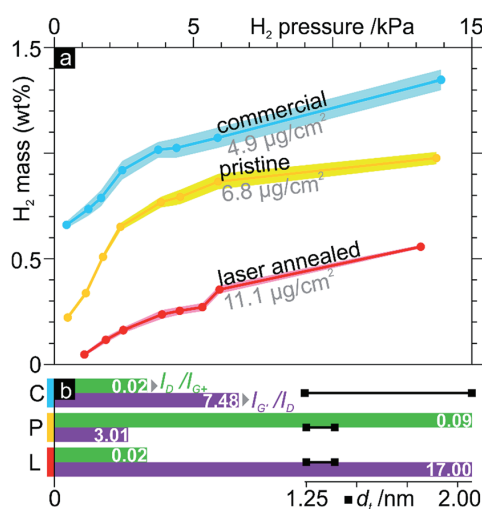


Fig. 8 (a) H₂ gas adsorption (with deposited mass and σ areas) as a function of H₂ pressure, (b) I_D/I_G (green bars), I_G/I_D (purple bars) and tube diameter (d_t) (black segments) distribution (as per RBM frequencies) of commercial (C), pristine (P) and (scaled up) laser-annealed (L) samples.

effectively heals defects, removes impurities and homogenises the sample, as confirmed by Raman spectroscopy, electrical resistance, hydrogen adsorption and TG. Furthermore, this (2) adds to the validity of extensively used, yet contested Raman I_D/I_G and I_G/I_D ratios as indicators of crystallinity and purity. Furthermore, (3) the application-relevant mm scale brings this promising technique closer to industry with sights on higher quality tubes, cheaper synthesis and recovery of unavoidable processing-related damage. This can be extended to unachievable tube qualities, due to alternative complex organic precursors,⁴⁸ bringing such CNTs up to industry standards and closer to sustainability. A final corollary of damage recovery is (4) the possible rejuvenation of electrical cycling or wear-related damage to CNT materials, to extend their duty life.

Advancing controllability of CNT synthesis, chirality purification and tube quality could benefit from this swift and scalable CNT treatment to reach new standards in CNT quality, recover CNT damage, and generally improve performance in CNT-based materials and devices.

Acknowledgements

This work was supported by the SUMA2 Network Project, 7th Framework Program of the European Commission (IRSES Project No. 318903), and the CREATE-Network Project, Horizon 2020 Program of the European Commission (RISE Project No. 644013). Many thanks to Matias Míguez for the electrical resistance set-up, Prof. Volker Presser for the Raman spectrometer, Aura Tolosa for TEM imaging and Marco Zeiger for TG. M.Sc. Federico Lasserre is kindly acknowledged for corrections and discussions. D. D.-D. thanks the 11130555 Fondecyt project from the Chilean Government.

Notes and references

- 1 L. V. Radushkevich and V. M. Lukyanovich, *Zh. Fiz. Khim.*, 1952, **26**, 88.
- 2 S. Iijima, *Nature*, 1991, **354**, 56–58.
- 3 B. G. Demczyk, Y. M. Wang, J. Cumings, M. Hetman, W. Han, A. Zettl and R. O. Ritchie, *Mater. Sci. Eng., A*, 2002, **334**, 173–178.
- 4 M. M. Shulaker, G. Hills, N. Patil, H. Wei, H.-Y. Chen, H.-S. P. Wong and S. Mitra, *Nature*, 2013, **501**, 526–530.
- 5 M. F. L. De Volder, S. H. Tawfik, R. H. Baughman and A. J. Hart, *Science*, 2013, **339**, 535–539.
- 6 J. A. Robinson, E. S. Snow, Ş. C. Bădescu, T. L. Reinecke and F. K. Perkins, *Nano Lett.*, 2006, **6**, 1747–1751.
- 7 M. Wong, M. Paramsothy, X. J. Xu, Y. Ren, S. Li and K. Liao, *Polymer*, 2003, **44**, 7757–7764.
- 8 Y. Piao, B. Meany, L. R. Powell, N. Valley, H. Kwon, G. C. Schatz and Y. Wang, *Nat. Chem.*, 2013, **5**, 840–845.
- 9 J. Stein, B. Lenczowski, E. Anglaret and N. Fréty, *Carbon*, 2014, **77**, 44–52.
- 10 P. G. Collins, in *Oxford Handbook of Nanoscience and Technology: Volume 2: Materials: Structures, Properties and Characterization Techniques*, ed. A. V. Narlikar and Y. Y. Fu, 2010, pp. 1–73.
- 11 H. Jia, Y. Lian, M. O. Ishitsuka, T. Nakahodo, Y. Maeda, T. Tsuchiya, T. Wakahara and T. Akasaka, *Sci. Technol. Adv. Mater.*, 2005, **6**, 571–581.
- 12 S. Bandow, A. Rao and K. Williams, *J. Phys. Chem. B*, 1997, **5647**, 8839–8842.
- 13 K. B. Shelimov, R. O. Esenaliev, A. G. Rinzler, C. B. Huffman and R. E. Smalley, *Chem. Phys. Lett.*, 1998, **282**, 429–434.
- 14 A. Suri and K. S. Coleman, *Carbon*, 2011, **49**, 3031–3038.
- 15 H. J. Park, M. Park, J. Y. Chang and H. Lee, *Nanotechnology*, 2008, **19**, 335702.
- 16 Y. Wang, J. Wu and F. Wei, *Carbon*, 2003, **41**, 2939–2948.
- 17 P. Garg, J. L. Alvarado, C. Marsh, T. a. Carlson, D. a. Kessler and K. Annamalai, *Int. J. Heat Mass Transfer*, 2009, **52**, 5090–5101.
- 18 S. Song, H. Yang, R. Rao, H. Liu and A. Zhang, *Catal. Commun.*, 2010, **11**, 783–787.
- 19 K. S. Munir and C. Wen, *Crit. Rev. Solid State Mater. Sci.*, 2016, **8436**, 1–20.
- 20 N. Souza, M. Zeiger, V. Presser and F. Mücklich, *RSC Adv.*, 2015, **5**, 62149–62159.
- 21 A. V. Krashenninikov, P. O. Lehtinen, A. S. Foster and R. M. Nieminen, *Chem. Phys. Lett.*, 2006, **418**, 132–136.
- 22 M. Monthieux and J. C. Charlier, *Carbon*, 2014, **75**, 1–4.
- 23 T. Nakamiya, T. Ueda, T. Ikegami, F. Mitsugi, K. Ebihara, Y. Sonoda, Y. Iwasaki and R. Tsuda, *Thin Solid Films*, 2009, **517**, 3854–3858.
- 24 D. B. Geohegan, H. Schittenhelm, X. Fan, S. J. Pennycook, A. A. Puzos, M. A. Guillorn, D. A. Blom and D. C. Joy, *Appl. Phys. Lett.*, 2001, **78**, 3307.
- 25 U. Brand, H. Hippler, L. Lindemann and J. Troe, *J. Phys.*, 1990, **94**, 6305–6316.
- 26 L. Pang, L. Prochazka and R. Quezada, *Fuel and Energy Abstracts*, 1995, **36**, 189.
- 27 A. Roch, T. Roch, E. R. Talens, B. Kaiser, A. Lasagni, E. Beyer, O. Jost, G. Cuniberti and A. Leson, *Diamond Relat. Mater.*, 2014, **45**, 70–75.
- 28 H. Liu, D. Nishide, T. Tanaka and H. Kataura, *Nat. Commun.*, 2011, **2**, 309.
- 29 M. Mahjouri-Samani, Y. S. Zhou, W. Xiong, Y. Gao, M. Mitchell and Y. F. Lu, *Nanotechnology*, 2009, **20**, 495202.
- 30 H. Huang, R. Maruyama, K. Noda, H. Kajiura and K. Kadono, *J. Phys. Chem. B*, 2006, **110**, 7316–7320.
- 31 J. Yotani, S. Uemura, T. Nagasako, H. Kurachi, H. Yamada, T. Ezaki, T. Maesoba, T. Nakao, M. Ito, T. Ishida and Y. Saito, *Jpn. J. Appl. Phys.*, 2004, **43**, L1459–L1462.
- 32 K. F. Chen, K. C. Chen, Y. C. Jiang, L. Y. Jiang, Y. Y. Chang, M. C. Hsiao and L. H. Chan, *Appl. Phys. Lett.*, 2006, **88**, 2005–2007.
- 33 D. N. Ventura, *Synthesis of Cross-Linked Carbon Nanotube Mats and Their Applications*, Florida State University, 2011.
- 34 B. Peng, M. Locascio, P. Zapol, S. Li, S. L. Mielke, G. C. Schatz and H. D. Espinosa, *Nat. Nanotechnol.*, 2008, **3**, 626–631.
- 35 S. K. Del, R. Bornemann, A. Bablich, H. Schäfer-Eberwein, J. Li, T. Kowald, M. Östling, P. Haring Bolivar and M. C. Lemme, *2D Mater.*, 2015, **2**, 11003.
- 36 C. Fantini, A. Jorio, M. Souza, M. S. Strano, M. S. Dresselhaus and M. A. Pimenta, *Phys. Rev. Lett.*, 2004, **93**, 1–4.

RSC Advances

Paper

- 37 R. El Far, D. E. Diaz-Droguett, S. Rojas, J. I. Avila, C. P. Romero, P. Lievens and A. L. Cabrera, *Thin Solid Films*, 2012, **522**, 199–203.
- 38 E. Mosquera, D. E. Diaz-Droguett, N. Carvajal, M. Roble, M. Morel and R. Espinoza, *Diamond Relat. Mater.*, 2014, **43**, 66–71.
- 39 R. Jansen and P. Wallis, *Mater. Matters*, 2009, **4**, 23.
- 40 K. Ramadurai, C. L. Cromer, A. C. Dillon, R. L. Mahajan and J. H. Lehman, *J. Appl. Phys.*, 2009, **105**, 93106.
- 41 K. Hurst and A. Dillon, *J. Phys. Chem. C*, 2008, **112**, 16296–16300.
- 42 M. J. O. Connell, D. Ph and F. Group, *Carbon Nanotubes Properties and Applications*, 2006.
- 43 S. M. Lee, K. H. An, W. S. Kim, Y. H. Lee, Y. S. Park, G. Seifert and T. Frauenheim, *Synth. Met.*, 2010, **121**, 1189–1190.
- 44 K. Shen, H. Xu, Y. Jiang and T. Pietraß, *Carbon*, 2004, **42**, 2315–2322.
- 45 G. E. Ioannatos and X. E. Verykios, *Int. J. Hydrogen Energy*, 2010, **35**, 622–628.
- 46 M. Morel, E. Mosquera, D. E. Diaz-Droguett, N. Carvajal, M. Roble, V. Rojas and R. Espinoza-González, *Int. J. Hydrogen Energy*, 2015, **40**, 15540–15548.
- 47 S. Banerjee, S. Murad and I. K. Puri, *Proc. IEEE*, 2006, **94**, 1806–1814.
- 48 N. Souza, F. Lasserre, A. Blickley, M. Zeiger, S. Suárez, M. Duarte, V. Presser and F. Mücklich, *RSC Adv.*, 2016, 72596–72606.

4.3. Upcycling spent petroleum cracking catalyst (FC3R): pulsed laser deposition of single-wall carbon nanotubes and silica nanowires

N. Souza, F. Lasserre, A. Blickley, M. Zeiger, S. Suárez, M. Duarte, V. Presser, F. Mücklich.

RSC Advances, July 25, 2016

DOI: 10.1039/C6RA15479D

RSC Adv., 2016, 6, 72596 -72606

11 pages

This work addresses **Goal 2**.

Reproduced from Ref.^[119] with permission from the Royal Society of Chemistry.

Accessible online at <http://xlink.rsc.org/?DOI=C6RA15479D>

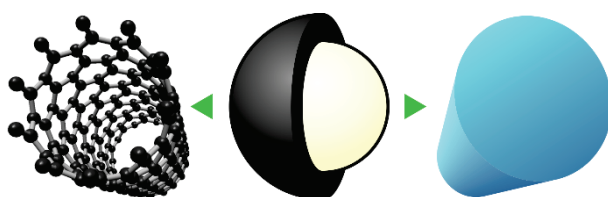


Figure 26 - Graphical abstract: FC3R particle (centre) with a zeolite core and graphitic shell produces SWCNTs (left) and SiONWs (right)

Cite this: *RSC Adv.*, 2016, 6, 72596

Upcycling spent petroleum cracking catalyst: pulsed laser deposition of single-wall carbon nanotubes and silica nanowires

N. Souza,^a F. Lasserre,^a A. Blickley,^{ab} M. Zeiger,^{ac} S. Suárez,^a M. Duarte,^d V. Presser^{ac} and F. Mücklich^{*a}

Fluid catalytic cracking (FCC), which currently accounts for half of the worldwide petroleum refining efforts, relies on catalytic, aluminosilicate zeolite particles which slowly deactivate. As of yet, this FCC catalyst residue (FC3R) has no commercial outlet, resulting in abundant amounts of landfill-destined refuse. However, this overlooked waste has the right ingredients for the synthesis of some of today's emerging nanomaterials. High-carbon FC3R, sourced from a Uruguayan refinery, was identified as faujasite particles encased in graphitic carbon shells. We show that pulsed laser ablation of raw FC3R produces simultaneous deposition of single-wall carbon nanotubes and silica nanowires through vapour/solid-liquid-solid self-assembly in distinct zones of an oven-laser apparatus. This is an extreme revalorisation and provides a new untapped resource for research and applications in C- and Si-based nanomaterials and mesoscopic physics.

Received 14th June 2016

Accepted 24th July 2016

DOI: 10.1039/c6ra15479d

www.rsc.org/advances

1. Introduction

Petroleum refining relies on cracking of large gasoil molecules into smaller vapour-phase distillable products. Depending on geographical location, specific fuel needs and crude origin, refineries employ different catalytic cracking installations. Fluid catalytic cracking (FCC) and hydroprocessing (-treating & -cracking) (HP) comprise 48% and 24% of the installed capacities in refineries world-wide.¹ FCC occurs at high temperatures with the help of a fluidised *catalyst* powder, modern versions of which consist mainly of faujasite, as well as an amorphous alumina matrix, a silica sol binder and a kaolinite clay (silica and alumina) filler.¹ The zeolite faujasite (FAU) is a crystalline aluminosilicate mineral (2–5 Si/Al atomic ratio) with a primitive cell consisting of 18-membered sodalite cages, orthogonally connected by hexagonal prisms. These result in a primary supercage and secondary pore structures which confine the hydrocarbons and, together with coordinated oxygen and sodium ions ($192[(\text{Si}/\text{Al})\text{O}_4]^{4-/5-}$ tetrahedrons per unit cell), act as Brønsted/Lewis acids and crack them.² Of the 200-some documented types of zeolite, two types of FAU exist, X and Y, each in a variety of modifications (de-/sodiated, de-/hydrated,

ultrastable, very ultrastable, dealuminated³). Although zeolite Y is the current FCC standard, its composition (modification) can also vary to adapt to real-time crude input and market output needs.¹

During cracking, petroleum coke (PC) accumulates on different locations and components of the FCC unit (conduits, chambers, chimneys). This form of coke, specific to the petrochemical industry, is a high carbon content fuel, also rich in sulphur and metals, that infiltrates (*i.e.*, poisons) and deposits on (*i.e.*, fouls) the catalyst, significantly reducing the catalytic activity.⁴ The PC is thus periodically burned off to maintain activity in a regenerator, the produced heat is refed into the system (FCC C–C cleaving is endothermic) and the catalyst is recirculated for further catalysis. A fraction of this circulating *equilibrium catalyst* (ECAT) is thus continually renewed in order to maintain activity and reduce metal and sulphur contents.⁵ Over time, however, the catalyst suffers stronger yield decline with irreversible decay due to poisoning and fouling (PC, metals and sulphur) and sintering (collapse of crystalline structure and loss of surface area),⁴ requiring further cyclone removal or electrostatic precipitation, yielding the eponymous *electrostatic precipitator catalyst* (EPCAT).⁶ Thus, ECAT & EPCAT are extracted in the form of off-white to black powders/rocks, depending on the coke content, referred to as *FCC catalyst residue* (FC3R), or in a broader sense, as *catalyst coke* or *catalyst fines* (catfines), to include *hydroprocessing catalyst residue* (HPCR). At this stage, these residues can be rejuvenated for reuse, a limited amount of times,⁷ eventually becoming waste. For the purpose of this work, spent catalyst or FC3R will designate that which is non-regenerable with no residual functional activity.

^aDepartment of Materials Science, Saarland University, 66123 Saarbrücken, Germany. E-mail: muecke@matsci.uni-sb.de

^bDepartment of Materials Science and Engineering, Drexel University, Philadelphia, PA 19104, USA

^cINM – Leibniz Institute for New Materials, 66123 Saarbrücken, Germany

^dEngineering and Technology School, Catholic University of Uruguay, 11600 Montevideo, Uruguay

FC3R is often assigned to PC in yield statistics as a subcategory.⁸ Although a by-product, upon extraction and/or purification, most PC is marketed as a commonplace global commodity. Disposal is thus avoided, recycling added-value materials back into the industry. Established buyers include power generation, cement, metallurgy and industrial. Indeed, coke (PC or other) can substitute coal for domestic heating purposes and is used in the metallurgical industry as fuel or reducing agent.⁹ NASA has used coke, combined with other materials, as heat shielding in various missions.¹⁰ Yet, marketable coke must be relatively pure carbon; that is why FC3R, with its high amounts of zeolite, is not considered as such. FC3R is the largest catalyst waste category in refineries.¹¹ In 2006, 0.5 MT of FCC catalyst were being used worldwide,¹² which will inevitably end up in landfills due to lacking technology, profitability and regulation.

Research is currently exploring outlets for spent cracking catalysts. To this end, in addition to the variety of zeolites (and their modifications) used in petroleum refining, an important distinction arises between FCC and HP catalyst waste, and therefore, their ensuing disposal/recycling. HP catalysts contain very high amounts of metal (Mo, Ni, V, Co, W) and their disposal/reuse implies potential metal leaching. Because of this, although both FC3R and HPCR must undergo treatment in order to meet ever stringent environmental standards, the latter metal-laden catalyst awaits greater hurdles.⁷ In fact, HPCR is labelled hazardous (US & EU)^{13,14} and cannot be exported to/from third world countries according to the Basel Convention and OECD rules.¹⁵ FC3R, on the other hand, is non-hazardous.¹⁴

A European Commission initiative from 1991 foresaw construction materials as a potential outlet for FC3R¹⁶ but it was not until 1997 that it was studied.¹⁷ Largely dominated by FC3R, spent catalysts have since been tested as substitute or aggregate in a variety of admixtures, mainly for construction. In addition to refractories^{18,19} and ceramic frits,²⁰ their pozzolanic activity seems to hold the greatest promise: high-performance Portland cements, pastes, binders, mortars and concretes have been successfully manufactured with cement substitution rates of up to 40 wt%.²¹ The characteristics of these composite products *versus* their standard counterparts range from similar quality to 117% pozzolanic activity,²¹ 147% compressive strength²² and improved hydraulics, durability, bleeding and setting times. Despite these very promising results, spent catalysts are not yet marketed.

In our experiments, the carbon coke in FC3R was considered to provide an interesting alternative carbon feedstock for carbon nanotube (CNT) synthesis. Apart from the necessary carbon, some of the elements present in FC3R are known catalysts in CNT growth. Although Al and Si do not directly take part in CNT growth,²³ their oxides have been extensively used as growth support²⁴ and Si can enhance growth through oxidation.²⁵ The 48% void fraction of FAU can be conducive to higher CNT yields.²⁶ Furthermore, trapped oxygen could burn off amorphous carbon, increasing CNT purity. Finally, sulphur is known to broaden the diameter distribution²⁷ and to produce Y-junctions through structural defects.²⁸

In addition, the aluminosilicate zeolite content in FC3R was expected to be conducive to silicon-based nanowires, namely silica nanowires (SiONWs). These lesser known nanohomologues exhibit excellent (blue) photoluminescence, which has dominated their study as well as their applications, dating back to their discovery in 1998.²⁹ Together with gold nanoparticles they feature a surface plasmon resonance absorption that can be used for photothermal cancer therapy.³⁰ Bolstered by their physical and chemical stability, large surface area, and biocompatibility, SiONWs are also envisioned and studied in biosensing³¹ and solar cells.³² Their chemistry is easily tuneable thanks to well-established protocols for surface modification.^{33,34} These rods have an ultimate strength one and two orders of magnitude above that of Kevlar and high-strength steel, respectively.³⁵

Pulsed laser deposition (PLD),³⁶ a branch of laser ablation (LA), was envisaged as a suitable means for these experiments. PLD is one of the principal established techniques for the growth of nanowires and -tubes. Although continuous wave (CW) lasers can ablate without the help of an oven,³⁷ pulsed lasers are usually preferred for LA due to the higher peak power output, accumulated between each pulse and released in very short, discrete ns pulses.³⁸ This renders PLD more controllable with respect to the plume dynamics emanating from the solid feedstock (target).³⁸ Chemical vapour deposition (CVD), another standard technique for either nanostructure, is generally fed by a gaseous precursor. Solids such as FC3R would require costly and laborious liquid-state chemistry to produce sprayable or vaporisable solutions/suspensions, easily surpassing the cost of the synthesis itself. Thermal evaporation would not manage the variety of species present in the FC3R. In arc discharge (Arc), a more energy-intensive CNT synthesis route, the anode is consumed in favour of CNT-containing soot that builds up on the cathode. Compared to the required standard, high-purity graphite electrodes, the aluminosilicates in the FC3R would not guarantee the necessary conductivity. Supposing it would, its anisotropy and alternating compositions of layered cokes, would alter the field lines and cause the arc to wander, rendering the discharge plasma unstable and unfavourable to prolonged nanotube growth. Not to mention, Arc is incompatible with SiONW growth and the aluminosilicates would be lost in the process. Finally, contrary to ablated graphite, which contributes single atoms to the CNTs, larger aromatic species present in the coke can be directly incorporated by PLD.³⁹

Common precursors for CNTs are carbon-containing gases and graphite. Si sources for SiONW precursors include: silicon wafers, silane, silicon-based powders (Si, SiC, SiO₂) and silica xerogel (mesoporous silica); oxygen can be found in the Si sources, metallic oxides can be fed in the gas phase or in impurities from other process gases (*e.g.*, H₂, N₂, Ar), and/or mixtures thereof. Catalysts for either nanostructure are usually metals, for example, Fe, Co, Ni, Ga, Au, Sn or Pd.^{40,41} A number of substances have been used to activate, enhance growth or produce catalyst, such as activated carbon, graphite and metallic nitrates.

Given their popularity and impending market boom, CNT synthesis has experimented with a manifold of alternative

carbon sources amongst vegetable (camphor,^{42–48} turpentine oil,^{49,50} eucalyptus oil,⁵¹ palm oil⁵²), mineral (coal and coal gas^{53–68}), nano- (C60 fullerenes,^{69–71} CNTs^{72–76}) and petrochemical carbons (heavy oil residue,⁷⁷ tire powder,⁷⁸ carbon fibre,⁷⁹ carbon black,^{80,81} asphalt^{82,83}). With the exception of tire powder, while some might provide cheaper alternatives, none of them represent waste, having established markets and uses. The comparatively understudied SiONWs have not required alternative precursors from recycling or waste and are yet to be explored.

Two recent reports exist on the use of marketable (zeolite-free) PC for CNT synthesis. Kai Xu *et al.* were able to controllably produce single-wall (SW) and double-wall CNTs by arc discharge of an Fe-PC electrode in He and Ar atmospheres, respectively.⁸⁴ Crushed, sieved coke and Fe powders were mixed at a 1 : 2 weight ratio and filled into a hollowed out high-purity graphite anode. The high-purity graphite cathode was not the deposit collector in this case, but rather a metal wire net placed near the electrodes. The high-quality tubes presented narrow diameter distributions, more so for the SWCNTs. Abdullayeva *et al.* found that a coke rock, gasified at intermediate temperature zones in a tube furnace under He and H₂, produced CNTs on FeCl₂ thin films and powders, and Fe thin films.⁸⁵

FAU is not new to SiONW and CNT synthesis either, having served as a growth template for pore-controlled diameter distributions or catalyst arrangements. Reports of thermal disproportionation of SiO show the porous structure of FAU (cages and channels) defining the core diameter of resulting core/shell hybrid nanowires. Primarily, fine, crystalline Si cores sheathed with amorphous SiO₂ were found protruding from the zeolite pores. Beyond the templated growth, the FAU provided the silica in the shells. To a lesser extent, inverted (silica core) and side-by-side (half wire) nanowires were found at undisclosed locations in the sample.^{86,87} In CNT synthesis, zeolites can similarly provide catalytic decomposition,⁸⁸ catalyst support⁸⁹ and structural templates.⁹⁰ In fact, the thinnest free-standing SWCNTs (0.4 nm) were grown inside the channels of AFI zeolite (AlPO₄⁵⁻).⁹⁰

Given these existing synergies, the intention of this study is to provide a proof of concept for the feasibility of CNT and SiONW synthesis from FC3R by PLD, including intermittent parallels to cracking catalyst waste in general. The motivation is the revalorisation of this otherwise wasted material, addressing synthesis cost efficiency with cheaper precursors, beyond economies of scale and process optimisation. A FC3R rock from the state-owned La Teja refinery in Uruguay (operated by ANCAP), that in 2004 was producing 65 T of cracking catalyst waste a year,⁹¹ was thus used as the starting material for this work, constituting the carbon and silica precursor for CNT and SiONW synthesis by PLD. The produced nanostructures are technologically relevant 0-, 1- and 2-D nanomaterials: the expected SiONWs and SWCNTs, as well as onion-like carbons (OLCs), carbon nanodots (CNDs) and SiC nanostructures. Feasibility and proof are provided by a thorough morphological and chemical characterisation of the precursor (FC3R in 3.1) and resulting nanostructures (SiONWs in 3.2; SWCNTs in 3.3),

supported by a combination of electron microscopy, micro-milling and spectroscopic techniques.

2. Experimental

2.1 Thin film deposition

ca. 100 nm thin Ni films were DC magnetron-sputtered onto commercial SiO/Si wafers (500 ± 25 μm Si + 250 nm SiO₂) by physical vapour deposition (PVD). A base chamber pressure of 3.0 × 10⁻⁵ bar, an Ar pressure of 4.9 × 10⁻³ bar and a power of 103 W produced a sputtering rate of 14 nm min⁻¹.

2.2 Nanomaterial synthesis

Samples were synthesised by PLD. The carbon feedstock pellets (targets) were obtained by grinding a FC3R rock, faceting it into a manageable shape, appropriate for the PLD apparatus. The target was vaporised by a pulsed laser (solid state Nd:YAG Newport-SpectraPhysics Quanta-Ray 290) inside a tube furnace (Fig. 1) with the parameters in Table 1 and a total radiation time of 30 min.

2.3 Material characterisation

Scanning electron microscopy (SEM) (at 10–15 kV), focused ion beam (FIB) (Ga⁺ at 30 kV) milling and energy-dispersive X-ray spectroscopy (EDS) (10–20 kV) were carried out in a dual-beam

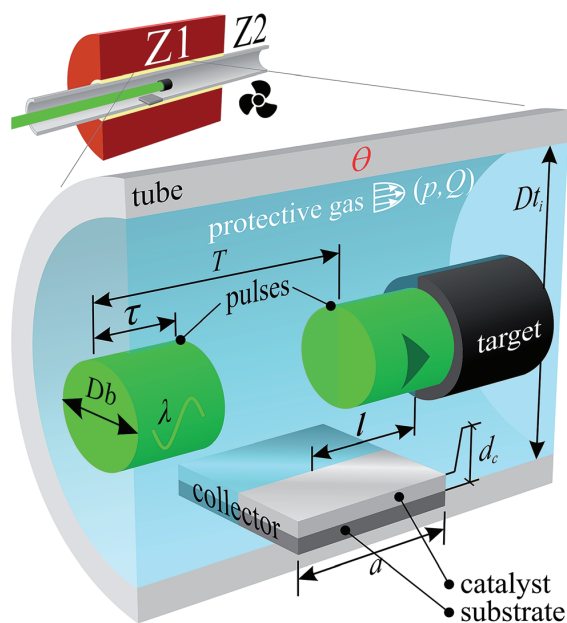


Fig. 1 Zone Z1 of PLD oven schematics (inset): tube (interior diameter D_t) furnace flooded with protective gas (pressure p , flow Q) at temperature Θ with incoming laser pulses (wavelength λ , pulse duration τ , frequency $1/T$, beam diameter D_b) impinging on a carbonaceous target and depositing on a square collector (thin-film catalyst (unrelated to cracking catalyst) (thickness d_c) on SiO₂/Si substrate (side a)) at a distance l from the laser impingement. Zone Z2 is the downstream, cooled tube furnace exit.

Table 1 PLD parameters as described in Fig. 1

Chamber	Quartz tube	$D_{\text{ti}} = 29 \text{ mm}$	$\Theta = 1200^\circ \text{C}$				
Atmosphere	Ar	Purity 6.0	$p = 1.3 \text{ bar}$	$Q = 3 \text{ sccm}$			
Radiation	$\lambda = 532 \text{ nm}$	$\tau = 10 \text{ ns}$	$1/T = 10 \text{ Hz}$	$D_b = 8 \text{ mm}$	$F = 1.59 \text{ J cm}^{-2}$	Vertical polarisation	
Target	Faceted FC3R rock		Composition: see results				
Collector	Catalyst: Ni	$d_c = 100 \text{ nm}$	Substrate: SiO_2/Si		$l \approx 30 \text{ mm}$	$a = 10 \text{ mm}$	

workstation (FEI Helios NanoLab 600) equipped with an EDS detector (EDAX Company). FIB cross-sections require the deposition of a Pt layer directly above the revealed cross-section to avoid curtaining effects.

Transmission electron microscopy (TEM; JEOL 2100F) was carried out at 200 kV on drop-casted dispersions in ethanol on a copper grid with a lacey carbon film (Gatan).

Raman spectra from 100 to 3500 cm^{-1} were obtained in a Raman spectrometer (Renishaw inVia) with 532 nm (2.33 eV) CW excitation through a 50 \times objective with a numerical aperture of 0.75, producing a 2.91 μm spot (calculated in ref. 92) on the sample. The power was set to 8.8 μW (0.13 kW m^{-2}), below a threshold of 2.65 kW cm^{-2} , beyond which modification was observed in SWCNTs.⁹² All Raman spectra were baseline-corrected with a straight line through the middle of the base noise over the complete range, if not specified otherwise, and peaks were fitted with Lorentzian functions.

X-ray diffraction (XRD) was performed (X'Pert MPD) with Cu K α radiation from a Cu source in a θ - θ geometry configuration. Spectra were acquired from 5–80° 2 θ with a step size of 0.026°.

2.4 Decoking

Decoked FC3R was obtained by grinding a sample into fine powder, then heating to 750 °C in air and mixing, thus thermally oxidising and removing the organic and volatile coke species without thermally decomposing the zeolite (at 793 °C).⁹³

3. Results and discussion

3.1 FC3R

The obtained raw FC3R rocks are agglomerates of coke-covered (shell) catalyst particles (core) which present an average core diameter and shell thickness of *ca.* 40 μm (Fig. 2a) and 2.65 μm (inset Fig. 2a). This would imply 69 vol% and 66 wt% catalyst ($d_{\text{FAU}} = 1.93 \text{ g cm}^{-3}$; $d_{\text{graphite}} = 2.16 \text{ g cm}^{-3}$ (ref. 95)). However, decoking revealed 57 wt% catalyst, indicating excess interparticle carbon.

An elemental EDS analysis reveals C, Al, Si, O and traces of S and Na. Colour-mapped scans for each element (Fig. 2b) assign the C to the coke shells and Al, Si, O to the catalyst. A global spectrum of the area shows predominant C (Fig. 2c) due to a majority of shells and EDS penetration depth (2 μm , at 10 kV, below shell thickness), however local spectra of the coke and the catalyst show distinct species (Fig. 2d), with Na attributed to the latter. Na ions are used to balance the alumina tetrahedra in the zeolite during its synthesis.⁹⁶

Beyond elemental analysis, XRD of the FC3R produced unintelligible signal convolution due to its complex

composition. Isolation of the carbonaceous species was not possible, yet, it is expected to contain mainly aromatic carbon, namely, two to five 5/6-membered aromatic carbon rings, from $\text{C}_{12}\text{H}_{10}$ to $\text{C}_{18}\text{H}_{12}$.⁸⁵ On the other hand, X-ray powder diffraction of the isolated catalyst (decoked FC3R) (Fig. 3b) was successful, and contrasted with a selection of simulated zeolite XRD powder patterns^{3,97} and experimental alumina⁹⁸ and silica⁹⁹ patterns. Two groups of distinct reflections, narrow and well-defined vs. broad, clearly evidence the convoluted signal of two discrete species in the FC3R, unequivocally identified as sodiated zeolite Y (FAU NaY: $[\text{Na}_{28.8}\text{Ca}_{14.4}(\text{H}_2\text{O})_{263}][\text{Si}_{134.4}\text{Al}_{57.6}\text{O}_{384}]^3$ (Fig. 3a) and gamma alumina ($\gamma\text{-Al}_2\text{O}_3$) (Fig. 3c, right), respectively. The latter is present as a baseline to the former, an overlay of both. The Scherrer equation,¹⁰⁰ based on these peak geometries, qualitatively attributes much smaller crystallites to the alumina in contrast to the longer-range order of FAU. We can conclude that this alumina polymorph is not that of the FAU aluminate tetrahedra (AlO_4) and likely stems from the kaolinite or the matrix, components of fluid catalytic cracking (FCC) catalysts. Silica could only be marginally attributed to four unidentified peaks in the FC3R (Fig. 3c, left). Nonetheless, the presumed FAU and aluminosilicates could be

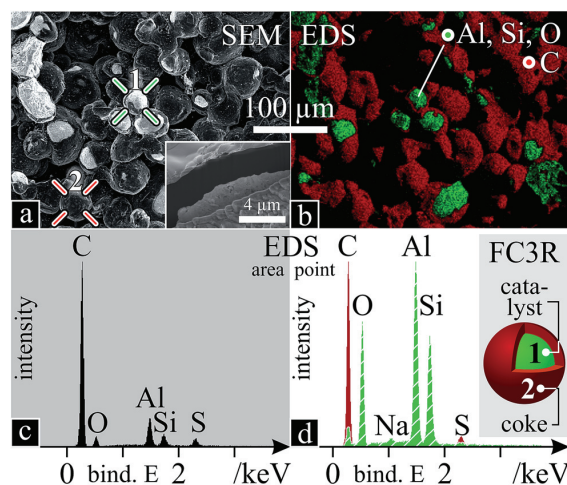


Fig. 2 FC3R morphology and chemistry: (a) fracture SEM micrograph with points 1 (catalyst core; green crosshair) and 2 (coke shell; red crosshair) and close-up of FIB cross-section (inset); (b) EDS colour map of Al, Si, O and C; (c) EDS scan of area in "a"; (d) EDS spectra of points 1 (green, striped) and 2 (red) in "a", with a schema of a FC3R particle and what points 1 and 2 correspond to. S was equally present in both cores and shells of the particles. All EDS data refer to K-shell electrons. The dark patches in "b" are out of plain.

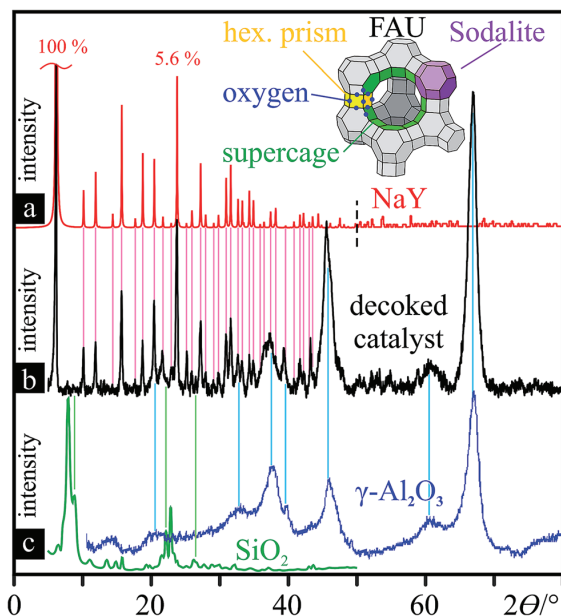


Fig. 3 Decoked catalyst powder characterisation: XRD patterns with reference lines for peak assignment. (a) simulated XRD powder pattern of NaY FAU from 0–50° (ref. 3) and from 50–80° (ref. 97) (both sections normalised to the strongest reflection at 6.19°); 3-D structure of simplified FAU unit cell (Si/Al vertices), composed of linked sodalite cells. (b) XRD powder pattern of the decoked catalyst. (c) XRD pattern of zeolite (ITQ-39)-derived SiO₂ (left, green)⁹⁹ and commercial γ -Al₂O₃ (blue, right)⁹⁸ (both baseline-corrected).

confirmed with sufficient detail and certainty for the framework of this study, indicating an industry standard FCC catalyst.

The phase chemistry of the coke deposit was provided by Raman spectroscopy (Fig. 4). The signal of the decoked catalyst

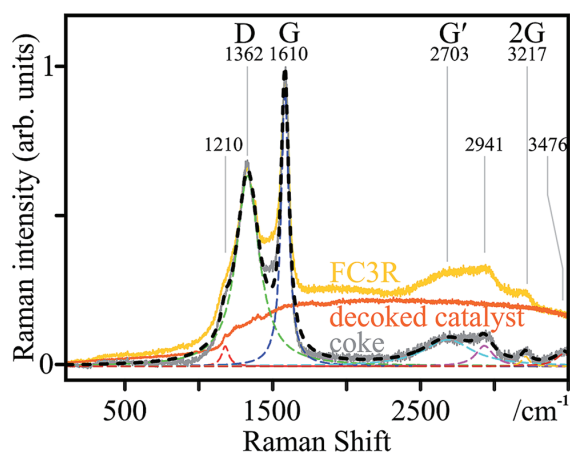


Fig. 4 Coke characterisation: Raman spectrum (black) of the coke constructed ($r^2 > 0.98$) from the deconvoluted peaks of the coke spectrum (grey), in turn resulting from FC3R (raw data; yellow) minus the decoked catalyst baseline (orange); marked peaks D, G, and their overtones G' and 2G, and corresponding frequencies. Fits are dashed.

powder was subtracted from that of the FC3R to reveal an approximate spectrum of the coke (not free of catalyst contributions with parasite peaks). The presumed graphitic nature of the coke shell was confirmed with characteristic D and G modes, and their overtones G' and 2G.¹⁰¹ The thin peak width of G indicates relatively ordered graphite with few defects,¹⁰² confirmed by a defect density I_D/I_G of 0.65.¹⁰³ However, the relatively intense and wide D mode attests to the disordered carbon and numerous aromatic species present,¹⁰⁴ as can be expected from a by-product of petroleum refining. This is supported by a low G' intensity and very low $I_{G'}/I_D$ ratio (0.15), indicating low purity.¹⁰³

3.2 SiONWs

Post synthesis, the thin film sample from Z1 (Fig. 1) appeared to be lacking any deposition or Ni film. In the SEM, except for a few protruding, torus-shaped craters, the entire sample surface was covered in a dense, regular layer of nanowires (Fig. 5a), found to be optically transparent. Judging from their shape, the craters might be due to larger target debris, projected at the beginning of the laser irradiation or impurities on the Ni surface, already present before irradiation. Upon closer inspection (of either feature) (Fig. 5b), arrangements consisting of radially-grown nanowires appear, which, when observed with primary

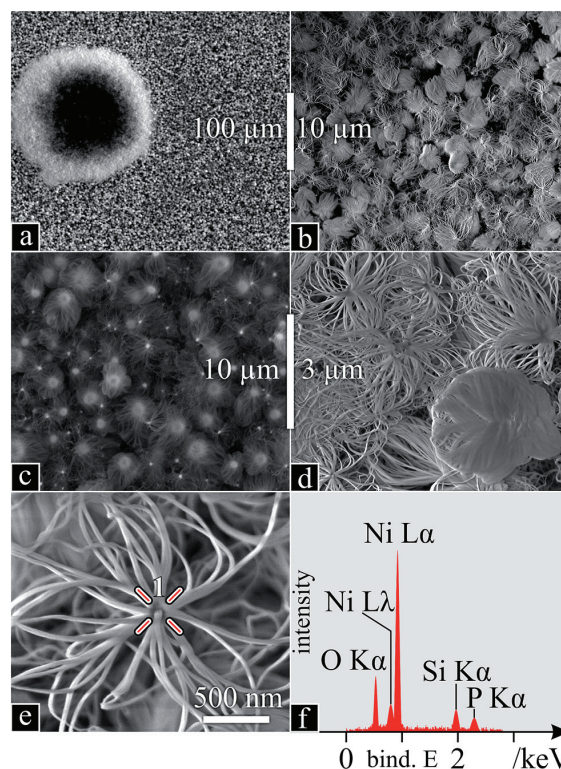


Fig. 5 SiONW characterisation I: (a–e) SEM micrographs (high-energy secondary electrons in (c)) with increasing magnification; (f) EDS spectrum of the growth nucleus (point 1 in e).

electrons, reveal particles at their core (Fig. 5c). Higher magnification (Fig. 5d and e) confirms this radial configuration of densely packed nanowires around particles, of which a local EDS spectrum reveals a composition of predominant Ni, along with O, Si and P (Fig. 5f): a first indication of Ni-particle-bound SiONWs. These were identical to those in and around the craters.

The bright heterostructures seen by SEM appear as transparent nanowires protruding from opaque particles using TEM (Fig. 6a). High magnification of the wires (Fig. 6b) exposed an amorphous structure confirmed by the absence of diffraction patterns (inset). A zoom on one nanowire/core formation (Fig. 6c) was used for elemental analysis: Ni is only found at the core (Fig. 6d), where Si (Fig. 6e) and O (Fig. 6f) are also present, yet to a greater extent at the surface and in the wires. The excess O, deduced from a corresponding Si/O atomic ratio of 1 : 3.5, possibly indicates Ni oxide in the core. Also identified were low amounts of P, in the core, and generally dispersed traces of Al, not corresponding to any particular structural feature or location.

These arrangements with catalyst cores suggest dewetting of the Ni thin film, a common occurrence in supported nanowire/tube synthesis, by which a continuous thin film at or near its melting point ruptures and coagulates into beads, due to Plateau-Rayleigh instability and surface tension. Although 1200

°C is still well below the melting point of Ni (1450 °C), several factors can account for this phenomenon: (1) low dimensionality is known to drastically reduce melting points, placing that of a 100 nm Ni film at roughly 1200 °C;¹⁰⁵ (2) the highly energetic species landing on the Ni, produced in the ablation plume (above 3500 °C (ref. 106)), would further provide the necessary energy; (3) the eutectic temperature of a formed alloy, *e.g.* the Ni–Si system, which has a number of eutectic plateaus between 22 and 56 at% Si, at temperatures as low as 800 °C (up to 1215 °C),¹⁰⁷ all of which are allowed systems through Si diffusion. Any combination of (1), (2) and (3) would drastically reduce the melting temperature of the catalyst and initiate or maintain liquid metal-alloy droplets catalysing nanowire growth.

To explore dewetting, layer morphology, growth and possibly the early stages thereof, a deeper inspection of the SiONW layer down to the substrate was necessary. Since this layer was densely packed, a FIB cross-section provided the insight (Fig. 7). Although the Pt layer (see Experimental) presumably compressed the SiONW layer, a $\sim 6\text{--}7\ \mu\text{m}$ layer of SiONWs (around Ni cores) can be seen atop an intact SiO thin film on Si, with no trace of the Ni layer. The nanowires seem to be thinner near the substrate. Furthermore, although Si- and SiONWs are often reported to coexist, growing with or from each other,^{86,87,108,109} no SiNWs were observed. Several conclusions can be drawn: (1) the existing SiO film did not intervene in the nanowire growth; (2) only SiONWs were grown; (3) the Ni layer was completely consumed into beads, and (4) nanowire growth in the lowest regions was quenched due to lacking precursors.

The vapour-liquid-solid (VLS) mechanism would imply an initial downwards growth of the nanowires, elevating the first seeds of growth away from the substrate, eventually covering the space below. The silica, being deposited on the outer surface, would feed the continued growth of thick and dense nanowire bundles in the uppermost regions. However, the resulting limited availability of silica and Ni in the lower regions of the layer would result in smaller wires nucleating from small amounts of leftover metal catalyst, which was finally exhausted in the early stages of growth.

This complex SiONW precursor, FC3R, offers many conjectures as to the growth mechanism. Aside from the common

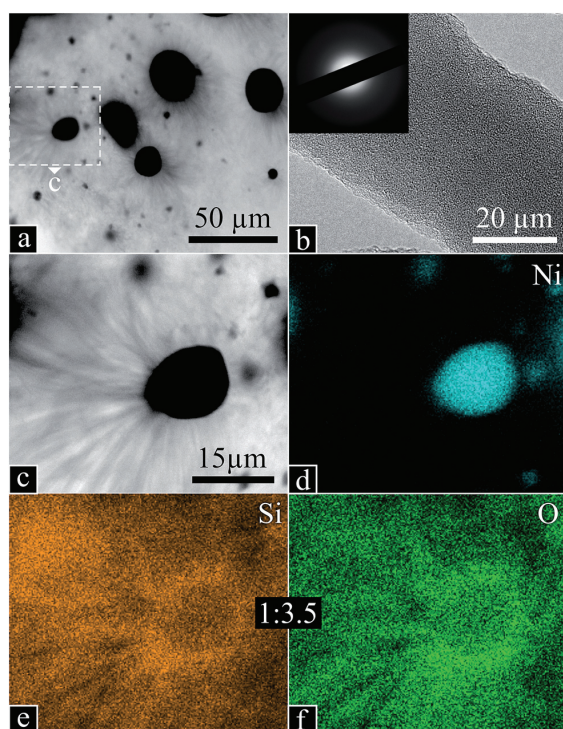


Fig. 6 SiONW characterisation II: TEM micrographs of (a) Ni particles with radial SiONWs; (b) high magnification of a SiONW with diffraction inset; (c) close up from “a” of one Ni particle with SiONWs; (d–f) EDS scans of “c” for Ni, Si and O with 1 : 3.5 Si to O atomic ratio.

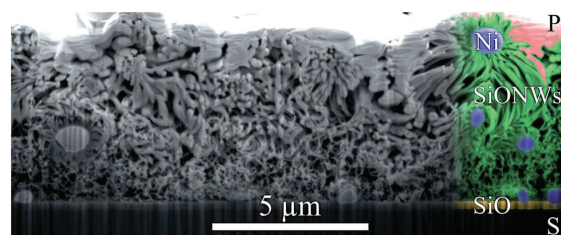


Fig. 7 SiONW layer: SEM micrograph of a FIB cross-section, along the sample surface normal. Observed are (from top to bottom): an irregular layer of deposited platinum (partially sunken in), a $\sim 6\text{--}7\ \mu\text{m}$ layer of SiONWs around Ni cores, an intact 250 nm SiO thin film (as received), and the underlying Si. The right of the image is in false colour, to better identify each species: pink Pt, green nanowires, blue cores and yellow SiO₂ thin film. The vertical lines are an artefact of the FIB milling.

vapour/solid-liquid-solid (SLS) mechanisms involving Si and O, certain reports present carbon as a key element in their SiONW growth, through mechanisms fitting the conditions described here. Upstream graphite can be gasified by a fed oxygen flow to CO₂, reacting with Si (s) to produce SiO (g), which upon reaction with O₂ (g) to SiO₂ (s) in Si, aggregates into nanowires.¹¹⁰ Similarly, a CH₄ feed can be decomposed by an Fe catalyst, freeing C to dissolve in SiO₂ nanoparticles, forming SiO and CO vapours; CO reduction by the Fe releases O₂ which diffuses with SiO in the nanoparticles to nucleate at their surface as SiONWs.¹¹¹ In either case, the carbon was key and acted as a vehicle for the oxygen, to oxidise Si and SiO.

Summarising, the liquid catalyst droplets become the support for the described VLS growth, prior to or upon laser irradiation of the target. At this point, the reactants from the vapour phase are absorbed, alloyed and solved until supersaturation and crystallisation at the surface. Each nickel particle catalyses tens to thousands of nanowires depending on its size, maintained as long as the eutectic temperature is not underrun. Supposing the temperature of the catalyst is well above the chamber temperature of 1200 °C, due to the incoming vapour, all eutectic Ni-Si systems would be allowed.

As to the alumina present in the target, it appears to not play a role in the synthesis. Indeed, FAU thermally decomposes at 793 °C,⁹³ freeing up mainly silica and alumina. Their respective melting and boiling temperatures of 1713 °C & 2950 °C (ref. 112) vs. 2072 °C & 2977 °C (ref. 113) would indicate a tendency to preferentially release the silica into the laser plume. Furthermore, the heavier alumina (4.0–4.1 vs. 2.2–2.6 g cm⁻³) would have a shorter flight path from the target and perhaps land outside of the collector. Finally, FAUs X and Y and other variations differ mainly in the Si/Al ratio. It is possible that this was a low-Al FAU and that the kaolinite γ -Al₂O₃ underwent different ejection/vaporisation mechanisms, incompatible with nanostructure self-assembly. Si, found in all the catalyst components (FAU, binder, kaolinite), was in major surplus with respect to Al (kaolinite and minor component of FAU). Although bottom-up synthesis of alumina nanowires is known to occur at the reactor temperature (1200 °C) by PVD¹¹⁴ and CVD,¹¹⁵ no such reports exist for PLD and none were observed here.

3.3 SWCNTs

Neither SEM, TEM nor EDS analyses indicated CNTs in samples from zone Z1. SEM EDS spectra of what appeared to be thinner nanowires/tubes indicated low amounts of carbon, yet within uncertain peak intensities. However, Raman spectra from certain spots of the sample (Fig. 8-Z1) revealed spectra strikingly similar to that of MWCNTs, with much thinner peaks, a high D-mode intensity, a slightly lower I_D/I_G of 0.61 and, most importantly, a very intense G' and thus a much lower $I_{G'}/I_D$ of 0.92, common in MWCNTs. Additionally, the refined Raman modes of said spectrum attest to the loss of amorphous carbon, aromatic species and functional groups, previously present in the coke.

In zone Z2 of the PLD apparatus, a black, powdery soot condensed on the cold tube exit. These samples produced Raman spectra (Fig. 8-Z2) indicative of graphitic species, including

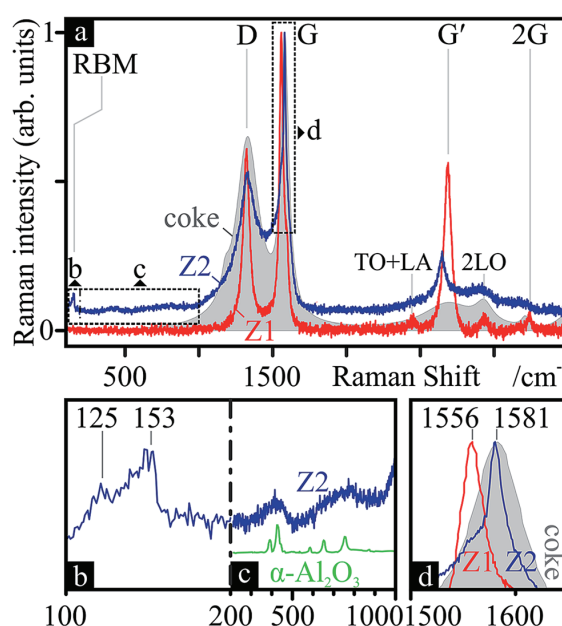


Fig. 8 Nanocarbon chemistry: Raman spectra (a) of certain areas on the SiONW sample from zone Z1 (Z1, red) and of the black soot powder from zone Z2 (Z2, blue). The underlayed Raman spectrum of the initial coke from Fig. 4 (grey, filled area) is added for comparison. The RBM (b), alumina (c) (contrasted with ref. 124 in green) and G (d) regions are zoomed-in for further detail. Modes and frequencies are marked.

SWCNTs: a clear RBM (Fig. 8b) between 125 and 153 cm⁻¹, revealing tubes *ca.* 1.5–1.8 nm in diameter,¹¹⁶ and G-splitting (Fig. 8d), with disparate G⁺ and G⁻ intensities, suggesting semi-conducting SWCNTs.¹¹⁷ The position of the G band (1581 cm⁻¹) suggests a more ordered form of sp² carbon than that found in Z1 (1561 cm⁻¹).¹¹⁸ Furthermore, the Raman features between RBM and D (Fig. 8c) resemble that of α -Al₂O₃. This $\gamma \rightarrow (\delta \rightarrow \theta \rightarrow) \alpha$ transformation is to be expected, since the former is a metastable phase and only α remains at 1100 °C.¹¹⁹

EDS spectra (Fig. 9b) reveal the same components as the nanowire samples, C, O, Al and Si, in order of atomic abundance. Although C is predominant, the missing Al in zone Z1 clearly made its way here, accounting for a quarter of the atomic species. Indeed, the bright spots in Fig. 9a appear to be alumina particles (Fig. 9c). Apart from these visible spheres, Si, Al and O are present throughout the sample (Fig. 9b). Closer up, branched networks of nanoparticulate material appear (Fig. 9d), typical for CNT soot.

The latter formations, upon observation in TEM (Fig. 10), reveal superimposed species. SiC nanoparticles (Fig. 10b) and -flakes (Fig. 10c), encapsulated with 2–3 layers of sp² carbon display a characteristic honeycomb pattern with a fringe lattice spacing of 0.28 nm (confirmed by the inset fast Fourier transform (FFT)).¹²⁰ OLCs (Fig. 10d) and CNDs (Fig. 10e) are also present. Most importantly, SWCNTs (Fig. 10e) are readily found, as an underlying network and protruding from the edges of CNDs/SiC, with diameters >2 nm, undetectable by Raman.¹²¹

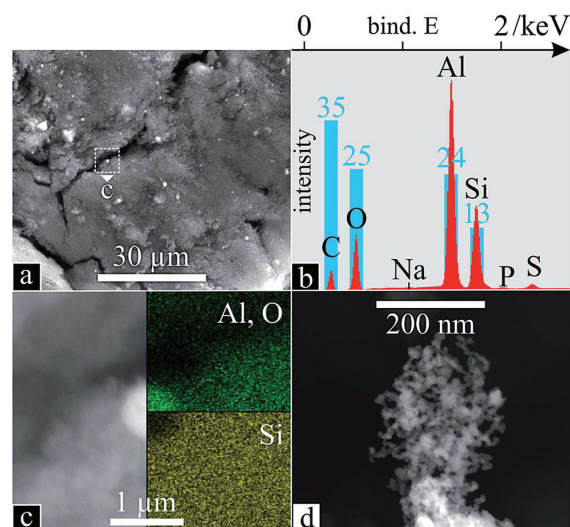


Fig. 9 Nanocarbon soot morphology and chemistry: SEM (a) of powder deposit from zone Z2 in the PLD apparatus (Fig. 1) with corresponding EDS scan (b); SEM with inset EDS scans of an alumina particle (c); higher magnification of branched network (d).

Conversely, those observed by Raman, 1.5–1.8 nm ($125\text{--}153\text{ cm}^{-1}$),¹¹⁶ could not be found by TEM, likely hidden amongst the other species present. Although MWCNTs with inner-most tubes below 2 nm are known to present misleading RBM^{121,122} and G-splitting¹²¹ Raman features, none could be observed.

This CNT growth follows the mechanism from whence it was discovered: SLS-condensation on the downstream, cooled furnace exit.²⁷ Though instead of a water-cooled copper collector, the air-cooled quartz tube served as condensation site. Specifically, gaseous carbon was dissolved in liquid SiC and C nanoparticles to saturation, followed by crystallisation at the surface. This precipitation of graphitic carbon at the surface encapsulates the nanoparticle in sp^2 C. Through an instability in the sheet or partial dissolution of fullerenes, critical nuclei protrude outwards into CNTs.³⁸ Failure to produce outwards growth, closes the carbon shell resulting in the observed encapsulated SiC, CNDs or OLCs.

Although the 47% void fraction of FAU¹²³ is actually conducive to enhanced CNT synthesis and higher yields by PLD due to porosity,²⁶ these pores likely contain oxygen. This presents competing mechanisms of amorphous carbon removal towards increased CNT purity and the removal of carbonaceous species before it can be added to the CNT. Still, contrary to graphite ablation, where single atoms are added to a growing CNT, larger aromatic species present in the coke can be directly incorporated.³⁹ Finally, no alumina nanoparticulate could be found, crystalline or other.

The benefits of the low cost and availability of FC3R outweigh the complex heterogeneous composition of the coke, with further research necessary to fine-tune the selectivity, quality and yield of the numerous valuable products. The advantages of PLD with respect to its plume dynamics could be

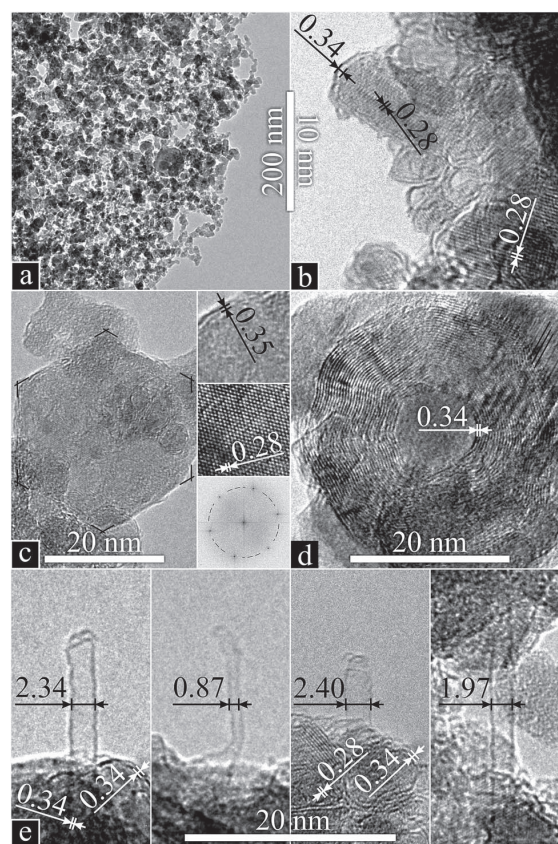


Fig. 10 Nanocarbon soot (a) species: TEM micrographs with corresponding fringe lattice spacings of sp^2 -carbon-encapsulated SiC nanocrystals (b), a nanoflake (insets: zoomed-in edge and lattice; FFT) (c), an OLC (d) and SWCNTs (e) with encapsulated SiC or CNDs at their base.

combined with the scalability of CVD, tailoring CNT seeds by the former with continued growth by the latter. Alternating functionally-graded CNT layers could be achieved by changing the pulse parameters.

The worlds refined hydrocarbons are chiefly produced by FCC and HP (48% and 19%).¹ Extending these findings to spent cracking catalyst waste in general, the little-to-no silica precludes the use of spent HP catalyst for SiONWs; and although the metal content might be pertinent to SWCNT catalysis, the low amounts of carbon (due to a reduced coking tendency) and the absence of any tendency for alumina to self-assemble in an oven-laser apparatus, would render HPCR a mere source of alumina nanoparticulate with marginal SWCNT yield, at best. Thus, FC3R stands out as a candidate for revalorisation as proposed here.

4. Conclusions

The waste, taken directly from a refinery, was identified as high-carbon petrochemical cracking catalyst waste, FC3R, consisting

of petroleum coke-covered (predominantly sp^2) zeolite Y and γ - Al_2O_3 . The resulting PLD nanospecies were produced in two distinct zones of a simple lab-scale oven-laser setup, from untreated FC3R. On samples directly opposite the FC3R target (zone Z1), the reflected plume produced an optically transparent layer of amorphous SiONWs, consistent with a metal-catalysed VLS mechanism, as densely packed, radial bundles around Ni particle cores at their base. At the downstream, cooled tube-furnace exit (zone Z2), condensation produced SWCNTs (and other nanocarbons: sp^2 -encapsulated SiC nanocrystals and -flakes, OLCs and CNDs), consistent with a nano-carbon-catalysed SLS self-assembly. Our hypothesis and concept are thus proven, constituting (1) the first use of a waste feedstock for SiONW synthesis, (2) one of very few such attempts for CNTs, and (3) the first (high-tech) outlet for FC3R and catalyst coke in general.

Silicon is the most eminent material in electronics. From bulk to thin films, its semiconducting properties have permeated technology, until recently, unchallenged. Enter wires, tubes and dots of various materials. Thanks to their size and/or aspect ratio, these low-dimensional nanostructures are now competing for their share in future technologies. Carbon, from the same group in the periodic table, is possibly the strongest contender. Respectively the 2nd and 15th most abundant elements in earth's crust, neither Si nor C are scarce nor are they conflict materials. But as high-tech nanomaterials continue to infiltrate technology, so does the need to reduce, reuse and recycle ('the three R's'). Although a petrochemical precursor may not qualify as *green*, its use does address the third R of a currently otherwise wasted and contaminant resource, mitigating its environmental impact. Moreover, if recycled materials are of particular relevance since they avoid waste and its disposal, then indeed transforming petroleum cracking waste into 0- and 1-D nanostructures of great technological value such as SWCNTs and SiONWs would fall into the more coveted end of the recycling spectrum, *upcycling*. This extreme revalorisation of abundant waste could fuel research and applications in mesoscopic physics, optical fibres, Si- and C-based nano- and microelectronic devices and composites.

Acknowledgements

This work was supported by the SUMA2 Network Project, 7th Framework Program of the European Commission (IRSES Project No. 318903), and the CREATE-Network Project, Horizon 2020 Program of the European Commission (RISE Project No. 644013). VP and MZ thank Prof. Eduard Arzt (INM) for his continuing support. AB was supported as part of the iSTAR Scholars Program of Drexel University.

Notes and references

- 1 E. T. C. Vogt and B. M. Weckhuysen, *Chem. Soc. Rev.*, 2015, **44**, 7342–7370.
- 2 R. Sadeghbeigi, *Fluid Catalytic Cracking Handbook: Design, Operation and Troubleshooting of FCC Facilities*, Gulf Professional Publishing, 2nd edn, 2000.
- 3 M. M. J. Treacy and J. B. Higgins, *Collection of simulated XRD powder patterns for zeolites*, Elsevier, 1986, vol. 21.
- 4 D. L. Trimm, *Appl. Catal.*, A, 2001, **212**, 153–160.
- 5 A. L. C. da Cunha, M. S. Lemos, S. Meth, J. P. Gonçalves and J. Dweck, *J. Therm. Anal. Calorim.*, 2011, **106**, 805–809.
- 6 N. Su, H.-Y. Fang, Z.-H. Chen and F.-S. Liu, *Cem. Concr. Res.*, 2000, **30**, 1773–1783.
- 7 E. Furimsky, *Catal. Today*, 1996, **30**, 223–286.
- 8 U.S. Energy Information Administration, *Supply and Disposition – Petroleum Coke*, 2015.
- 9 M. A. Diez, R. Alvarez and C. Barriocanal, *Int. J. Coal Geol.*, 2002, **50**, 389–412.
- 10 R. A. Graves Jr and W. G. Witte, *Flight-test analysis of Apollo heat-shield material using the Pacemaker vehicle system*, Langley Research Center, Washington DC, 1968.
- 11 European Commission, *Integr. Pollut. Prev. Control*, 2003, p. 518.
- 12 E. C. I. Council, *FCC equilibrium catalyst (including FCC catalyst fines) finds safe reuse/rework outlets in Europe*, 2006.
- 13 M. Diaz, *Hazardous Waste Management System; Identification and Listing of Hazardous Waste: Spent Catalysts from Dual-Purpose Petroleum Hydroprocessing Reactors*, Washington DC, 2002, vol. 67.
- 14 Environmental and forestry Statistics, *Guidance on classification of waste according to EWC-stat categories*, 2010, vol. 2150/2002.
- 15 M. Marafi and A. Stanislaus, *Resour., Conserv. Recycl.*, 2008, **53**, 1–26.
- 16 R. Schmitt, *Oil Gas J.*, 1991, **89**, 101–102.
- 17 J. Monzó Balbuena, J. Payá Bernabeu and V. Rosado Borrachero, *Sp. Pat.*, ES 2 144 928, 1997.
- 18 E. Restrepo, L. Arbeláez, P. Caballero, E. López, F. Vargas and G. Duarte, *Elabor. refract. Al_2O_3 - SiO_2 a partir residuos catalíticos provenientes la Ind. petroquímica*, 2014, pp. 1–10.
- 19 L. P. Garcia, R. T. da Cruz and S. R. Braganca, *Proc. Inst. Mech. Eng., Part L*, 2012, **226**, 286–292.
- 20 A. Escardino, J. L. Amoros, A. Moreno and E. Sanchez, *Waste Manage. Res.*, 1995, **13**, 569–578.
- 21 K.-L. Lin, H.-H. Wu, S.-J. Chao, A. Cheng and C.-L. Hwang, *Environ. Prog. Sustainable Energy*, 2013, **32**, 94–98.
- 22 J. Monzó, J. Payá, M. V. Borrachero, S. Velásquez, L. Soriano, P. Serna and J. Rigueira, in *International RILEM Conference on the Use of Recycled Materials in Buildings and Structures*, 2004.
- 23 A. Guerrero, J. Puerta, F. Gomez and F. Blanco, *Phys. Scr.*, 2008, **T131**, 014007.
- 24 N. Nagaraju, A. Fonseca, Z. Konya and J. B. Nagy, *J. Mol. Catal. A: Chem.*, 2002, **181**, 57–62.
- 25 K.-H. Lee, K. Baik, J.-S. Bang, S.-W. Lee and W. Sigmund, *Solid State Commun.*, 2004, **129**, 583–587.
- 26 M. Yudasaka, M. Zhang and S. Iijima, *Chem. Phys. Lett.*, 2000, 6–7.
- 27 T. Guo, P. Nikolaev and A. Thess, *Chem. Phys. Lett.*, 1995, **243**, 49–54.
- 28 H. Zhu, L. Ci, C. Xu, J. Liang and D. Wu, *Diamond Relat. Mater.*, 2002, **11**, 1349–1352.

- 29 D. P. Yu, Q. L. Hang, Y. Ding, H. Z. Zhang, Z. G. Bai, J. J. Wang, Y. H. Zou, W. Qian, G. C. Xiong and S. Q. Feng, *Appl. Phys. Lett.*, 1998, **73**, 3076–3078.
- 30 J. Chen, X. Li, X. Wu, J. T. Pierce, N. Fahrudin, M. Wu and J. X. Zhao, *Langmuir*, 2014, **30**, 9514–9523.
- 31 E. Huey, S. Krishnan, S. K. Arya, A. Dey and S. Bhansali, *Sens. Actuators, B*, 2012, **175**, 29–33.
- 32 S. Y. Khmel, in *EU PVSEC*, 2013, pp. 395–398.
- 33 N. S. Ramgir, P. K. Sekhar, A. Zajac, L. Lee, T. Zhukov and S. Bhansali, *Sens. Lett.*, 2007, **5**, 608–611.
- 34 R. G. Elliman, A. R. Wilkinson, T. H. Kim, P. K. Sekhar and S. Bhansali, *J. Appl. Phys.*, 2008, **103**, 104304.
- 35 G. Brambilla and D. N. Payne, *Nano Lett.*, 2009, **9**, 831–835.
- 36 T. Guo, P. Nikolaev, A. G. Rinzler, D. Tomanek, D. T. Colbert and R. E. Smalley, *J. Phys. Chem.*, 1995, **99**, 10694–10697.
- 37 E. Munoz, W. Maser and A. Benito, *Synth. Met.*, 1999, **103**, 2490–2491.
- 38 A. Gorbunoff and O. Jost, in *Pulsed Laser Deposition of Thin Films*, 2007, pp. 613–632.
- 39 L. Pang, L. Prochazka and R. Quezada, *Fuel and Energy Abstracts*, 1995, **36**, 189.
- 40 G. Hong, Y. Chen, P. Li and J. Zhang, *Carbon*, 2012, **50**, 2067–2082.
- 41 D. Carole, A. Brioude, A. Pillonnet, J. Lorenzzi, O. Kim-Hak, F. Cauwet and G. Ferro, *J. Cryst. Growth*, 2011, **320**, 55–62.
- 42 M. Sharon, W. K. Hsu, H. W. Kroto, D. R. M. Walton, A. Kawahara, T. Ishihara and Y. Takita, *J. Power Sources*, 2002, **104**, 148–153.
- 43 M. Kumar and Y. Ando, *Diamond Relat. Mater.*, 2003, **12**, 998–1002.
- 44 M. Kumar and Y. Ando, *Diamond Relat. Mater.*, 2003, **12**, 1845–1850.
- 45 M. Kumar and Y. Ando, *Chem. Phys. Lett.*, 2003, **374**, 521–526.
- 46 M. Kumar and Y. Ando, *Carbon*, 2005, **43**, 533–540.
- 47 R. J. Andrews, C. F. Smith and A. J. Alexander, *Carbon*, 2006, **44**, 341–347.
- 48 M. Kumar, T. Okazaki, M. Hiramatsu and Y. Ando, *Carbon*, 2007, **45**, 1899–1904.
- 49 R. A. Afre, T. Soga, T. Jimbo, M. Kumar, Y. Ando, M. Sharon, P. R. Somani and M. Umeno, *Microporous Mesoporous Mater.*, 2006, **96**, 184–190.
- 50 P. Ghosh, T. Soga, R. A. Afre and T. Jimbo, *J. Alloys Compd.*, 2008, **462**, 289–293.
- 51 P. Ghosh, R. A. Afre, T. Soga and T. Jimbo, *Mater. Lett.*, 2007, **61**, 3768–3770.
- 52 A. B. Suriani, R. M. Nor and M. Rusop, *J. Ceram. Soc. Jpn.*, 2010, **118**, 963–968.
- 53 L. Pang and M. Wilson, *Energy Fuels*, 1993, 239–240.
- 54 K. Williams, M. Tachibana and J. Allen, *Chem. Phys.*, 1999, 31–37.
- 55 M. Wilson, H. Patney and J. Kalman, *Fuel*, 2002, **81**, 5–14.
- 56 J.-S. Qiu, F. Zhang, Y. Zhou, H.-M. Han, D.-S. Hu, S. C. Tsang and P. J. F. Harris, *Fuel*, 2002, **81**, 1509–1514.
- 57 Y. F. Li, J. S. Qiu, Z. B. Zhao, T. H. Wang, Y. P. Wang and W. Li, *Chem. Phys. Lett.*, 2002, **366**, 544–550.
- 58 J. Qiu, Y. Li, Y. Wang, T. Wang, Z. Zhao and Y. Zhou, *Carbon*, 2003, **41**, 2170–2173.
- 59 J. Yu, J. Lucas, V. Strezov and T. Wall, *Fuel*, 2003, **82**, 2025–2032.
- 60 Y. J. Tian, Y. L. Zhang, Q. Yü, X. Z. Wang, Z. Hu, Y. F. Zhang and K. C. Xie, *Catal. Today*, 2004, **89**, 233–236.
- 61 J. Qiu, Y. An, Z. Zhao, Y. Li and Y. Zhou, *Fuel Process. Technol.*, 2004, **85**, 913–920.
- 62 J. Qiu, Y. Li, Y. Wang and W. Li, *Fuel Process. Technol.*, 2004, **85**, 1663–1670.
- 63 Y. Tian, Y. Zhang, B. Wang, W. Ji, Y. Zhang and K. Xie, *Carbon*, 2004, **42**, 2597–2601.
- 64 Z. Wang, Z. Zhao and J. Qiu, *Carbon*, 2006, **44**, 1321–1324.
- 65 Z. Wang, Z. Zhao and J. Qiu, *Carbon*, 2006, **44**, 1845–1847.
- 66 J. Qiu, Q. Li, Z. Wang, Y. Sun and H. Zhang, *Carbon*, 2006, **44**, 2565–2568.
- 67 R. B. Mathur, C. Lal and D. K. Sharma, *Energy Sources, Part A*, 2007, **29**, 21–27.
- 68 J. Qiu, Z. Wang, Z. Zhao and T. Wang, *Fuel*, 2007, **86**, 282–286.
- 69 Y. Zhang and S. Iijima, *Appl. Phys. Lett.*, 1999, **75**, 3087.
- 70 V. Lavrentiev, H. Abe and S. Yamamoto, *Phys. B*, 2002, **323**, 303–305.
- 71 J. Qiu, G. Chen, Z. Li and Z. Zhao, *Carbon*, 2010, **48**, 1312–1315.
- 72 M. Zhang, M. Yudasaka and S. Iijima, *Chem. Phys. Lett.*, 2001, **336**, 196–200.
- 73 D. B. Geohegan, H. Schittenhelm, X. Fan, S. J. Pennycook, A. A. Paretzky, M. A. Guillorn, D. A. Blom and D. C. Joy, *Appl. Phys. Lett.*, 2001, **78**, 3307.
- 74 A. A. Stramel, M. C. Gupta, H. R. Lee, J. Yu and W. C. Edwards, *Optic. Laser. Eng.*, 2010, **48**, 1291–1295.
- 75 L. Li, F. Li, C. Liu and H.-M. Cheng, *Carbon*, 2005, **43**, 623–629.
- 76 F. Bonaccorso, C. Bongiorno, B. Fazio, P. G. Gucciardi, O. M. Maragò, A. Morone and C. Spinella, *Appl. Surf. Sci.*, 2007, **254**, 1260–1263.
- 77 Y. Li, H. Wang, G. Wang and J. Gao, *Chem. Eng. J.*, 2012, **211–212**, 255–259.
- 78 L. E. Murr, D. K. Brown, E. V. Esquivel, T. D. Ponda, F. Martinez and A. Virgen, *Mater. Charact.*, 2005, **55**, 371–377.
- 79 H. M. Yusoff, R. Shastri, T. Querrioux and J. Abrahamson, *Curr. Appl. Phys.*, 2006, **6**, 422–426.
- 80 D. Buchholz, S. Doherty and R. Chang, *Carbon*, 2003, **41**, 1625–1634.
- 81 K. S. Kim, G. Cota-Sanchez, C. T. Kingston, M. Imris, B. Simard and G. Soucy, *J. Phys. D: Appl. Phys.*, 2007, **40**, 2375–2387.
- 82 K. Xu, Y. Li, C. Xu, J. Gao, H. Liu, H. Yang and P. Richard, *Chem. Eng. J.*, 2013, **225**, 210–215.
- 83 K. Xu, Y. Li, T. Liu, F. Yang, C. Xu and J. Gao, *IEEE Nanotechnology Magazine*, 2013, 15–18.
- 84 K. Xu, Y. Li, F. Yang, W. Yang, L. Zhang, C. Xu, T. Kaneko and R. Hatakeyama, *Carbon*, 2014, **68**, 511–519.
- 85 S. Abdullayeva and N. Musayeva, *World J. Condens. Matter Phys.*, 2014, 93–100.

- 86 C. P. Li, X. H. Sun, N. B. Wong, C. S. Lee, S. T. Lee and B. K. Teo, *Chem. Phys. Lett.*, 2002, **365**, 22–26.
- 87 B. K. Teo, C. P. Li, X. H. Sun, N. B. Wong and S. T. Lee, *Inorg. Chem.*, 2003, **42**, 6723–6728.
- 88 A. Bazargan and G. McKay, *Chem. Eng. J.*, 2012, **195–196**, 377–391.
- 89 W. Zhao, B. Basnet and I. J. Kim, *J. Adv. Ceram.*, 2012, **1**, 179–193.
- 90 N. Wang, *Nature*, 2000, **408**, 50–51.
- 91 *Plan Director de Residuos Sólidos de Montevideo y Área Metropolitana - ANEXO: Residuos Sólidos Industriales*, http://www.cempre.org.uy/docs/biblioteca/plan_director/etapa1_estudios_basicos/Anexo_RSI.PDF, (accessed June 2016), Fichtner GmbH CO&KG and LKSur S.A., 2005.
- 92 N. Souza, M. Zeiger, V. Presser and F. Mücklich, *RSC Adv.*, 2015, **5**, 62149–62159.
- 93 S. Bhatia, *Zeolite catalysis: principles and applications*, CRC Press, Boca Raton, 1990.
- 94 W. A. Deer and R. A. Howie, *Rock-forming Minerals: Silica Minerals*, Geological Society of London, London, 2004.
- 95 W. N. Reynolds, *Physical properties of graphite*, Elsevier, 1968.
- 96 C. S. Cundy and P. A. Cox, *Microporous Mesoporous Mater.*, 2005, **82**, 1–78.
- 97 C. Baerlocher and L. B. McCusker, *Database zeolite struct.*, <http://www.iza-structure.org>.
- 98 N. Salahudeen, A. S. Ahmed, A. H. Al-Muhtaseb, M. Dauda, S. M. Waziri and B. Y. Jibril, *Appl. Clay Sci.*, 2015, **105–106**, 170–177.
- 99 T. Willhammar, J. Sun, W. Wan, P. Oleynikov, D. Zhang, X. Zou, M. Moliner, J. Gonzalez, C. Martínez, F. Rey and A. Corma, *Nat. Chem.*, 2012, **4**, 188–194.
- 100 A. L. Patterson, *Phys. Rev.*, 1939, **56**, 978–982.
- 101 S. Reich and C. Thomsen, *Philos. Trans. R. Soc., A*, 2004, **362**, 2271–2288.
- 102 L. Ian, *Handbook of Raman Spectroscopy. From the Research Laboratory to the Process Line*, CRC Press, New York and Basel, 2001, vol. 28.
- 103 R. A. DiLeo, B. J. Landi and R. P. Raffaele, *J. Appl. Phys.*, 2007, **101**, 064307.
- 104 J. Schwan, S. Ulrich, V. Batori, H. Ehrhardt and S. R. P. Silva, *J. Appl. Phys.*, 1996, **80**, 440.
- 105 D. G. Gromov and S. A. Gavrilov, *Thermodynamics – Physical Chemistry of Aqueous Systems*, InTech, 2011.
- 106 K. Pathak, PhD thesis, University of Akron, 2008.
- 107 P. Nash and A. Nash, *Bull. Alloy Phase Diagrams*, 1987, **8**, 6–14.
- 108 Y. Chen, J. Li and J. Dai, *Chem. Phys. Lett.*, 2001, **344**, 450–456.
- 109 H. Wang, X. Zhang, X. Meng, S. Zhou, S. Wu, W. Shi and S. Lee, *Angew. Chem., Int. Ed.*, 2005, **44**, 6934–6937.
- 110 K. Saulig-Wenger, D. Cornu, F. Chassagneux, T. Epicier and P. Miele, *J. Mater. Chem.*, 2003, **13**, 3058.
- 111 K. H. Lee, S. W. Lee, R. R. Vanfleet and W. Sigmund, *Chem. Phys. Lett.*, 2003, **376**, 498–503.
- 112 D. R. Lide, *Handbook of Chemistry and Physics*, CRC Press, 2002.
- 113 P. Patnaik, *Handbook of Inorganic Chemicals*, 2003.
- 114 Q. Zhao, X. Xu, H. Zhang, Y. Chen, J. Xu and D. Yu, *Appl. Phys. A: Mater. Sci. Process.*, 2004, **79**, 1721–1724.
- 115 S. J. Park, J. G. Kim and D. J. Choi, *Int. J. Appl. Ceram. Technol.*, 2015, **6**, 1–6.
- 116 C. Fantini, A. Jorio, M. Souza, M. S. Strano, M. S. Dresselhaus and M. A. Pimenta, *Phys. Rev. Lett.*, 2004, **93**, 1–4.
- 117 M. S. Dresselhaus, G. Dresselhaus, R. Saito and A. Jorio, *Phys. Rep.*, 2005, **409**, 47–99.
- 118 A. C. Ferrari and J. Robertson, *Phys. Rev. B: Condens. Matter Mater. Phys.*, 2000, **61**, 14095–14107.
- 119 P. S. Santos, H. S. Santos and S. P. Toledo, *Mater. Res.*, 2000, **3**, 104–114.
- 120 S. S. Lin, *J. Phys. Chem. C*, 2012, **116**, 3951–3955.
- 121 J. H. Lehman, M. Terrones, E. Mansfield, K. E. Hurst and V. Meunier, *Carbon*, 2011, **49**, 2581–2602.
- 122 R. Gupta, B. P. Singh, V. N. Singh, T. K. Gupta and R. B. Mathur, *Carbon*, 2014, **66**, 724–726.
- 123 D. W. Breck, *Zeolite molecular sieves: structure, chemistry, and use*, Wiley, 99th edn, 1973.
- 124 D. Zappa, S. Dalola, G. Faglia, E. Comini, M. Ferroni, C. Soldano, V. Ferrari and G. Sberveglieri, *Beilstein J. Nanotechnol.*, 2014, **5**, 927–936.

5. Conclusion and outlook

This work delves into two pressing matters in CNT science, with direct implications in industry: CNT quality and sustainability. Insufficient CNT quality – which encompasses both crystallinity and purity – and inadequate existing purification techniques, as well as dedicated petrochemical carbon precursors, were the motivation in the search for alternatives and improvements.

For the framework of this study, a lab-scale oven laser apparatus was constructed around a pulsed nanosecond laser. Pulsed laser deposition of single- and multiwall carbon nanotubes was successfully demonstrated and tuned by means of a least squares statistical analysis, taking into account process parameters gas pressure, gas flow and chamber temperature. This setup and optimised parameters provided the CNTs required for the present work, summarised in the following.

The subject of CNT purification and defect healing is approached in an initial proof of concept for an ambient laser-based treatment (4.1). After establishing the context of pertinent state-of-the-art techniques, laser stood out as a fast, scalable and flexible method. The limited body of literature that had stumbled upon the advantageous effect of laser radiation lacked in observation and understanding. To fill this void, very local μm -scale laser radiation was applied to SWCNTs with varying powers and exposure times. Consequently, Raman-based indicators for tube defect density, such as I_D/I_{G^+} , dropped 94 %, while the purity, I_{G^+}/I_D , increased 17-fold compared to pristine samples. Similar results were obtained in samples that had been previously damaged to reproduce the processing steps of metal matrix composites.

The posited effects and advantages of laser healing were convincingly brought forth, yet the scale of the experiments rendered site-specific comparative characterisation unmanageable. A second scaled-up iteration (4.2) was able to confirm previous results, now backed up by and correlated to electrical resistance and hydrogen adsorption measurements. A \varnothing 6 mm beam produced a Raman-based 80 % improvement in tube crystallinity and a 6-fold purity, both reaching out passed the treated area in the heat-affected zone. The average electrical resistance across 200 μm stretches dropped by two thirds from ca. 750 Ω to 250 Ω , with its data-spread resembling that of the crystallinity, indicating the preponderance of defects on

electrical resistance. Hydrogen uptake also dropped to a third, given that adsorption is tied to defect sites, further supporting previous claims.

This two-part study showed ample indications that laser radiation effectively heals defects, removes impurities and homogenises SWCNT samples, as confirmed by Raman spectroscopy, electrical resistance, gas adsorption and thermogravimetry. The main findings include:

- tuned laser radiation can damage or heal CNTs, based on power density and radiation times;
- lattice defects are removed on a time scale one order of magnitude shorter than impurities;
- the technique is fast, contactless, ambient and adaptable to any CNT sample type or morphology;
- composite processing-based damage due to sheer mixing, ultrasound and centrifugation, can be fully recovered;
- the technique is scalable for integration in CNT synthesis.

These results have consequent advantages and corollaries in:

- applications highly sensitive to lattice defects or impurities;
- excessively time- and/or cost-intensive synthesis and/or purification techniques;
- inadequate purification techniques that further contaminate/damage samples;
- purification techniques incompatible with certain applications when liquid processing-based;
- unavoidable processing-related CNT damage and sullying (e.g., dispersion: ball milling, shear-mixing, ultrasonication, centrifugation, functionalisation);
- rejuvenation of electrical cycling- or wear-related damage to CNT materials, to extend their duty life;
- validation of disputed Raman I_D/I_{G+} and $I_{G'}/I_D$ ratios as indicators of crystallinity and purity;
- any laser-based CNT characterisation method;
- unachievable tube qualities, due to alternative complex organic precursors, bringing such CNTs up to industry standards and closer to sustainability.

Finally, if CNTs are to become as commonplace as their advantages would have them, the question of sustainability emerges. However, a look at standard carbon precursors for CNTs reveals dedicated high-purity petrochemical carbons in all forms. An alternative carbon precursor was thus studied (4.3). A currently wasted by-product of petroleum fluid catalytic cracking, FC3R, was adapted to the PLD apparatus and used as a carbon feedstock to produce SWCNTs, as well as SiONWs from the zeolite content. This addresses the reuse and upcycling of an otherwise wasted and contaminant resource. Such a potent revalorisation could fuel research and applications in CNT-based devices and composites. The novelties of these findings are:

- the first use of a waste feedstock for SiONW synthesis;
- one of very few such attempts for CNTs, OLCs and CNDs;
- the first outlet for FC3R and catalyst coke in general.

The obtained insights address synthesis energy and cost efficiency, sustainability and device/material performance, and should be of great interest to the CNT community. This was to a certain extent confirmed by the publication of each chapter in an international, peer-reviewed journal, a guarantee of the quality of the scientific work therein. All articles are available under a Creative Commons open access license (CC BY), allowing for wider ranging visibility.

Although further fine tuning is required to understand the effect of laser radiation on CNTs and FC3R, the novelties presented here combine seamlessly in current CNT research and industry, putting forth the versatility of both laser and carbon, with directly applicable concepts.

Appendix

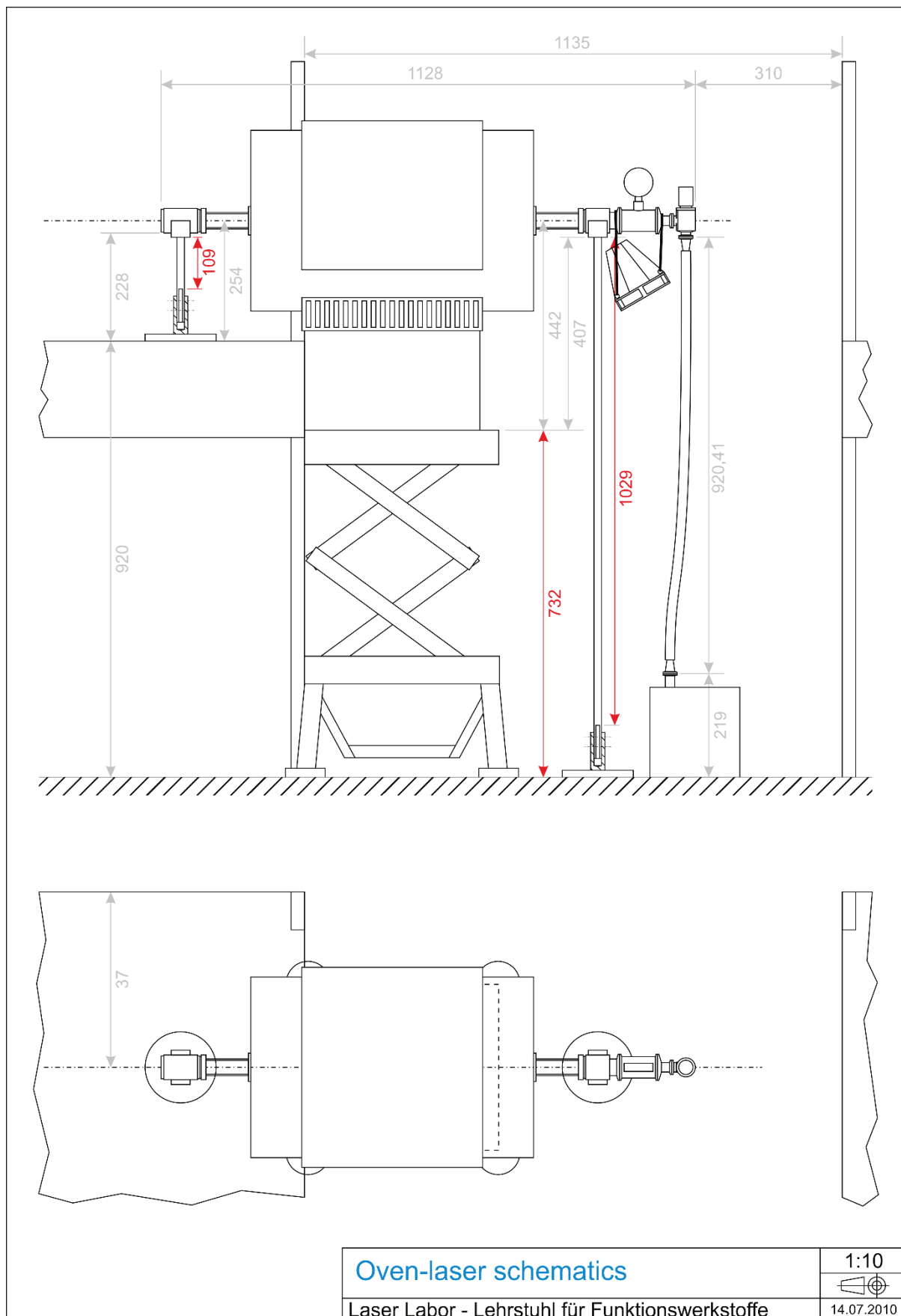


Figure 27 - Early version of the oven-laser PLD schematics.

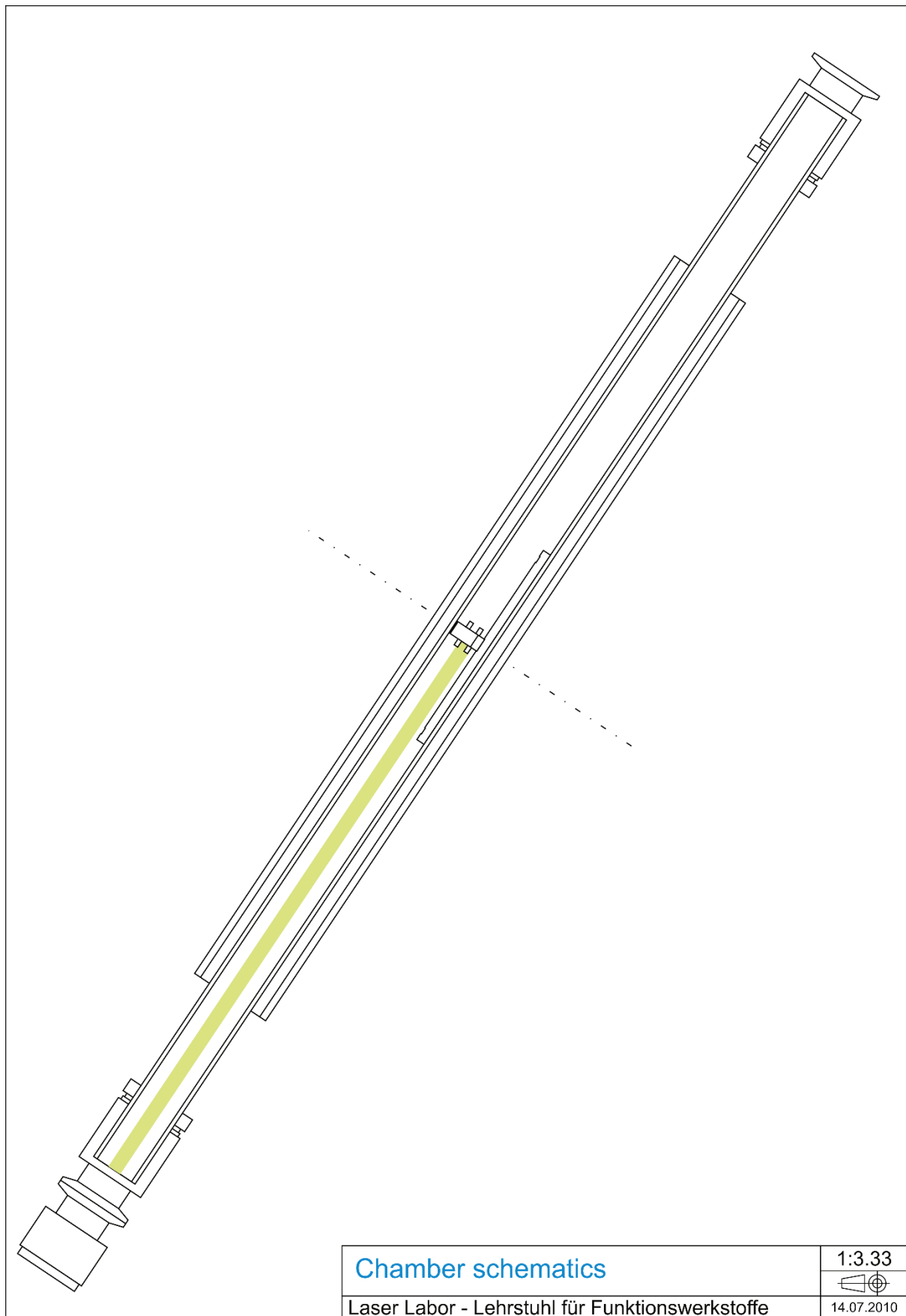


Figure 28 - Tube-in-tube PLD chamber schematics

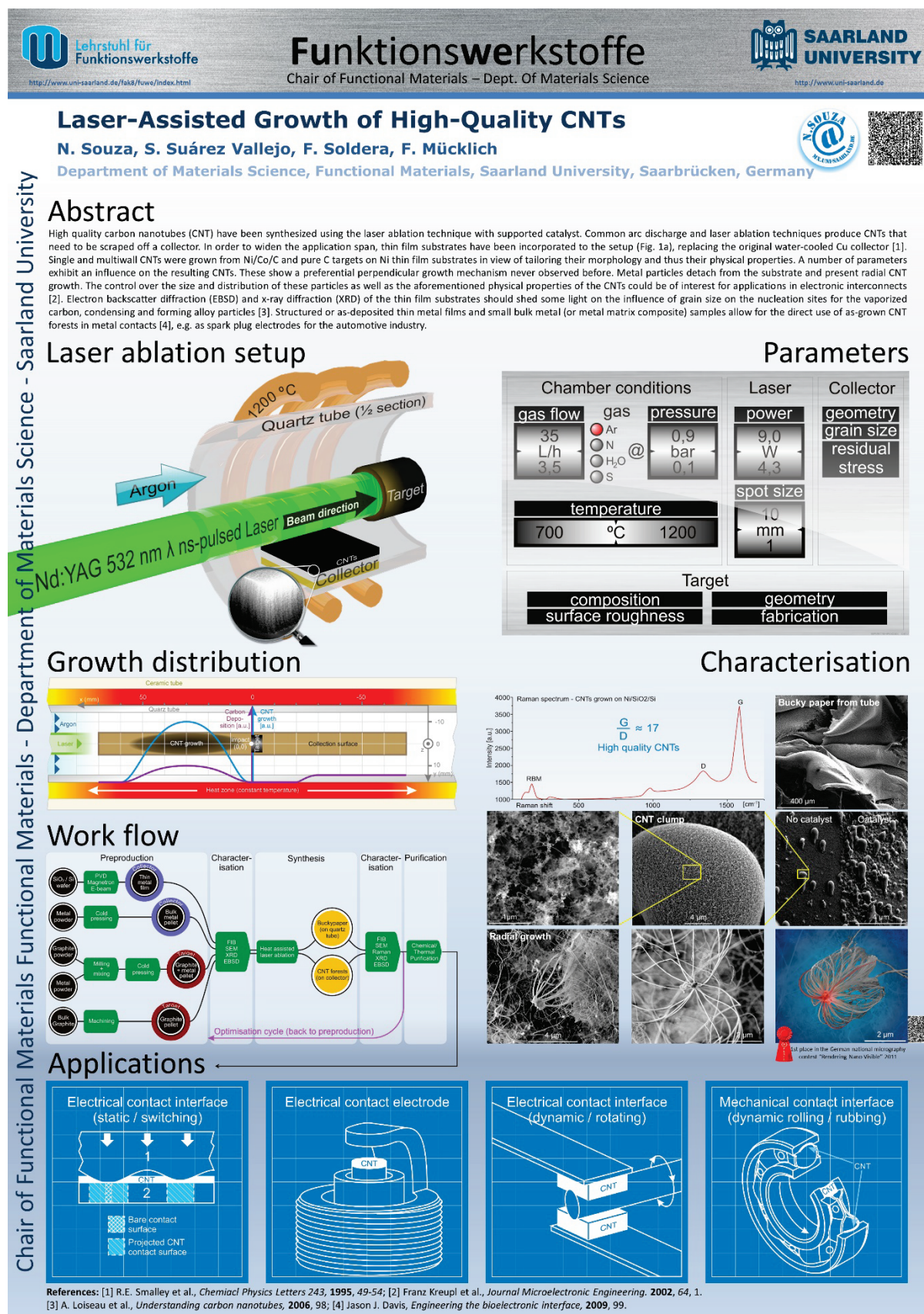


Figure 29 – Poster contribution for ChemOnTubes 2012

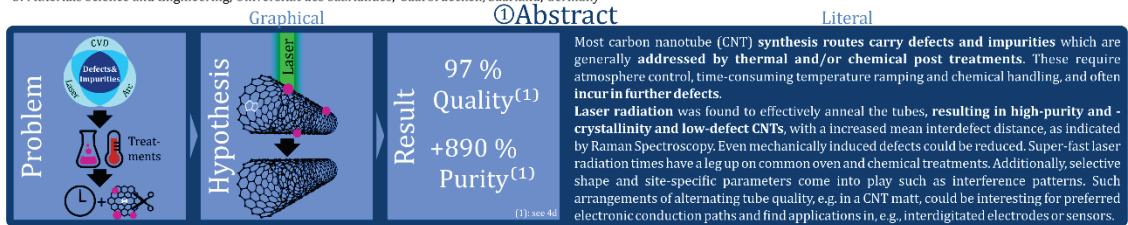
Laser annealing of single-wall carbon nanotubes

Nicolas Souza¹, Volker Presser^{2,3}, Frank Mücklich¹

1: Materials Science and Engineering, Functional Materials, Universität des Saarlandes, Saarbrücken, Saarland, Germany

2: Energy Materials, Leibniz Institute for New Materials, Saarbrücken, Saarland, Germany

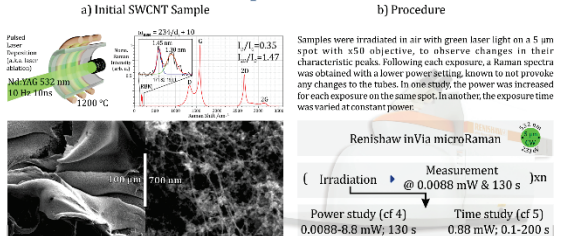
3: Materials Science and Engineering, Universität des Saarlandes, Saarbrücken, Saarland, Germany



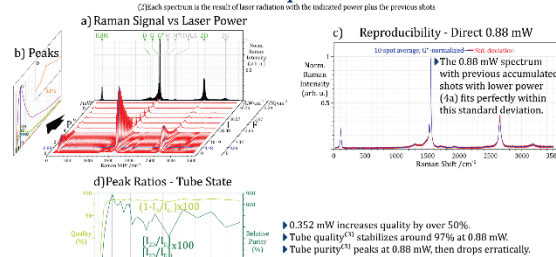
② Previous Studies

Sample	Atmosph.	Power Density [kW/cm ²]	Const. / Pulsed	λ [nm]	t [s]	I_D/I_G	FWHM [D]	Ref.
MWCNT	Air	up to 100	CW	514	2x60	constant -5 cm ² (D&G)	-	Judek, PSSA 2012
SWCNT	Air	0.00065	PW	193	30	100%	-10%	Hurst
		0.00045		248	30	-50%	-30%	J. Phys. Chem. C. 2008
CNT	CO ₂	19	?	1064	?	-	-	Rai Carbon 2004
SWCNT	Air	300	CW	514.5 & 632.8	60-6000	Metallic tubes are destroyed	-	Huang J. Phys. Chem. B. 2006
DWCNT	Air	0.318	PW	355	-	28%	-	Zhang J. Phys. Chem. C. 2006

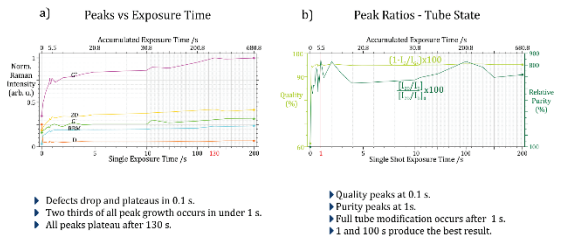
③ Experiment



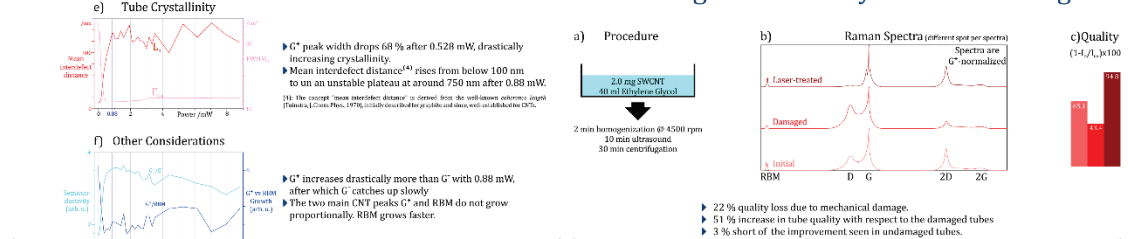
④ Power Dependence ($t=130$ s; same spot⁽²⁾)



⑤ Time ($P=0.88$ mW; same spot)



⑥ Fixing Mechanically-induced Damage



⑦ Conclusions

- Laser radiation effectively reduces defects, increases purity and crystallinity. 4.48 kJ·cm⁻² fluence produced the best results.
- Processing times of ca. 1 s are very short and advantageous compared to thermal (oven) or chemical purification.
- Purification in air produces satisfying results, although atmosphere control can be considered.
- Raman signal intensification solely through increased power input can be excluded, given the unproportional growth of the RBM and G modes.
- Commonly reported irradiance or power density takes only the irradiated area into account yet excludes the time factor, i.e. energy and fluence, a stronger physical representation of the underlying phenomena.
- Raman spectroscopy is an important characterization tool for carbon nanotubes, yet without the proper care, results are not free of uncertainty as to the degree of modification induced by the measurement itself. The fluence should be studied and adapted to each sample to avoid skewed results.
- Mechanically-induced defects were corrected. CNT processing with necessary ultrasonication, e.g. composite manufacturing, could amend unavoidable damage to the tubes [Suarez, PSSA, 2014].

Acknowledgements - EFRE funds of the European Commission for support of activities within the AME-Lab project, F. Lasserre, S. Suarez.



Figure 30 - Poster contribution for NT14 2014



Figure 31 - "Qualle" (Jellyfish): Multiwall CNTs on a Ni particle. Best electron micrograph in Germany - 1st place in national electron micrograph contest Rendering the nanosized visible by cc-nanobionet

Literature

- [1] C. Buzea, I. I. Pacheco, K. Robbie, *Biointerphases* **2007**, 2, MR17.
- [2] M. Cahay, *Quantum Confinement VI: Nanostructured Materials and Devices : Proceedings of the International Symposium*; **2001**.
- [3] E. C. Garnett, M. L. Brongersma, Y. Cui, M. D. McGehee, *Annu. Rev. Mater. Res.* **2011**, 41, 269.
- [4] G. Fedorov, P. Barbara, D. Smirnov, D. Jiménez, S. Roche, *Appl. Phys. Lett.* **2010**, 96, 132101.
- [5] G. Brambilla, D. N. Payne, *Nano Lett.* **2009**, 9, 831.
- [6] R. S. Ruoff, D. Qian, W. K. Liu, *Comptes Rendus Phys.* **2003**, 4, 993.
- [7] K. Mizuno, J. Ishii, H. Kishida, Y. Hayamizu, S. Yasuda, D. N. Futaba, M. Yumura, K. Hata, *Proc. Natl. Acad. Sci. U. S. A.* **2009**, 106, 6044.
- [8] Z. L. Wang, *Adv. Mater.* **2003**, 15, 432.
- [9] X. Zhang, A. J. Du, P. Lee, D. D. Sun, J. O. Leckie, *J. Memb. Sci.* **2008**, 313, 44.
- [10] H. Kroto, A. Allaf, S. Balm, *Chem. Rev.* **1991**.
- [11] S. Iijima, *Nature* **1991**, 354, 56.
- [12] M. Monthieux, V. L. Kuznetsov, *Carbon N. Y.* **2006**, 44, 1621.
- [13] L. V. Radushkevich, V. M. Lukyanovich, *Zhurn. Fiz. Khim.* **1952**, 26, 88.
- [14] Grand View Research, *Carbon Nanotubes (CNT) Market Analysis By Product (Single Walled Carbon Nanotubes (SWCNT), Multi Walled Carbon Nanotubes (MWCNT)), By Application (Polymers, Energy, Electrical & Electronics) And Segment Forecasts To 2022*; San Francisco, **2015**.
- [15] A. Zurutuza, C. Marinelli, *Nat. Nanotechnol.* **2014**, 9, 730.
- [16] O. V. Kharissova, B. I. Kharisov, *RSC Adv.* **2014**, 4, 30807.
- [17] H. Zhu, L. Ci, C. Xu, J. Liang, D. Wu, *Diam. Relat. Mater.* **2002**, 11, 1349.
- [18] C. J. Lee, J. Park, *Appl. Phys. Lett.* **2000**, 77, 3397.
- [19] H. Cui, O. Zhou, B. R. Stoner, *J. Appl. Phys.* **2000**, 88, 6072.
- [20] H. Kataura, Y. Kumazawa, Y. Maniwa, I. Umezue, S. Suzuki, Y. Ohtsuka, Y. Achiba, *Synth. Met.* **1999**, 103, 2555.
- [21] R. Saito, M. Fujita, G. Dresselhaus, M. S. Dresselhaus, *Phys. Rev. B* **1992**, 46, 1804.
- [22] M. J. O'Connell, *Carbon Nanotubes Properties and Applications*; CRC Press: Boca Raton,

2006.

- [23] M. Ahlskog, P. Hakonen, M. Paalanen, L. Roschier, R. Tarkiainen, *J. Low Temp. Phys.* **2001**, *124*, 335.
- [24] J. Robertson, G. Zhong, S. Hofmann, B. C. Bayer, C. S. Esconjauregui, H. Telg, C. Thomsen, *Diam. Relat. Mater.* **2009**, *18*, 957.
- [25] S. A. Getty, E. Cobas, M. S. Fuhrer, **2004**, *4*, 35.
- [26] S. Hong, S. Myung, *Nat. Nanotechnol.* **2007**, *2*, 207.
- [27] S. B. Desai, S. R. Madhupathy, A. B. Sachid, J. P. Llinas, Q. Wang, G. H. Ahn, G. Pitner, M. J. Kim, J. Bokor, C. Hu, H.-S. P. Wong, A. Javey, *Science* **2016**, *354*, 99.
- [28] M. M. Shulaker, G. Hills, N. Patil, H. Wei, H.-Y. Chen, H.-S. P. Wong, S. Mitra, *Nature* **2013**, *501*, 526.
- [29] E. Pop, D. Mann, Q. Wang, K. Goodson, H. J. Dai, *Nano Lett.* **2006**, *6*, 96.
- [30] J. P. Lu, *Phys. Rev. Lett.* **1997**, *79*, 1297.
- [31] M. Yu, *Science* **2000**, *287*, 637.
- [32] B. G. Demczyk, Y. M. Wang, J. Cumings, M. Hetman, W. Han, A. Zettl, R. O. Ritchie, *Mater. Sci. Eng. A* **2002**, *334*, 173.
- [33] M. Popov, M. Kyotani, R. Nemanich, Y. Koga, *Phys. Rev. B* **2002**, *65*, 1.
- [34] L. Reinert, S. Suárez, A. Rosenkranz, *Lubricants* **2016**, *4*, 11.
- [35] M. J. O'Connell, S. M. Bachilo, C. B. Huffman, V. C. Moore, M. S. Strano, E. H. Haroz, K. L. Rialon, P. J. Boul, W. H. Noon, C. Kittrell, J. Ma, R. H. Hauge, R. B. Weisman, R. E. Smalley, *Science* **2002**, *297*, 593.
- [36] P. Avouris, M. Freitag, V. Perebeinos, *Nat. Photonics* **2008**, *2*, 341.
- [37] M. S. Dresselhaus, G. Dresselhaus, R. Saito, A. Jorio, *Phys. Rep.* **2005**, *409*, 47.
- [38] M. Terrones, *Annu. Rev. Mater. Res.* **2003**, *33*, 419.
- [39] C. W. Lung, N. H. March, *Mechanical Properties of Metals - Atomistic and Fractal Continuum Approaches*; World Scientific Publishing Co. Pte. Ltd.: Singapore, **1999**.
- [40] M. S. Dresselhaus, G. Dresselhaus, A. Jorio, A. G. Souza Filho, R. Saito, *Carbon N. Y.* **2002**, *40*, 2043.
- [41] A. C. Ferrari, *Solid State Commun.* **2007**, *143*, 47.
- [42] L. G. Cançado, A. Jorio, E. H. M. Ferreira, F. Stavale, C. A. Achete, R. B. Capaz, M. V. O. Moutinho, A. Lombardo, T. S. Kulmala, A. C. Ferrari, *Nano Lett.* **2011**, *11*, 3190.
- [43] J. Schwan, S. Ulrich, V. Batori, H. Ehrhardt, S. R. P. Silva, *J. Appl. Phys.* **1996**, *80*, 440.

- [44] S. Reich, C. Thomsen, *Philos. Trans. A. Math. Phys. Eng. Sci.* **2004**, 362, 2271.
- [45] R. Prada Silvy, Y. Tan, P. Wallis, Single-wall Carbon Nanotubes: Recent Advances, Manufacturing, Characterization and Applications. *Sigma-Aldrich - CoMoCAT® Single-wall Carbon Nanotub.* **2016**. <http://www.sigmaaldrich.com/technical-documents/articles/materials-science/nanomaterials/comocat-carbon-nanotubes.html> (accessed 2017-01-18)
- [46] R. A. DiLeo, B. J. Landi, R. P. Raffaele, *J. Appl. Phys.* **2007**, 101, 64307.
- [47] J. A. Elliott, J. K. W. Sandler, A. H. Windle, R. J. Young, M. S. P. Shaffer, *Phys. Rev. Lett.* **2004**, 92, 92.
- [48] P. Queipo, A. G. Nasibulin, S. D. Shandakov, H. Jiang, D. Gonzalez, E. I. Kauppinen, *Curr. Appl. Phys.* **2009**, 9, 301.
- [49] P. G. Collins, In *Oxford Handbook of Nanoscience and Technology: Volume 2: Materials: Structures, Properties and Characterization Techniques*; Narlikar, A. V.; Fu, Y. Y., Eds.; Oxford University Press, **2010**; Vol. 2, pp. 31–93.
- [50] S. Mathew, U. M. Bhatta, B. Joseph, B. N. Dev, *Nucl. Instruments Methods Phys. Res. Sect. B Beam Interact. with Mater. Atoms* **2007**, 264, 36.
- [51] A. Aitkaliyeva, Irradiation Stability of Carbon Nanotubes, Texas A&M University, **2009**.
- [52] S. Suzuki, *Low-Energy Irradiation Damage in Single-Wall Carbon Nanotubes*; Marulanda, J. M., Ed.; InTech, **2011**.
- [53] A. V Krashennnikov, K. Nordlund, J. Keinonen, *Phys. Rev. B* **2002**, 65, 1.
- [54] J.-C. Charlier, *Acc. Chem. Res.* **2002**, 35, 1063.
- [55] N. Souza, M. Zeiger, V. Presser, F. Mücklich, *RSC Adv.* **2015**, 5, 62149.
- [56] M. S. Dresselhaus, G. Dresselhaus, P. Avouris, *Carbon nanotubes: synthesis, structure, properties, and applications*; Dresselhaus, M. S.; Dresselhaus, G.; Avouris, P., Eds.; Springer, **2003**.
- [57] S. Bellucci, *Physical Properties of Ceramic and Carbon Nanoscale Structures*; Bellucci, S., Ed.; **2011**.
- [58] H. Shima, M. Sato, *Elastic and Plastic Deformation of Carbon Nanotubes*; **2013**; Vol. 72.
- [59] A. S. Paipetis, V. Kostopoulos, *Carbon Nanotube Enhanced Aerospace Composite Materials: A New Generation of Multifunctional Hybrid Structural Composites*; Paipetis, A. S.; Kostopoulos, V., Eds.; Springer, **2013**.
- [60] T. Gates, G. Jefferson, S.-J. Frankland, In *49th AIAA/ASME/ASCE/AHS/ASC Structures, Structural Dynamics, and Materials Conference 16th AIAA/ASME/AHS Adaptive Structures Conference 10t*; American Institute of Aeronautics and Astronautics: Reston, Virginia, **2008**; pp. 1–12.
- [61] A. M. Beese, X. Wei, S. Sarkar, R. Ramachandramoorthy, M. R. Roenbeck, A. Moravsky,

- M. Ford, F. Yavari, D. T. Keane, R. O. Loutfy, S. T. Nguyen, H. D. Espinosa, *ACS Nano* **2014**, *8*, 11454.
- [62] A. Gorbunoff, O. Jost, In *Pulsed Laser Deposition of Thin Films: Applications-Led Growth of Functional Materials*; Eason, R., Ed.; Wiley-Interscience: Hoboken, **2007**; pp. 613–632.
- [63] G. G. Tibbetts, *J. Cryst. Growth* **1984**, *66*, 632.
- [64] M. H. Rummeli, A. Bachmatiuk, F. Börrnert, F. Schäffel, I. Ibrahim, K. Cendrowski, G. Simha-Martynkova, D. Plachá, E. Borowiak-Palen, G. Cuniberti, B. Büchner, *Nanoscale Res. Lett.* **2011**, *6*, 303.
- [65] A. S. Amelinckx, X. B. Zhang, D. Bernaerts, X. F. Zhang, V. Ivanov, J. B. Nagy, **2016**, *265*, 635.
- [66] R. T. K. Baker, *Carbon N. Y.* **1989**, *27*, 315.
- [67] G. G. Tibbetts, M. G. Devour, E. J. Rodda, *Carbon N. Y.* **1987**, *25*, 367.
- [68] S. B. Sinnott, R. Andrews, D. Qian, A. M. Rao, Z. Mao, E. C. Dickey, F. Derbyshire, *Chem. Phys. Lett.* **1999**, *315*, 25.
- [69] Y. Li, W. Kim, Y. Zhang, M. Rolandi, D. Wang, H. Dai, *J. Phys. Chem. B* **2001**, *105*, 11424.
- [70] R. Bacon, *J. Appl. Phys.* **1960**, *31*, 283.
- [71] M. José-Yacamán, M. Miki-Yoshida, L. Rendón, J. G. Santiesteban, *Appl. Phys. Lett.* **1993**, *62*, 657.
- [72] K. A. Shah, B. A. Tali, *Mater. Sci. Semicond. Process.* **2016**, *41*, 67.
- [73] T. Guo, P. Nikolaev, A. G. Rinzler, D. Tomanek, D. T. Colbert, R. E. Smalley, *J. Phys. Chem.* **1995**, *99*, 10694.
- [74] T. Guo, P. Nikolaev, A. Thess, D. T. Colbert, R. E. Smalley, *Chem. Phys. Lett.* **1995**, *243*, 49.
- [75] E. Munoz, W. Maser, A. Benito, *Synth. Met.* **1999**, *103*, 2490.
- [76] M. Bystrzejewski, M. H. Rummeli, H. Lange, A. Huczko, P. Baranowski, T. Gemming, T. Pichler, *J. Nanosci. Nanotechnol.* **2008**, *8*, 6178.
- [77] Y. Zhang, S. Iijima, *Appl. Phys. Lett.* **1999**, *75*, 3087.
- [78] M. Zhang, M. Yudasaka, S. Iijima, *Chem. Phys. Lett.* **2001**, *336*, 196.
- [79] M. Yudasaka, M. Zhang, S. Iijima, *Chem. Phys. Lett.* **2000**, *323*, 549.
- [80] O. Jost, R. Friedlein, A. A. Gorbunov, T. Pichler, M. Reibold, H.-D. Bauer, M. Knupfer, M. S. Golden, L. Dunsch, J. Fink, W. Pompe, In *The 13th international winterschool on electronic properties of novel materials - science and technology of molecular nanostructures*; ASCE, **1999**; Vol. 486, pp. 288–291.

- [81] H. Kataura, A. Kimura, Y. Ohtsuka, S. Suzuki, Y. Maniwa, T. Hanyu, Y. Achiba, *Japanese J. Appl. Physics, Part 2 Lett.* **1998**, 37.
- [82] H. Kataura, Y. Kumazawa, Y. Maniwa, Y. Ohtsuka, R. Sen, S. Suzuki, Y. Achiba, *Carbon N. Y.* **2000**, 38, 1691.
- [83] O. Jost, A. Gorbunov, X. Liu, W. Pompe, J. Fink, *J. Nanosci. Nanotechnol.* **2004**, 4, 433.
- [84] M. Yudasaka, N. Sensui, M. Takizawa, S. Bandow, T. Ichihashi, S. Iijima, *Chem. Phys. Lett.* **1999**, 312, 155.
- [85] O. Jost, A. A. Gorbunov, W. Pompe, T. Pichler, R. Friedlein, M. Knupfer, M. Reibold, H.-D. Bauer, L. Dunsch, M. S. Golden, J. Fink, *Appl. Phys. Lett.* **1999**, 75, 2217.
- [86] O. Jost, A. A. Gorbunov, J. Möller, W. Pompe, X. Liu, P. Georgi, L. Dunsch, M. S. Golden, J. Fink, *J. Phys. Chem. B* **2002**, 106, 2875.
- [87] S. Bandow, S. Asaka, Y. Saito, A. M. Rao, L. Grigorian, E. Richter, P. C. Eklund, *Phys. Rev. Lett.* **1998**, 80, 3779.
- [88] D. Nishide, H. Kataura, S. Suzuki, K. Tsukagoshi, Y. Aoyagi, Y. Achiba, *Chem. Phys. Lett.* **2003**, 372, 45.
- [89] E. Munoz, W. Maser, A. Benito, *Carbon N. Y.* **2000**, 38, 1445.
- [90] Y. Saito, Y. Tani, A. Kasuya, *J. Phys. Chem. B* **2000**, 104, 2495.
- [91] A. A. Gorbunov, R. Friedlein, O. Jost, M. S. Golden, J. Fink, W. Pompe, *Appl. Phys. A Mater. Sci. Process.* **1999**, 69, 593.
- [92] O. Jost, A. A. Gorbunov, J. Möller, W. Pompe, A. Graff, R. Friedlein, X. Liu, M. S. Golden, J. Fink, *Chem. Phys. Lett.* **2001**, 339, 297.
- [93] R. Sen, Y. Ohtsuka, T. Ishigaki, D. Kasuya, S. Suzuki, H. Kataura, Y. Achiba, *Chem. Phys. Lett.* **2000**, 332, 467.
- [94] M. Yudasaka, T. Ichihashi, T. Komatsu, S. Iijima, *Chem. Phys. Lett.* **1999**, 299, 91.
- [95] A. G. Rinzler, J. Liu, H. Dai, P. Nikolaev, C. B. Huffman, F. J. Rodríguez-Macías, P. J. Boul, A. H. Lu, D. Heymann, D. T. Colbert, R. S. Lee, J. E. Fischer, A. M. Rao, P. C. Eklund, R. E. Smalley, *Appl. Phys. A Mater. Sci. Process.* **1998**, 67, 29.
- [96] M. Yudasaka, F. Kokai, K. Takahashi, R. Yamada, N. Sensui, T. Ichihashi, S. Iijima, *J. Phys. Chem. B* **1999**, 103, 3576.
- [97] O. Jost, A. A. Gorbunov, L. C. Ciacchi, W. Pompe, X. Liu, T. Pichler, L. Dunsch, M. S. Golden, J. Fink, In *AIP Conference Proceedings*; AIP, **2001**; Vol. 591, pp. 1–4.
- [98] A. Thess, R. Lee, P. Nikolaev, H. Dai, P. Petit, J. Robert, C. Xu, Y. H. Lee, S. G. Kim, A. G. Rinzler, D. T. Colbert, G. E. Scuseria, D. Tomanek, J. E. Fischer, R. E. Smalley, *Science* **1996**, 273, 483.
- [99] C. Bower, S. Suzuki, K. Tanigaki, O. Zhou, *Appl. Phys. A Mater. Sci. Process.* **1998**, 67, 47.

- [100] P. Eklund, B. Pradhan, U. Kim, *Nano Lett.* **2002**.
- [101] N. Braidy, M. El Khakani, G. Botton, *Carbon N. Y.* **2002**, 40, 2835.
- [102] N. Braidy, M. A. El Khakani, G. A. Botton, *J. Mater. Res.* **2002**, 17, 2189.
- [103] A. C. Dillon, P. a. Parilla, J. L. Alleman, J. D. Perkins, M. J. Heben, *Chem. Phys. Lett.* **2000**, 316, 13.
- [104] A. A. Gorbunov, O. Jost, W. Pompe, A. Graff, *Carbon N. Y.* **2002**, 40, 113.
- [105] A. A. Puretzky, D. B. Geohegan, X. Fan, S. J. Pennycook, *Appl. Phys. A Mater. Sci. Process.* **2000**, 70, 153.
- [106] A. A. Puretzky, H. Schittenhelm, X. Fan, M. J. Lance, L. F. Allard, D. B. Geohegan, *Phys. Rev. B* **2002**, 65, 245425.
- [107] M. Yudasaka, Y. Kasuya, F. Kokai, K. Takahashi, M. Takizawa, S. Bandow, S. Iijima, *Appl. Phys. A Mater. Sci. Process.* **2002**, 74, 377.
- [108] U.S. Energy Information Administration, *Supply and disposition - Petroleum Coke*; **2015**.
- [109] L. Masterson, *Energy Arg.* **2015**.
- [110] European Commision, *Integr. Pollut. Prev. Control* **2003**, 518.
- [111] E. C. I. Council, *FCC Equilibrium Catalyst (including FCC catalyst fines) finds safe reuse / rework outlets in Europe*; **2006**.
- [112] U.S._Energy_Information_Administration, *Refinery Yield*; **2015**.
- [113] U.S._Energy_Information_Administration, *Crude Oil Production*; **2015**.
- [114] U.S._Energy_Information_Administration, *Supply and disposition - Catalyst Petroleum Coke*; **2015**.
- [115] Y. Suda, K. Utaka, M. a. Bratescu, Y. Sakai, J. Tsujino, K. Suzuki, *Appl. Phys. A* **2004**, 79, 1331.
- [116] Y. Suda, A. Tanaka, A. Okita, M. A. Bratescu, Y. Sakai, J. Nakamura, G. Y. Xiong, Z. F. Ren, *MRS Proc.* **2004**, 858, HH3.6.
- [117] J. M. Lambert, P. M. Ajayan, P. Bernier, J. M. Planeix, V. Brotons, B. Coq, J. Castaing, *Chem. Phys. Lett.* **1994**, 226, 364.
- [118] N. Souza, M. Roble, D. E. Diaz-Droguett, F. Mücklich, *RSC Adv.* **2017**, 7, 5084.
- [119] N. Souza, F. Lasserre, A. Blickley, M. Zeiger, S. Suárez, M. Duarte, V. Presser, F. Mücklich, *RSC Adv.* **2016**, 6, 72596.

List of figures

Figure 1 – Schematic classification of a nanomaterial according to the number of its external dimensions in (top row) and out of (bottom row) the nanoscale.....	1
Figure 2 - Fullerene (green), CNT (blue) and graphene (yellow) discovery and Nobel prize (N) milestones, and publications per year. Data from Web of Science, corrected for the variety of nomenclatures for each species and cross-hits (e.g. “fullerene” in “tubular fullerene”).....	3
Figure 3 – Yearly world CNT market estimate by segment (in kT; left axis) and forecast ^[14] ; gram price trend based on single-wall carbon nanotube prices of 1500 \$ in 2000, 50 \$ in 2010 and 2 \$ in 2016 (USD/g; right axis).	3
Figure 4 – sp^2 carbon lattice with two neighbouring atoms and the atomic and molecular orbitals at play.	4
Figure 5 - CNT chirality map. 30° wedge of a symmetry-simplified infinite graphene sheet, defined by absolute (x,y) coordinates and unit vectors (a_1, a_2). Tube-defining parametres C_h , T , d_t and θ are represented. Colour code key represents band gaps.....	5
Figure 6 - CNT morphology: zigzag (a), armchair (b) and chiral tubes; capped tube end (d); MWCNT (e).....	6
Figure 7 – Experimental specific stiffness (E modulus / density) vs specific strength of CNTs compared to those of relevant competing structural materials (CFRP: carbon fiber reinforced plastic). Double logarithmic scale.	8
Figure 8 - Raman spectrum (red line) of synthesised SWCNT sample with expanded y-axis (pink surface) to observe more features ^[37]	10
Figure 9 - Examples of local disorder in CNTs. Mono- (a) and di-vacancies before and after reconstruction (H-termination of the remaining dangling bond in (a). (c) Single (Thrower) and double (Dienes) 5-7 defects and their effect (left), or absence thereof (right), on long-range order (perpendicular and angled perspectives with cell guidelines). Adapted from ^[49]	13
Figure 10 - Tip (a) and base (b) growth models. C_x are the various precursor species.	14
Figure 11 - Arc discharge schematics.....	16
Figure 12 - CVD schematics.....	17
Figure 13 - Laser ablation schematics.....	17
Figure 14 – Influence of the furnace temperature T (solid circles, solid line), the carrier gas flow velocity v (open squares, dashed line) and pressure P (open circles, dotted line), and the	

laser fluence ϕ (solid squares, dash-dot line) on the relative SWCNT abundance in the laser evaporated soot ^[91] . Each curve represents the effect of variation of one parameter with all other specified in Table 1 constant. Adapted from ^[62]	19
Figure 15 - First second of SWCNT life: time (t) scale of the ablation products, their temperature (T_p , yellow curve) and their pressure (P_p , green curve). Initial temperature (T_0) and pressure (P_0), (any) fullerene (C_{60}), amorphous carbon (aC), fireball time (t_p), nanoparticle (np), condensation time (t_p), eutectic temperature (T_{eut}), thermal equalisation time (t_T), room temperature (T_{room}). Summary of the time scale and rough qualitative curves of the data described in ^[62,91,93,104–107]	20
Figure 16 - Approx. 2014 U.S. crude barrel yield (%) ^[112] : of the 10 % PC, 73 % is marketable and 27 % is non-marketable catalyst coke. Estimated from 2014 US production (3,2 B (10^9) barrels of crude ^[113] , 0,32 B barrels of PC ^[108] and 85 M barrels of CC ^[114]).	21
Figure 17 – Summarised global strategy and parameters to adress the defined goals. Title of the work: “Laser and carbon: nanotube synthesis and annealing”	23
Figure 18 - Basic principles of pulsed laser depostion of carbon nanotubes	24
Figure 19 – Specification and functional schematics of oven-laser aparatus	25
Figure 20 – Target and sample assembly: target (yellow) held by three alumina pins (red), force-assembled in the target holder (blue), carried by the sample tray (green).	26
Figure 21 – Experimental PLD oven-laser aparatus with laser and gas IN and OUT sides. CNT deposition can be observed on the quartz tube OUT side.	27
Figure 22 - Renishaw inVia Raman system. Closed sample chamber and system (left) and opened (right).	28
Figure 23 – Electrical resistance measurement setup (left), close-up of contact calibration on a micrometer ruler (centre), view through microscope (right).	29
Figure 24 - Graphical abstract: defective (red pentagons) SWCNT irradiated with green (532 nm) light, producing heat (orange glow).	30
Figure 25 - Graphical abstract: defective (red pentagons) and contaminated (black spheres) SWCNT irradiated with green (532 nm) light, producing heat (orange glow). Right: defect- and impurity-free SWCNT injected with electrons and hydrogen.	43
Figure 26 - Graphical abstract: FC3R particle (centre) with a zeolite core and graphitic shell produces SWCNTs (left) and SiONWs (right)	53
Figure 27 - Early version of the oven-laser PLD schematics.	69

Figure 28 - Tube-in-tube PLD chamber schematics	70
Figure 29 – Poster contribution for ChemOnTubes 2012.....	71
Figure 30 - Poster contribution for NT14 2014.....	72
Figure 31 - “Qualle” (Jellyfish): Multiwall CNTs on a Ni particle. Best electron micrography in Germany - 1st place in national electron micrography contest Rendering the nanosized visible by cc-nanobionet	73

List of symbols

a	length
a_1, a_2	unit vectors
$\alpha-, \gamma-, \delta-, \theta-$	(Al ₂ O ₃) alumina polymorphs
A	area
aC	amorphous carbon
C	carbon
C_f	linear sensitivity factor
C_h	chiral vector
C_{60}	60-atom fullerene, any fullerene
d	atomic orbital, diameter
d_c	film thickness
d_t	tube diameter
D	Raman mode
D_b	beam diameter
D_{t_i}	interior tube diameter
Δ	variation
€	euro
e	Euler’s number
E	energy
F	fluence, frequency
Φ	fluence
G	gas, quantum conductance, Raman mode
G_0	conductance quantum

G', G^+, G^-	Raman modes
Γ	peak width
h	Plank constant
η	energetic efficiency
I	intensity, irradiance
L	length
$K\alpha, L\alpha, L\gamma$	electron shell energy transitions
L_a	coherence length
λ	wavelength
m	mass
m_R	residual mass
n, m, j	multiples
μ	shear modulus
N	number of channels
ω	frequency
P	purity, power, pressure
p_u	atomic orbital (axis u)
π	molecular orbital
Q	quality, flow, heat
R	electrical resistance
R^2	coefficient of determination
ρ	density
S	solid
sp^n	hybrid atomic orbital
σ	molecular orbital, standard deviation
Σ	sum
t	time
t_{cond}, t_{drift}	time of condensation, drift time
T	carbon nanotube axis vector, transmissivity, temperature, period
T_{eut}, T_{room}	eutectic temperature, room temperature
$T_1\%$	carbonaceous purity

τ	pulse duration
θ	chiral angle, temperature
v	velocity
Y	yield
\varnothing	diameter

List of abbreviations

CC	catalyst coke
CFRP	carbon fibre reinforced plastic
CND	carbon nanodiamond
CNT	carbon nanotube
CVD	chemical vapour deposition
CW	continuous wave
x-D	x-dimensional
DC	direct current
DNA	deoxyribonucleic acid
DOS	density of states
DSC	differential scanning calorimetry
ECAT	equilibrium catalyst
EDS	energy-dispersive X-ray spectroscopy
EPCAT	electrostatic precipitator catalyst
FAU	faujasite
FCC	fluid catalytic cracking
FC3R	FCC catalyst residue
FFT	fast Fourier transform
FIB	focused ion beam
FWHM	full width at half maximum
FWTM	full width at tenth maximum
HAZ	heat-affected zone
HP	hydroprocessing
HPCR	HP catalyst residue

LA	laser ablation
MWCNT	multiwall CNT
OLC	onion-like carbon
PC	petroleum coke
PLD	pulsed laser deposition
PW	pulsed wave
RBM	radial breathing mode
RO	randomly ordered
RPM	revolutions per minute
SEM	scanning electron microscopy
SiONW	silica nanowire
SLS	solid liquid solid
SWCNT	single wall CNT
TEM	transmission electron microscopy
TG	thermogravimetry
TGA	thermogravimetric analysis
VA	vertically-aligned
VACNT	vertically-aligned CNT
VLS	vapour liquid solid
XRD	x-Ray diffraction

List of units

A	ampere
Å	ångström
bar	bar
°	angular degree
°C	Celsius degree
atm	atmosphere
at%	atomic percent
eV	electron volt

g	gram
Hz	hertz
J	joule
m	metre
min	minute
Ω	ohm
Pa	pascal
s	second
sccm	standard cubic centimetre per minute
T	ton
V	volt
W	watt
wt%	weight percent

Lebenslauf

Dipl.-Ing. Nicolas Souza, Cand. Dr.

Schönwalder Str. 20, 13347, Berlin
nicolas.souza.carmona@gmail.com +49 1575 1572573



Maschinenbau

Europäisches Doppeldiplom (FR & DE)

„Concéption de systems mécaniques & Productions- und Werkstofftechnik“

4-sprachig EN / FR / ES / DE

Schlüsselfertigkeiten

Industrie

Projekt- & Produktionsmanagement, Lean Production, Fertigungsprozesse, Qualitätssicherung, Reliability Engineering, Bosch/Toyota Production System, Technisches Schreiben & Übersetzen, SAP

Bauteil/Maschine

Mechanische Konstruktion, Materialwissenschaft, Festkörpermechanik, 3D-Modellierung, technisches Zeichnen, zerspanende Fertigungsverfahren

Forschung


Just-In-Sequence-Planen, Laserbearbeitung, Ultraschallschweißen, Carbon Nanotube Synthese, Herstellung Komposite aus Metall/Kunststoff, Materialcharakterisierung (Rasterelektronenmikroskop, Ionenstrahl, Röntgenbeugung, Raman Spectroscopie), mechanische Belastbarkeitsprüfung

AKADEMISCHE AUSBILDUNG

2009 - 2016	Cand. Dr.	Materialwissenschaft	Uni. Saarland	Saarbrücken, DE
2004 - 2008	Dipl.-Ing.	Produktions- & Werkstofftechnik	50 % TU KL	Kaiserslautern, DE
	M.Sc. / Ingénieur	Mechanical Systems Design	50 % INSA Rouen	Rouen, FR
Somm. 2004	Praktikant	Mechanische CAD	Corus Aluminium	Koblenz, DE
Somm. 2003	Praktikant	Mechanische Wartung	Mateu Cromo	Madrid, ES
2002 - 2004	B.Sc.	Ingenieur (zweisprach. 50% FR/EN)	INSA Rouen	Rouen, FR
Somm. 2002	Abitur	70/100; angenommen in Maschinenbau bei Carlos III		Madrid, ES

BERUFSERFAHRUNG

10.09 - 02.16	Forscher, Lehrkraft & Doktorand		Uni. Saarland	Saarbrücken, DE
Entwicklung, Konstruktion (CAD), Fertigung und Verwertung eine Carbon Nanotube Produktionsanlage; Verantwortlich für Raman Messungen, Laser-Techniker; Industrie Schnittstelle für Atotech bei Carbon Nanotube Forschung; Englische Proofing bei allen Wissenschaftlichen Institutsveröffentlichungen; Mediengestaltung, Web-Design, -Programmierung und -Master von Webseiten für EU-geförderte Kooperationen (nanocom-network.net, suma2.net, create-network.eu) und Förderanträge. Unterrichten, studentische Betreuung und Entwicklung von Inhalte für Vorlesungen (Carbon Nanotubes: Synthese, Eigenschaften & Anwendung - Funktionswerkstoffe II), Laborpraktika (Batterien aus Zitronen, Leiterwerkstoffe, Polarisation), Entwicklung und Betreuung von Klausuren, Studienarbeiten und Praktika. (Kontakt: Frank Mücklich)				
05-10.2008	Lean Production Produktionsplaner		Robert Bosch	Rodez, FR
Planertätigkeiten in der Wasch-, Montage- und Prüflinien in der Projektteilung Hochlauf Common Rail Injektor (CRI 2.2) für Peugeot Citroen PSA : Design, Entwicklung und Einführung von Lean Production Systeme (Ladungsträger, Arbeitstische, Milkrun-Schleifen, Kanban und FIFO Fördersysteme); Erstellung von FMEA, VSD/VSM (Wertromanalyse); Leitung von Abteilungsbesprechungen und Workshops (Projektmanagement) für die Einführung von neue Konzepte und Arbeitsweise; Layout Planung (Anlagen und Einrichtungen); Benchmarking von Best Practices in anderen Boschwerken. Gestaltung einer Druckschleuse zur Reinraum und ein Besprechungsraum. Konzipierung, Anschaffung und Kaufabwicklung; Vorbereitung eines Audits von PSA; Technisches DE/FR Dolmetschen bei der Schulung von Montagetechniker; Design standardisierter Arbeit sowie Erstellung technische Arbeitsblätter. Ressourcenplanung unterstützt durch SAP. (Kontakt: Silvain Bou)				
03-05.2008	Just-In-Sequence Produktionsplaner		Borg Warner TS	Kirchheimbolanden, DE
Erfassung von Taktzeiten und dessen Variabilität alle Einzelteile (mit u.a. SAP) von 20 verschiedene Turboauflader für Daimler AG , über die ganze Produktionskette von Unterlieferanten, Lieferanten, die eigene Produktion bis hin zur Kundenbedarf. Identifikation von Schwachstellen, Entw. ein Simulationswerkzeug für Teilbestände unter Beobachtung der Kundennachfrage und Engpässe über 24 Mon. Vorschlag von Lösungsansätze. (Kontakt: Martin Rößing)				

SPRACHEN	Englisch	Spanisch	Französisch	Deutsch	Ungarisch
	← <i>Muttersprachniveau</i> →			Verhandlungsfähig Grundkenntnisse	
INTERNAT. ERFAHRUNG	8 Jahre in Kanada	10 Jahre in Spanien	7 Jahre in Frankreich	8 Jahre in Deutschland	

WISSENSCHAFTLICHE BEITRÄGE

Beiträge	10 Papers; Konferenzen: 2 Vorträge, 2 Poster	Uni. Saarland	2012-16
Forschungsprojekte	„Laser and Carbon: CNT synth. and annealing“ (PhD)	Uni. Saarland	Saarbrücken, 2015
	Ultraschalltorsionsschweißen von AlMg3/CFRP	TU KL	Kaiserslautern, 2008
Auszeichn.	1. Platz Bundesweit Rasterelektronmicroskopie	cc-nanobionet	WING, Berlin, 2011

STIPENDIEN (Arbeit, Mobilität & Studium)

Haute Normandie 2005 (FR)	Deutschfranz. Hochsch. 2006 (DE)	DAAD Matching Funds 2010 - 12
NanoCom 2011 & 12 (ARG)	SUMA2 2014 (CHI)	CREATE 2015 & 16 (URU)

IT-KENNTNISSE

Prog.-Sprach.	C++, ISO, G-code (CNC), Matlab, XHTML, CSS, PHP, JavaScript.
Engineering	Catia, AutoCAD, Ideas, Matlab, SAP R3, DevC++, Corel, Vector & Bitmap Programme

INTERESSE Professioneller Schlagzeuger & Perkussionist | Klettern, Mountainbike, Laufen | Graf. Design
Webprogrammierung und -design | Freiwilliger Web-Developer bei NRO Sématos | Reisen | Möbel basteln

Online researcher profiles



Google

Scholar

<https://scholar.google.com/citations?user=QoTQv2AAAAAJ&hl>



Research

Gate

https://www.researchgate.net/profile/Nicolas_Souza



Learn to say 'no'

– Prof. Frank Mücklich

Award for excessive dedication to
scientific English proofing